Faraday instability in binary fluids

Vibhor Jajoo

université de BORDEAUX

THÈSE PRÉSENTÉE

POUR OBTENIR LE GRADE DE

DOCTEUR DE

L'UNIVERSITÉ DE BORDEAUX

ÉCOLE DOCTORALE DES SCIENCES PHYSIQUES ET DE L'INGÉNIEUR

SPÉCIALITÉ MECANIQUE

Par Vibhor JAJOO

INSTABILITÉS DE FARADAY DANS LES FLUIDES BINAIRES

Sous la direction de : Sakir AMIROUDINE
(Co-directeur : Farzam ZOUESHTIAGH)

Soutenue le **18 Décembre 2017**

Membres du jury :

M. DELVILLE, J.P.	Université de Bordeaux	Président
M. CARLES, P.	Université Pierre et Marie Curie, Paris	Rapporteur
M. MOJTABI, K.	Université Paul Sabatier, Toulouse	Rapporteur
M. MARRE, S.	Université de Bordeaux	Examinateur
M. DELAROCHE, C.	Centre National d'Etudes Spatiales	invité
M. NARAYANAN, R.	Université de Floride, USA	invité
M. AMIROUDINE, S.	Université de Bordeaux	Directeur de thèse
M. ZOUESHTIAGH, F.	Université de Lille 1	Co-Directeur de thèse

THESIS

SUBMITTED TO

UNIVERSITY OF BORDEAUX

ÉCOLE DOCTORALE DES SCIENCES PHYSIQUES ET DE L'INGÉNIEUR

SPECIALITY: MECHANICAL ENGINEERING

by Vibhor Jajoo

TO OBTAIN THE DEGREE OF

DOCTOR OF PHILOSOPHY

FARADAY INSTABILITY IN BINARY FLUIDS

Under the direction of: Sakir AMIROUDINE
(Co-director: Farzam ZOUESHTIAGH)

Defended on

December 18, 2017

Graduation Committee:

M. DELVILLE, J.P.	Université de Bordeaux	Président
M. CARLES, P.	Université Pierre et Marie Curie, Paris	Rapporteur
M. MOJTABI, K.	Université Paul Sabatier, Toulouse	Rapporteur
M. MARRE, S.	Université de Bordeaux	Examinateur
M. DELAROCHE, C.	Centre National d'Etudes Spatiales	invité
M. NARAYANAN, R.	University of Florida, USA	invité
M. AMIROUDINE, S.	Université de Bordeaux	Directeur de thèse
M. ZOUESHTIAGH, F.	Université de Lille 1	Co-Directeur de thèse

Titre : instabilités de Faraday dans les fluides binaires

Résumé court

Alors qu'il est bien connu que le phénomène d'instabilité de Faraday est une manifestation d'ondes de gravité capillaire, son comportement lorsque les effets capillaires et gravitationnels disparaissent reste inexploré théoriquement et expérimentalement. Une étude expérimentale et théorique détaillée est réalisée pour comprendre la physique de ce phénomène dans une petite cavité rectangulaire où la proximité des murs entraîne des contraintes considérables sur les parois latérales. Un couple de liquides binaires est utilisé avec une faible tension interfaciale pour une interface presque plate. Le contrôle thermique de ce système de fluide est utilisé pour diminuer la force capillaire et d'étudier ainsi les instabilités de Faraday dans les fluides miscibles où la tension interfaciale s'annule. Afin de prendre en compte les effets gravitationnels, l'expérience a été réalisée dans des campagnes de vols paraboliques. Pour l'approche théorique, une analyse de stabilité linéaire est effectuée à l'aide d'équations de Navier-Stokes dans un système de fluide visqueux incompressible et newtonien. Ceci est réalisé grâce à une méthode de Fourier-Floquet résultant en un problème aux valeurs propres. Les comparaisons montrent des différences non négligeables. Les équations sont ensuite résolues en incluant des effets d'amortissement visqueux pour compenser les contraintes des parois latérales. Les fluides binaires ont fourni une option commode pourchanger le coefficient de tension interfaciale en augmentant la température jusqu'à la température critique, ce qui a permis de passer d'un système de fluides non miscibles à celui des fluides miscibles tout en restant au-dessous de la température d'ébullition. Le taux d'amortissement visqueux linéaire est mesuré expérimentalement. La correction des calculs théoriques en prenant en compte le taux d'amortissement visqueux a permis une amélioration nette des résultats et donc de mieux comprendre la prédiction de l'amplitude critique expérimentale pour les modes sous-harmonique et harmonique.

Mots clés: INSTABILITÉS, FARADAY, FLUIDES BINAIRES, VOLS PARABOLIQUES, ANALYSE DE STABILITE LINEAIRE

Institut de Mécanique et d'Ingénierie

ENSCBP bât A, *16 avenue Pey-Berland, 33607 PESSAC Cedex*

Title: Faraday instability in binary fluids

Short version of abstract:

While it is well known that the phenomenon of Faraday instability is a manifestation of vibrational acceleration, its behaviour when both the capillary and gravitational effects vanish, remains unexplored theoretically and experimentally. A detailed experimental and theoretical study is performed to understand the physics of this phenomenon in small rectangular geometry where the proximity of wall results in considerable sidewall stresses. A novel binary liquids system is utilized with low interfacial tension for a near flat interface. Thermal control of fluid system is utilized for achieving reduction in capillary force with study of miscible fluids where interfacial tension reduces to almost zero. In order to discriminate between gravity and capillarity effects, experiments were performed in parabolic flight campaigns. . For the theoretical approach a linear stability analysis is performed through Navier-Stokes equations in a Newtonian incompressible viscous fluid system. This is achieved through a Fourier Floquet method resulting into an eigenvalue problem. Equations are solved by including viscous damping effects for compensating sidewall stresses. Experimentally binary fluids provided a convenient option of changing the coefficient of interfacial tension by temperature control and going through immiscible to miscible system without change of liquid charge. Viscous damping rate is determined experimentally by measuring the linear damping rate. The correction in the theoretical calculations with the viscous damping rate helped in achieving a better understanding of the prediction of the experimental critical amplitude for sub-harmonic and harmonic modes.

Keywords: FARADAY, INSTABILITY, BINARY FLUIDS, PARABOLIC FLIGHT, LINEAR STABILITY ANALYSIS

Institut de Mécanique et d'Ingénierie

ENSCBP bât A, *16 avenue Pey-Berland, 33607 PESSAC Cedex*

Dedicated to the feeling of being loved

Acknowledgement

When I started this work in January 2015, I did not know that the next three years of my life will be full of extemporaneous events. There have been many people who stood beside me, guided me, showered their love and blessings on me, befriended me and provided me opportunities for which I was not worthy enough. Expressing gratitude to them is joyful for me.

My research would have been impossible without the aid and support of Prof. Sakir Amiroudine & Prof. Farzam Zoueshtiagh whose guidance and fatherly concern helped me to complete this doctoral thesis. I am profoundly grateful to Prof. Ranga Narayanan, a humble man and role model I wish to become. Heartfelt thanks go to Diwakar S. V., who took care of me as his own younger brother.

I am also very indebted to Madame Valerie Thouard, the busiest person at I2M and Nicolas Meadeb from International office of University of Bordeaux, They were especially helpful in my dealings with administration (and showed tolerance to my minimal knowledge of French!).

I would like to say that I am an extension of my father and mother. I owe my life to them. They have given me life; given me shelter, care, unconditional love and support.

I also want to thank the CNES & Région Aquitaine for funding this project. I am grateful to them in no small measure.

At last I want to say that the letter we intended to write, the word of appreciation we intended to express, the prayers we intended to offer when we had more time to express to the Lord our appreciation for his goodness. We are grateful for all of these things that are done for us, of course, but in our busy life we don't always express appreciation for what others do for us. As we express our gratitude, we must never forget that the highest appreciation is not to utter words, but to live by them.

Abstract

When one or more fluids are vibrated normal to the surface of a fluid or at the interface of fluids, standing waves appears on interface. This phenomenon is known as Faraday instability. In physical terms, when imposed frequency resonates with the natural frequency of the system, wave patterns appear on the surface of the fluid. In this thesis, experiments displaying the Faraday instability are presented and described mathematically with the help of linear stability analysis. These experiments (on ground and in microgravity conditions through parabolic flights) are well thought-out by input parameters such as the vibrational amplitude and frequency which, at criticality, give rise to a wide range of patterns. These patterns form a recognizable and predictable wave structure. This thesis considers immiscible and miscible cases where the manifestation of Faraday waves requires a jump in the density across the interface and density gradient respectively. The acceleration due to parametric excitation must act perpendicular to the interface and in the case of miscible fluids, it must be parallel to the density gradient.

Experiments illustrate the effects of gravity and interfacial tension forces on the Faraday instability appearing in immiscible system within a confined boundary system. A fluid pair is picked judiciously (the Perfluorohexane Liquid FC72 and 1 Cst Silicon oil) to have a binary fluid system of experimentally achievable consolute temperature (i.e below the boiling temperature). Also, it should be nontoxic in order to avoid any accidents happening in case of leakage in parabolic flight campaign or in future experiments planned in the International space station. As the surface tension between the two liquids is very low, it leads to minimum meniscus and an almost not pinned triple contact line at wall.

The influence of gravity was comprehended by carrying out experimentations on earth as well as in microgravity environment, created in a parabolic flight. The influences of density difference and interfacial tension are understood by the variation of fluid temperature utilizing a thermal bath. Experiments are performed to determine the critical threshold amplitude and to measure different forced parametric frequencies. In the chosen small rectangular geometry, critical threshold curves show discrete modes on earth. A clear drift of these modes towards

lower frequency is seen as the temperature of the liquid pair approaches its consolute value, i.e., the temperature at which the binary pair is completely miscible.

For the theoretical approach, a linear stability analysis is performed through Navier-Stokes equations in a Newtonian incompressible viscous fluid system. This is achieved through a Fourier Floquet method resulting into an eigenvalue problem. The linear stability analysis approach is very popular and has been used for successful prediction of critical threshold for low frequency in large sized deep cylindrical container. Experiments in small rectangular geometries with low viscous fluid still remain unsolved with respect to theory. For the successful prediction, equations are solved by including viscous damping effects which are determined experimentally by measuring the linear damping rate.

Résumé

Les ondes superficielles ou interfaciales générées par la vibration d'un ou plusieurs fluides dans la direction perpendiculaire à l'interface, sont connues sous le nom d'instabilité de Faraday. En terme physique, lorsque la fréquence imposée résonne avec la fréquence naturelle du système, des motifs apparaissent à la surface du fluide. Dans cette thèse, les expériences montrant l'instabilité de Faraday sont présentées en comparant aux résultats de l'analyse théorique basée sur la stabilité linéaire. Les expériences sont menées avec des paramètres d'entrées comme l'amplitude et la fréquence de vibration qui donnent lieu à une large gamme de paramètres permettant d'obtenir les valeurs critiques pour détecter les instabilités de Faraday. Cette thèse traite les cas miscibles et non-miscibles où la manifestation des ondes de Faraday nécessite un saut de densité à travers l'interface et un gradient de densité respectivement. L'accélération due à l'excitation paramétrique doit être perpendiculaire à l'interface dans le cas des fluides immiscibles et, dans le cas des fluides miscibles, elle doit être parallèle au gradient de densité.

Les expériences illustrent l'influence de la gravité et de la tension interfaciale sur l'instabilité de Faraday qui surviennent dans un système confiné de fluides non miscibles. Afin de passer facilement de ce système de fluides immiscibles au système de fluides miscibles, nous avons sélectionné judicieusement un couple de fluides binaires (le Fluorinert FC72 et 1 cst d'huile de silicone). Lorsqu'on augmente la température, la tension de surface diminue jusqu'à devenir nulle rendant ce système de fluides, miscible. De plus, il doit être non-toxique pour éviter les accidents en cas de fuite dans les campagnes de vol parabolique ou dans des expériences futures dans la station spatiale internationale et au-dessous de la température d'ébullition. La tension superficielle entre les deux liquides étant très faible, elle entraîne aussi un faible ménisque et une ligne de contact triple mobile et en phase avec la vibration.

L'influence de la gravité a été analysée en effectuant des expérimentations aussi bien sur terre qu'en microgravité lors des vols paraboliques. L'influence de la différence de densité et de la tension interfaciale a été prise en compte par la variation de la température du fluide en utilisant un bain thermique. Ces expériences ont été effectuées pour déterminer le seuil

critique et pour mesurer les différentes fréquences paramétriques du système de fluides considéré. Dans la géométrie rectangulaire choisie (de dimensions relativement petites), des courbes critiques de seuil ont montré l'existence de modes discrets sur terre. Une déviation de ces seuils vers une fréquence inférieure a été observée lorsque la température de ces fluides binaires s'approchait de sa valeur critique de miscibilité.

Une analyse de stabilité linéaire est effectuée parallèlement à ces expérimentations en considérant les équations de Navier-Stokes dans un système de fluides visqueux incompressibles et newtoniens. La méthode de Fourier-Floquet est adoptée résultant en un problème aux valeurs propres. L'approche de l'analyse de la stabilité linéaire a été déjà considérée dans la littérature dans le cas d'une cellule cylindrique de grande taille et a permis de prédire le seuil critique dans le cas des basses fréquences. En revanche, les expériences dans les géométries rectangulaires de petite taille dans le cas d'un fluide peu visqueux sont restées non résolues par rapport à la prédiction théorique. Nous avons résolu ce problème en incluant des effets d'amortissement visqueux dans notre modèle théorique et qui sont déterminés expérimentalement en mesurant le taux d'amortissement linéaire.

Nomenclature

Roman Symbols

A	Applied amplitude	m
F	Function defining implicit form of evolution of interface	-----
f*	Crossover frequency	Hz
g	Gravitational acceleration (9.81 m/s^2)	m/s^2
h_1	Height of top fluid layer	m
h_2	Height of bottom fluid layer	m
$\mathbf{I}$	Identity tensor	-----
$2H$	Twice the mean surface curvature	m^{-1}
k	Wavenumber	m^{-1}
$\mathbf{k}$	Unit vector in direction of gravity	-----
l_v	Stokes layer thickness	m
L	Length of experimental cell	m
M	Momentum	kg/m^2s
m	Fourier mode in depth direction	-----
$\mathbf{n}$	Normal unit vector to the interface	-----
n	Fourier mode in lateral direction	-----
P	Pressure field	Pa
p	Square of the natural wave frequency of a Faraday system	s^{-2}
q	Parametric amplitude	m/s^2
p_0	Base state pressure	Pa
p	Change in pressure due to perturbation	Pa
r	Distance of a point from origin in fixed frame system	m
r'	Distance of a point from origin in moving frame system	m
R	Distance between origins of fixed to moving frames	m
t	Time	s
$\mathbf{T}$	Stress tensor	N/m^2
$\mathbf{U}$	Velocity vector of interface	m/s

$\mathbf{V}$	Velocity vector of fluids	m/s
$\mathbf{v}$	Change in velocity vector due to perturbation	m/s
w	z- Component of velocity	m/s
W	Width of experimental cell	m
Z	Interface position	m

Greek Symbols

ρ_1	Density of top fluid layer	kg/m^3
ρ_2	Density of bottom fluid layer	kg/m^3
ω	Applied frequency	Hz
γ	Interfacial tension	N/m
μ	Dynamic Viscosity of fluid	$(N.s)/m^2$
ν	Kinematic Viscosity of fluid	m^2/s
ε	Infinitesimal perturbation for all variables	-----
ζ	Change in interface location due to perturbation	m
ς	Wave response amplitude	m
α	Wave response frequency	Hz
σ	Complex growth rate	-----

Indices

j	Common fluid indices (1,2)
1	Top fluid
2	Bottom fluid
0	Initial / base state
x	X – component
xz	XZ surface

Mathematical symbols

∇^2_{H}	Horizontal divergence

Abbreviations

cSt	Centistokes
FC-72	Perfluorohexane
ISS	International Space Station
NTC	Negative temperature coefficient
PID	Proportional integral derivative
PR-59	Proportional Controllers-59
PTFE	Poly tetra fluoroethylene
PT-100	Platinum Resistance
RS-232	Recommended Standard 232
RTD	Resistance Temperature Detector
SSR	Solid state relay
TEM	Thermoelectric module

Table of Contents

Chapter 1

General introduction and literature review to Faraday instability

It is well known that the Faraday instability is a manifestation of gravity-capillary wave phenomena wherein nonlinear discernible wave patterns emerge (see Figure 1.1) on a fluid interface that is subjected to perpendicular oscillations and exceeding a critical value. Faraday instability is generated due to the result of the parametric resonance of interfacial wave modes with an imposed vibrational frequency. It is a phenomenon of motorized perturbation and oscillation at definite frequencies. This is unlike the regular resonance as it reveals the phenomenon of hydrodynamic instability. Faraday waves can be usually witnessed as crispation appearing on the surface in a wineglass that is buzzing like a bell or can be observed with sand particles on a vibrating plate using a violin bow as witnessed by Faraday (Faraday, M., 1831). Faraday's violin bow instigated the plate to vibrate in a systematic motion at a certain frequency shaping tiny ripples of sand particles. These waves appear first at the centre of vibration and spread out towards nodal lines. Faraday later did detailed experiment with liquids such as water or mercury and noted that the fluid layer vibrating frequency is half of the applied frequency. He also observed that appearing patterns on the surface is same regardless of its container shape. This observation was an insight to the nonlinear behaviour of the phenomenon (see Figure 1.1(b)).

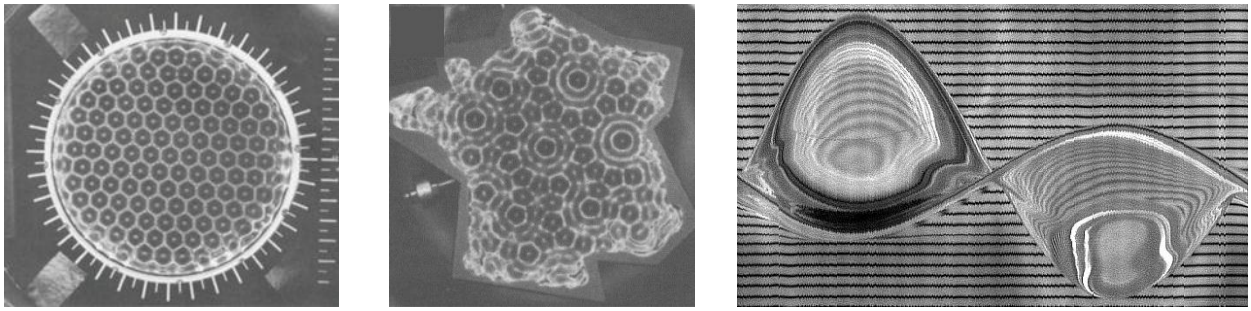

(a) (b) (c)

Figure 1.1: Faraday instability as observed by a) Edward and Fauve (1994) b) François Gallaire et al. (2017) c) W. Batson (2013)

Faraday also indicated that the note on the bow should be sufficiently loud for observation of undulations on the surface. Faraday experiments in general create peripatetic meniscus waves,

starting from container wall, and standing Faraday waves inside the cell. When the forced vibration is frail, only meniscus waves ruffle the surface. However, when strong vibrations are induced to increase the energy in the system (which in turn exceeds the dissipation due to the bulk viscosity) fluid surface is destabilized to fashion Faraday waves which grow to finite amplitude. This condition signifies a threshold energy requirement which must be exceeded in order for the phenomenon to be perceived, and is straight linked to the existence of dissipation mechanisms in the system. Measurement of these thresholds and linking it to a mathematical prediction is the emphasis of this thesis.

1.1 Basic phenomenon of Faraday instability

In laboratory setting, Faraday instability is studied by using a driven harmonic oscillator, in which the oscillations are driven by varying some parameters of the system at some frequency under controlled conditions. Here, the resonant behaviour is governed by various factors such as system geometry, gravity, and interfacial tension. A comprehensive understanding of the Faraday instability thus entails a clear demarcation of the role played by each of these effects. Interestingly, both gravity and interfacial tension play their roles which are primarily determined by the imposed frequency of excitation. In current study these two parameters have been studied in depth where the capillary force of the liquid was controlled by means of thermal bath while the effects of gravity force has been studied through parabolic flights experiments.

Faraday instability parameter such as gravity plays a dual role of aiding the instability at low frequencies of excitation and suppressing it at higher values. Though a similar effect is also manifested by interfacial tension, understanding its sole influence becomes very difficult under terrestrial gravity conditions. Due to large density gap and low interfacial tension of chosen fluids, gravity dominates here over the capillarity force for the investigated frequency range. We have performed experiments on ground and under reduced gravity conditions for understanding the gravity and capillary effects separately.

Past experiments have had good agreement when compared to its theory in cylindrical container (Batson, W. 2013); however similar theories with same fluids did not deliver a valid match in a small size container. Current experiments were focused to small rectangular geometries in which excited wavelength were of the order of the dimensions of the container. In earlier investigations, experimental thresholds did not come to an agreement with the estimates of the viscous linear stability model, thus inspiring this work.

In the present study, Faraday experimentation consisted of an oscillating Hele-Shaw (for the current experimental investigation, the frequency range is chosen such that, there is no velocity motion observed in the smaller dimension of cell, (See Figure 3.5) type cell containing binary fluids and inducing oscillations of the fluids and the interface between them. Exceeding a certain threshold, the interface formed standing wave patterns with different modes. The use of binary fluids here offered a useful possibility of altering the factor of interfacial tension by temperature control (it approached to zero as the temperature raised to the upper consolute value). These fluids could freely slip along the vessel wall, signifying the reduction of stress related to the sidewalls (see section 3.2) and with near horizontal interface to realize the closest possible assumptions of the linear viscous theory. However even after picking a careful set of liquids, it has been validated that the hypothesis of stress-free sidewalls is not absolutely correct and created disparity from theory specifically in small cell sized system.

Earlier, energy dissipation during wave motion was considered with the fluid viscosity being its primary force, which is not absolutely true. Thus concept of sidewall stresses and boundary layer effects evolved. While an effective methodology (Henderson & Miles, (1990)) existed for the quantification of the sidewall stresses, past experiments did not consider thin Hele-Shaw cells. This work discussed the calculation of dissipation (caused by sidewall stresses) which is often challenging, necessitating its measurement straight from the experiment. It has been shown that an experimental attempt can be made to study the appropriate boundary conditions, allowing prediction of threshold. This work architected a procedure to accurately predict selected modes and threshold amplitudes, and pinpointed the causes for difference which advanced the study of this rich phenomenon.

The cause originated from the fact that the two fluids contacting the compact sidewalls unavoidably yielded a static meniscus, which emitted waves during vibration exhibiting non-ideal behaviour, and violating the assumption of a flat interface. More specifically the role of wall proximity caused damping of small forcing frequency. It has been shown that a damping coefficient derived from linear theory for unbounded containers with specific wave numbers might be used to describe any discrepancies between a linear model in bounded containers and experiment. It has been further found that the damping coefficient depended only upon mode structure, the mode pattern being constant over a frequency range. The correction in the theoretical calculations with the viscous damping rate helped in achieving a better understanding for the prediction of the experimental critical amplitude for sub-harmonic and harmonic modes.

Analytically the problem in hand has been solved as single mode excitation and linear stability model. Faraday instability is a non-linear phenomenon, requiring some assumptions in obtaining an analytical solution without the need of using a numerical procedure and computers. Nonlinear systems could be treated as linear system to simplify the mathematics. A simple pendulum can be a perfect example of that. If the amplitude of the pendulum is small, the pendulum obeys the rules as a linear dynamical system. However, if the amplitude is large this is no longer true. In other words, a nonlinear system can be treated as a linear system when it is close to stable state. The system equations have been derived through Navier-Stokes equations in a Newtonian incompressible viscous fluid system. A Fourier-Floquet method resulting into an eigenvalue problem has been applied to the dispersion equation. The resulting equations have been solved by a matrix system as used by Kumar and Tuckerman (1994). Theory has been adjusted with the damping condition and lateral dimensions were taken in account for mode discretization. Thus experiments and theory of Faraday instability were reconciled over a range of temperature in which a chosen fluid system went continuously from immiscible to miscible fluid system.

Both experimental and theoretical analysis of miscible or partially miscible fluid systems was fraught with challenges. Theoretical stability analysis of such systems became complex due to

the ever-changing base state and undefined initial conditions. Difficult challenges in experiments were faced in terms of precise repeatability for which exactly same initial state for fluids needs to be posed before each experiment.

To move from immiscible to miscible state, the chosen binary fluid has properties depending on temperature (consolute). It has a notable feature of being miscible above the consolute temperature and immiscible or partially miscible below it. Furthermore, by controlling the temperature of the fluid, it was possible to control the mass diffusion coefficient, which was an important asset that regulated fluid mixing process. Constant state of mass-diffusion forces experiments have to be done precisely with specific time-interval to achieve repeatable results.

Experiments in parabolic flights were another challenge as it has time constraints and constant jitter vibration passed down to experiment. Experimental setup had to be designed to withstand hyper gravity which is a bi-product of zero-g flight path. Experimental cell had to be carefully sealed to remove any gas present in fluids and thermal bath, as bubbles could have disrupted in experiment and visuals respectively.

This thesis explains the experimental and analytical study of Faraday instability with challenges and countermeasure used for successfully prediction of its behaviour. In this dissertation some very thought-provoking phenomenon has been shown that were not investigated in the previous experiments. Modified analytical theory was successful in predicting the threshold as observed in experiments.

Faraday waves have some potential applications and contribute for the development of science. One of the direct applications of the present study is to understand mixing to extrication of droplets and air formation in capillary tubes during space enabling operations. In industrial settings Faraday waves are widely utilized for fluid prototypes for producing micro-scale materials such as cell spheroids and cell-seeded micro-carriers. By the knowledge of Faraday waves, attenuated layers of material can be deposited in a preferred configuration and particles in the fluid can be drawn producing precise optical instruments. In Mother Nature, Faraday waves have the role in the intensification of seismic activity through slacker sediments.

In the field of quantum mechanics, Faraday waves have been professed in Bose-Einstein Condensates.

1.2 Literature Review

The Faraday instability occurs when two fluid layers of different densities are parametrically excited and the imposed frequency resonates with the system's natural frequency. The natural frequency depends on the density difference, interfacial tension, viscosities, and geometry. Interfacial instability generated due to the parametric excitation is commonly called as "Faraday instability". A detailed experimental and theoretical study and of its potential applications are required to understand the physics behind the phenomenon. The immiscible fluid system has been well studied in the literature but still lacks a thorough understanding, as experimental work in literature has dissimilarities with present theoretical approach. On the other hand, the case of miscible liquids, which is important to understand the processes of mixing is much less considered in previous works. For liquid sets with low interfacial tension, gravitational force on the oscillatory convection becomes dominant and in order to understand the phenomenon of capillary force, gravity free environment becomes thus necessary.

Sand figures on vibrating plates were first analyzed and described by Ernst Florens Friedrich Chladni (Leipzig, 1787). These figures are known as Cladni Figures. The phenomenon of appearance of remarkable array generated on a liquid surface near a vibrating surface was first observed by (Oersted, 1813) and subsequently reported by (Wheatstone, 1825) and (Weber, 1825). Faraday (1831) was first to report the phenomenon in detail and deduced that the frequency of excited waves is half of the applied frequency. Melde (1860) reported similar observation by generating parametric oscillations in a string by using a tuning fork to periodically vary the tension at twice the resonance frequency of the string. Mathematically, parametric oscillation was first treated as a general phenomenon by Rayleigh (1883, 1887). He presented the argument for the existence of subharmonic solution. Faraday (1831) defined that generated patterns were independent of the container geometry and proved non-ideal behaviour of this phenomenon. Raman (1912) expanded Rayleigh's theory by including cubic nonlinearity into equations. Nonlinear behaviour in the Faraday wave is dependent on

restorative wave forces such as buoyancy (in case of stable configuration, heavier fluid on the bottom layer) and surface tension and dissipative forces such as viscosity. The first clear and complete theoretical description of the phenomenon was given by Benjamin and Ursell (1954) who considered the instability in the inviscid limit. They condensed the inviscid fluid equations of motion in the classical form of Mathieu equation which is similar to parametric excitation of a linear harmonic oscillator.

Subsequent to inviscid hydrodynamic stability analysis by Benjamin and Ursell (1954), Kumar & Tuckerman (1994) presented the stability of an infinite bilayer subjected to parametric vibration, including viscous effects in the Navier-Stokes equations. They performed a linear stability analysis for two infinite layers of immiscible fluids with a Fourier-Floquet analysis for the disturbed interfacial deflection. Marginal stability curves for critical amplitude (threshold value) as a function of wavenumber were obtained by setting the eigenvalue (growth rate of the Floquet exponent) to the value of zero. This analytical solution is the base of the theory used in this work which will be detailed later in the chapter 2.

It was clear from the previous research work that for problems of inviscid cell with unbounded extent, the natural frequency is very weakly dependent on interfacial tension, this property plays a role only when the side wall spacing is of the order of the capillary length. This idea continues to be true in the theory even when viscosity is taken into account as in Kumar and Tuckerman (1994). Now, in experiments the fluid viscosities cannot be ignored and the proximity of walls becomes important because of the viscous damping induced by wall stresses. At high forcing frequencies, the response wavenumbers are large (short wavelengths) and they are not affected by the presence of side walls. However, at low frequencies, the wavelengths are large and the patterns, i.e., modes that are seen at the onset of instability reflect the presence and geometry of the side walls.

One of the early experiments which focused on boundary conditions was that of Douady and Fauve (1988) who studied the effect of contact angle on the meniscus waves that inevitably form along the walls. For the purpose of removing these meniscus effects, they have tried to pin the boundaries. However such experiments are difficult to control, often leading to sloshing

after the instability commences. An alternate solution is to provide a close approximation to a stress free boundary condition such that the interface will always be making a perpendicular angle to the sidewall while sliding up and down to the boundary. However, most fluids induce a contact angle with the wall and thus generate a contact angle hysteresis as discussed by Hocking (1987). One way to provide a condition that is close to stress-free is to employ a fluid system wherein the upper fluid easily covers the common interface forming a very thin layer in contact with the container wall near the interface. As the walls are shaken with parametric forcing frequency the thin layer also moves in the form of "meniscus waves" and as long as the walls are spaced apart at distances several times the capillary length, there is no effect of damping. Thus, a very good agreement between theory and experiment can be obtained and this was demonstrated convincingly by Batson *et al.* (2013).

Our interest in the present work is to investigate the effect of side wall damping that arises from meniscus waves. If this could be accounted for, then a better comparison between theory and experiment can be obtained. Previous studies have shown that in large cylindrical cells, meniscus waves effects vanish as instability overpowers it. However, for cell size comparable to wave size meniscus, it plays an important role as shown by Henderson and Miles (1989, 1990). The damping length has been defined by Edwards and Fauve (1994) as $l_{decay} = (\frac{1}{2}\ \omega k)/2\nu k^2$ (ω is the frequency, k is the wavenumber and ν is the kinematic viscosity). They studied the effects of sidewall conditions and deduced that the damping length of a standing wave must be less than that of the container size in order to ignore sidewall effects. Hill (2002) investigated the effects of the energy dissipation through the varying domain wall sizes. Hill's experiments did not show any effects of top and bottom walls damping (the fluid height used was deep enough to take out any effect from these walls). They also observed that side wall damping dies off fairly rapidly as the domain becomes larger. In conclusion, the wavelength of the order of the domain size suffers suppression from wall damping.

Ito *et al.* (1999) and Tipton & Mullin (2004) performed experiments with two fluids layers with sidewall flow perturbations on the instability. Data presented by them were not in agreement with the Kumar and Tuckerman (1994) Faraday viscous theory model. Tipton & Mullin (2004)

mentioned that their damping rate was eight times the value calculated by the linear stability viscous model. It was assumed that wall damping was playing an important role as cell diameter for the experiments as cell size was small (35mm in their case). Das & Hopfinger (2008) later compared dissipation (in terms of length) in the interior of the domain (δ_i) to the dissipation (δ_w) in the Stokes layer near the boundary. The ratio of these two dissipation rates was defined by Lighthill (1978) as $\delta_i/\delta_w = 2l_v/L$ (where $l_v = (2\nu/\omega)^{1/2}$ is the Stokes layer thickness and L is the domain length). The internal to wall damping ratio for smaller-size cells with low viscous fluids system is small, indicating that boundary layer dissipation dominates over internal dissipation.

Edwards and Fauve (1994) had shown previously that experiments conducted with low-viscosity fluids bring significant finite-size effects even when the cell size to wavelength ratio is not small (cell size/wavelength = 5). Henderson and Miles (1990) had compared experimental and theoretical results in rectangular and cylindrical geometries. However, Henderson and Miles (1989) observed that in a rectangular cylinder, the measured linear viscous damping rates are found to be higher than the predicted values, increasing drastically the value of effective viscosity. They also noted that rectangular geometries led to higher wave damping which could have come from corner stresses and Stokes boundary layer.

Another aspect of this thesis is to study the mixing generated by Faraday instability in miscible fluids. In miscible fluids system, the interface is diffused (in contrast to a singular interface in immiscible system) thus creating a gradient of density in the system driving the instability. The instability grows itself with forced vibration and ultimately destroys itself with the mixing of the liquids. The mixed volume is considerably large in comparison to the initial diffused region. Zoueshtiagh *et al.* (2009), Amiroudine *et al.* (2012) and Diwakar S.V., *et al.* (2015) presented results of experimental and numerical model with good qualitative and quantitative agreements. They described the importance of the waiting period before the vibration is set. As the waiting time is increased, diffusion in the system weakens the driving potential and results in smaller wavelengths. One of the key observations in these studies of miscible fluids systems is that they obtained similar dispersion relations as in Kumar and Tuckerman (1994) for

immiscible fluids systems. It was considered that the reasons of growth of instability are similar to that of immiscible case while causes of stabilization differ.

The objective in the present work is to understand the reasons for the mismatch between the theory used by Batson *et al*. (2013) and the experimental results. This requires measuring the viscous damping rate in a rectangular container (as considered in our experimental set-up) and using the theoretical damping rate to determine the effective viscosity due to the presence of the meniscus waves. It is then used to modify the Kumar and Tuckerman (1994) viscous theory which can be compared with the experimental data.

Chapter 2

Theory of parametric instability

Faraday instability has been studied extensively in the past, out of which inviscid theory of Benjamin and Ursell (1954) and viscous theory of Kumar and Tuckerman (1994) marked a milestone in the development of theoretical understanding. This chapter refers to theoretical and numerical approaches of wave phenomenon as described by Faraday (1831), generated at the vibrating liquid surface in the direction of normal to the interface of fluids. . Faraday waves are characterized by deflection, growth and saturation of waves appearing at a flat fluid surface while vibration surpasses the critical amplitude for a particular frequency. Faraday mainly observed the wave frequency to be one half of the imposed vibrational frequency, a sub-harmonic response, which corresponds to a subset of parametric excitation. Following in this chapter a general idea of the mechanism of inviscid Faraday problem is explained. Further viscous analysis and linear stability analysis is explained in detail.

2.1 Inviscid fluid bilayer subjected to perpendicular vibration

Benjamin and Ursell (1954) described this phenomenon successfully by assuming non viscous fluids and thus reducing mathematical calculation by great deal and reducing inviscid fluid motion in standard form (McLachlan, 1947) of Mathieu equation derived from non-viscous Navier-Stokes equation

$$\frac{d^2\varsigma}{dt^2} + \big(p - 2q\ cos(2t)\big)\varsigma = 0 \tag{2.1}$$

Where ς is the wave response amplitude, t is time, p is the square of the natural wave frequency of a Faraday system, determined by the fluid densities (ρ_1, ρ_2), surface tension (γ), and wavenumber (k), and q is the parametric amplitude. They are defined as,

$$p = \frac{(\rho_1 - \rho_2)gk - \gamma k^3}{(\rho_1 \coth kh_1 + \rho_2 \coth kh_2)}$$

$$q = \frac{(\rho_1 - \rho_2)A\omega^2}{2(\rho_1 \coth kh_1 + \rho_2 \coth kh_2)}$$

h_1, h_2 are the heights of the two fluid layers (see Figure 2.1)

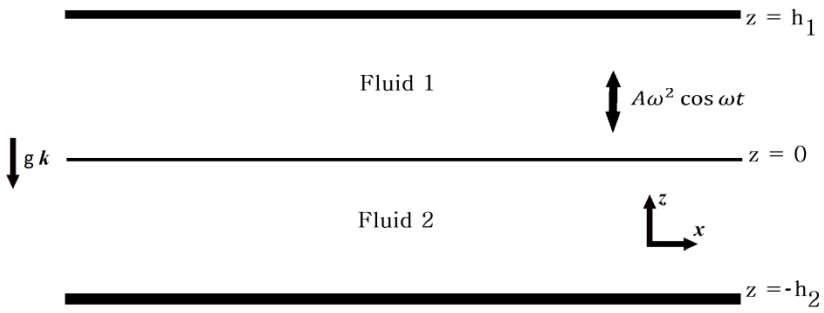

Figure 2.1: An infinite bilayer system

With the help of Floquet's theory, the Mathieu equation (periodic linear differential equations of the form $\ddot{\varsigma} = B(t)\varsigma$ with a defined period and gives the state of the stability of solutions) can be solved for two independent solutions of the form $e^{y_1 t}\,\tilde{\chi}(t)$ and $e^{y_2 t}\,\tilde{\chi}(t)$ where $\tilde{\chi}(t)$ is periodic and $y_1$and y_2 are functions of the system parameters *'p'* and *'q'* called as characteristic exponents. *'p', 'q'* which consist of regions in which the real parts of $y_1$and y_2 are negative, indicating bounded (stable) solutions, and positive value indicating an unbounded (unstable) solution. On the boundaries between stable and unstable regions, the real parts are zero. If $y_2 = y_1 = 1$, the solution is periodic with period T = π and if $y_2 = y_1 = -1$ the solution is periodic with period 2T = π (see Appendix **B** for solution of parametric equations with MATLAB code).

With the help of numerical integration of equation 2.1 it can be observed that for certain values of "*p*" and "*q*" the response *"ς"* grows without bound with half-integer frequencies with respect to the parametric frequency as shown in Fig 2.2(a). For other values, the response "ς" can be periodically stable as shown in Fig 2.2(b) also called as critically stable and completely stable in response to vibration as shown in Fig 2.2(c).

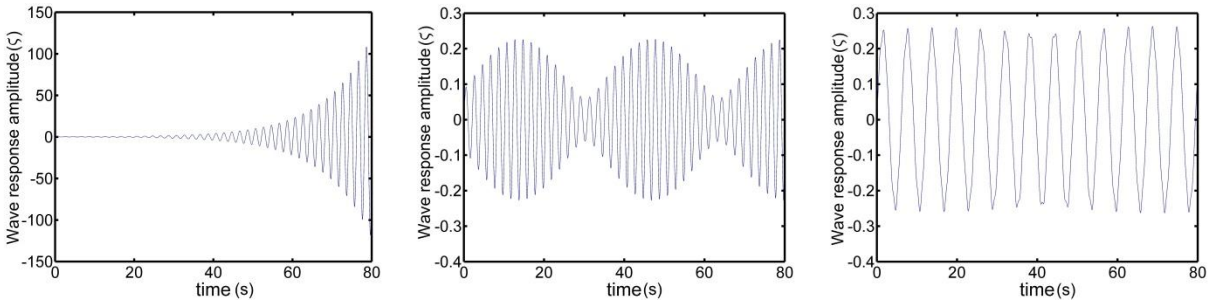

(a) *(b)* *(c)*

Figure 2.2: (a) Unstable, (b) critically stable and (c) stable interface oscillation for an ideal fluid.

The inviscid theory for Faraday waves is helpful for understanding the fundamental physical behaviour, including mode dispersion. For a closed cell experimental condition, each amplitude and frequency gives a point on the stability chart, and one can determine whether solution is stable or unstable,

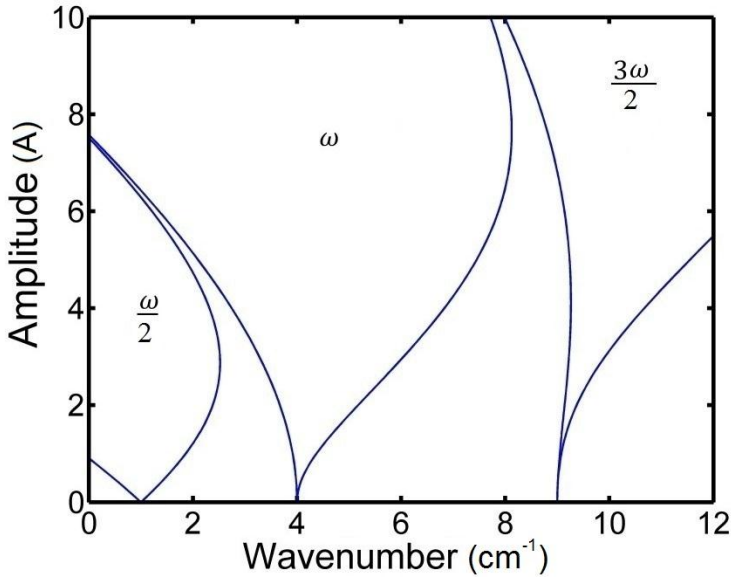

Figure 2.3: Stability chart for Mathieu Equation, where ω/2, ω, 3ω/2 represent oscillation period of standing Faraday waves with one-half, one, and three half of the imposed frequency.

By determining such a solution, one can also determine the stability boundaries. For the infinite bilayer fluids case shown in Fig. 2.1, one can define amplitude versus wave number graph for each imposed frequency as shown in Fig. 2.3. As for a particular geometry of confined cell, the

generation of waves is constrained by its boundaries. In a closed cell, the dimensions of the cell play an important role as it allows waves with certain wave numbers only. This means that an unstable solution is constrained with a certain set of frequency and certain wavenumbers depending on the cell geometry and size.

However, the above theory cannot be used for the current problem as the viscous effect is lacking in this model, and the effect of fluid viscosity cannot merely be integrated with linear damping into the Mathieu equation. Another reason corresponds to the boundary conditions restrictions and the allowed wavenumbers. High parametric frequencies have very small spacing between any two allowed wavenumbers and thus form a continuum system. However, this thesis is focused on low frequency excitation where the wavenumbers allowed by the system form a discretized set and are strongly dependent upon the boundary conditions and the lateral geometry of the container.

2.2 Viscous fluid bilayer subjected to perpendicular vibration

This section is an extension solution towards parametric excitation of inviscid fluid. In experiments the fluid viscosities cannot be ignored and thus an inviscid theory cannot work very precisely. To develop a more inclusive theory with a viscous system, a linear stability is modelled for Newtonian incompressible viscous fluid layers in order to relate theory with experiments. A single mode excitation has been derived from the Navier-Stokes equations, taking the true nature of the fluid system. The nonlinear equations were linearized with determined base state solution and forced excitation. The equations were solved for neutral stability conditions in order to obtain critical threshold – wavenumber curves. This was achieved by a Fourier-Floquet eigenvalue method and solved numerically by a matrix system. The current model considers an initial stable flat horizontal interface separating two distinct fluids, assuming no stresses for horizontally finite size system (see Fig. 2.4). Wavenumbers were then calculated based on finite cell size used in experiments.

The base state was stable with horizontally flat interface separating two distinct fluids. The stress-free boundary condition was assumed when horizontally finite system conditions were applied to these results, constraining on the allowed wavenumbers by the system. A case study has been presented discussing effects of various parameters like interfacial tension, viscosity, gravity to understand fluid behaviour in different circumstances.

2.2.1 Governing Equations

A horizontal infinite fluid bilayer with depths h_1 and h_2 of the two fluids and interface at z = 0 is submitted to a forced oscillation in the direction of gravity (See Fig 2.4).

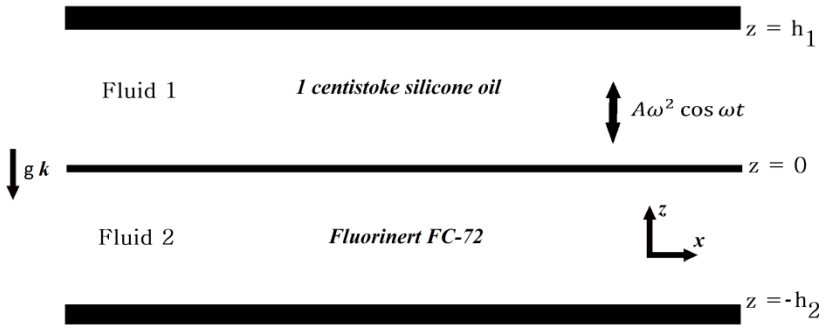

Figure 2.4: Sketch of the geometry for the linear stability analysis for Faraday instability- Two-fluids infinite bilayer system.

Equations of motion for Newtonian incompressible fluid in fix frame can be written as,

$$\rho_j \left(\partial_t \boldsymbol{V_j} + \boldsymbol{V_j} \cdot \nabla \boldsymbol{V_j}\right) = -\nabla P_j + \mu_j \nabla^2 \boldsymbol{V_j} + \rho_j g \, \boldsymbol{k} \tag{2.2}$$

Where $\boldsymbol{V_j}$ is the velocity vector field of the fluids, P_j is the pressure field, ρ_j is the density with j = 1 defining for upper fluid and j = 2 for lower fluid, g is the gravity acceleration,

For simplicity we investigate the system in the moving frame, for transformation from fix frame to moving frame space coordinate equations can be written as,

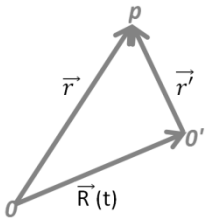

Where 0 is the origin of fix frame, 0' is the origin of moving frame and p is a point in fluid system

$$\boldsymbol{r} = \boldsymbol{r'} + \boldsymbol{R}(t)$$

$$\frac{d\boldsymbol{r}}{dt} = \frac{d\boldsymbol{r'}}{dt} + \frac{d\boldsymbol{R}(t)}{dt}$$

$$\boldsymbol{V} = \boldsymbol{V'} + \boldsymbol{U}(t)$$

$$\nabla \boldsymbol{V} = \nabla\, \boldsymbol{V'}$$

$$\boldsymbol{V} \cdot \nabla \boldsymbol{V} = (\boldsymbol{U}(\boldsymbol{t}) + \boldsymbol{V'}).(\nabla\, \boldsymbol{V'}) \tag{2.3}$$

Rewriting equation 2.2 in a moving frame,

$$\rho_j \left(\partial_t\, (\boldsymbol{U} + \boldsymbol{V'})_{\boldsymbol{j}} + \left(\boldsymbol{U}(\boldsymbol{t}) + \boldsymbol{V'}_{\boldsymbol{j}}\right).(\nabla\, \boldsymbol{V'})_{\boldsymbol{j}}\right) = -\nabla P_j + \mu_j\, \nabla^2 \boldsymbol{V}_{\boldsymbol{j}} + \rho_j g\, \boldsymbol{k}$$

which gives,

$$\rho_j \left(\partial_t\, \boldsymbol{V'}_{\boldsymbol{j}} + (\boldsymbol{V}_{\boldsymbol{j}}.\nabla)\boldsymbol{V}_{\boldsymbol{j}}\right) = -\nabla P_j + \mu_j\, \nabla^2 \boldsymbol{V}_{\boldsymbol{j}} + \rho_j g\, \boldsymbol{k} - \rho_j \frac{d\boldsymbol{U}(t)}{dt} \boldsymbol{k}$$

And finally,

$$\rho_j \left(\partial_t\, \boldsymbol{V}_{\boldsymbol{j}} + (\boldsymbol{V}_{\boldsymbol{j}}.\nabla)\boldsymbol{V}_{\boldsymbol{j}}\right) = -\nabla P_j + \mu_j\, \nabla^2 \boldsymbol{V}_{\boldsymbol{j}} + \rho_j (g - A\omega^2 \cos \omega t)\, \boldsymbol{k} \tag{2.4}$$

The applied acceleration on the system has been calculated as,

$$x(t) = A \cos \omega t$$

$$v(t) = -A\omega \sin \omega t$$

$$a(t) = -A\omega^2 \cos \omega t \tag{2.5}$$

Where *A* is the amplitude and ω is the frequency.

The equation of conservation of mass can be written as,

$$\nabla \cdot \mathbf{V_j} = 0 \tag{2.6}$$

Vibrational acceleration will become an additional term in the equations of motion by relocating equation into a moving reference frame through velocity transformation (see equation 2.4) giving acceleration which is in the direction of the gravity. This leads to an effective gravitational acceleration to the fluids.

No-slip conditions are applicable at the top and bottom walls and continuity of velocity is applied at the interface. The momentum balance at the interface is,

$$M = \rho_1 (\boldsymbol{V_1} - \boldsymbol{U}) \cdot \boldsymbol{n} = \rho_2 (\boldsymbol{V_2} - \boldsymbol{U}) \cdot \boldsymbol{n} \tag{2.7}$$

here M is the momentum, $\boldsymbol{V_1}, \boldsymbol{V_2}$ are velocity of fluid 1 and 2 respectively. For an immiscible fluid system momentum is zero ($M = 0$) at the interface. Here $\boldsymbol{U}$ is the speed of fluid interface, and $\boldsymbol{n}$ is the surface normal to the interface. The surface is given explicitly as the set of points (x, y) satisfying the function $Z(\mathrm{x}, \mathrm{y}, \mathrm{t})$. Then a normal at a point $(\mathrm{x}, \mathrm{y}, \mathrm{z})$ on the surface is given by $\nabla F(\mathrm{x}, \mathrm{y}, \mathrm{z})$ where $F(\mathrm{x}, \mathrm{y}, \mathrm{z}, \mathrm{t})$ is the implicit form of the evolution of the interface and is defined by $F(\mathrm{x}, \mathrm{y}, \mathrm{z}) = z - Z(\mathrm{x}, \mathrm{y}, \mathrm{t}) = 0$. The unit vector of surface normal can be defined by $\boldsymbol{n} = \nabla F(\mathrm{x}, \mathrm{y}, \mathrm{z}) / |\nabla F(\mathrm{x}, \mathrm{y}, \mathrm{z})|$ which can also be expressed by,

$$\boldsymbol{n} = \frac{\nabla [\mathrm{z} - \mathrm{Z}(\mathrm{x}, \mathrm{y}, \mathrm{t})]}{|\nabla [\mathrm{z} - \mathrm{Z}(\mathrm{x}, \mathrm{y}, \mathrm{t})]|} = \frac{\boldsymbol{k} - Z_x \boldsymbol{i} - Z_y \boldsymbol{j}}{\sqrt{(1 + {Z_x}^2 + {Z_y}^2)}} \tag{2.8}$$

Jump momentum balance from equation 2.7 can be reduced to,

$$\boldsymbol{V_j} \cdot \boldsymbol{n} = \boldsymbol{U} \cdot \boldsymbol{n}$$

$$\boldsymbol{V_j} \cdot \boldsymbol{n} = \mathrm{U}\, \boldsymbol{n} \cdot \boldsymbol{n}$$

$$\boldsymbol{V_j} \cdot \boldsymbol{n} = \mathrm{U} \tag{2.9}$$

The differential for the motion of the interface in an infinitesimal time δt can be written as,

$$\lim_{\delta t \to 0}\left[\frac{Z\,(x,y,z,t+\delta t) - \ Z\,(x,y,z,t)}{\delta t}\right] = \frac{\partial Z}{\partial t} + \frac{\partial Z}{\partial x}\frac{\partial x}{\partial t} + \frac{\partial Z}{\partial y}\frac{\partial y}{\partial t} + \frac{\partial Z}{\partial z}\frac{\partial z}{\partial t}$$

$$0 = \frac{\partial Z}{\partial t} + \boldsymbol{U} \cdot \nabla Z$$

$$0 = \frac{\partial Z}{\partial t} + \mathrm{U}\boldsymbol{n} \cdot \boldsymbol{n}\,|\nabla Z|$$

$$0 = \frac{\partial Z}{\partial t} + \mathrm{U}\,|\nabla Z|$$

Replacing U with $\mathbf{V_j} \cdot \boldsymbol{n}$ from equation 2.9 and expanding normal vector,

$$\frac{\partial Z}{\partial t} = -\,\mathbf{V_j} \cdot \boldsymbol{n}\,|\nabla Z| \tag{2.10}$$

which can be written as,

$$\partial_t Z = V_z - \ V_x Z_x - \ V_y Z_y \ \text{ at } z = Z(x,y,t) \tag{2.11}$$

The next step is to derive the normal and tangential stress boundary conditions fitting at a fluid interface defined in terms of interfacial tension γ. Consider an infinitesimal surface area closed by a contour and forming an infinitesimal volume. Forces present in this tiny body are inertial forces associated with acceleration of fluid within small volume balanced by body forces acting on fluid within the infinitesimal volume, hydrodynamic force exerted at the interface by the fluid from both sides and surface tension force exerted along perimeter. Hence surface force must balance hydrodynamic force. Thus, the stress balance equation can be defined as hydrodynamic force equal to force exerted by surface tension along the interface,

$$\boldsymbol{n} \cdot \boldsymbol{T_1} - \ \boldsymbol{n} \cdot \boldsymbol{T_2} = \gamma \boldsymbol{n}(\nabla \cdot \boldsymbol{n}) - \ \nabla\gamma \tag{2.12}$$

where,

$\boldsymbol{n} \cdot \boldsymbol{T_1}$ Stress (force/area) exerted by the upper layer on the lower layer,

$\boldsymbol{n} \cdot \boldsymbol{T_2}$ Stress (force/area) exerted by the lower layer on the upper layer,

$\boldsymbol{T_1}, \boldsymbol{T_2}$ are the stress tensors defined as $\boldsymbol{T_j} = \ -P\mathbf{I} + \ \mu\,(\nabla \boldsymbol{V_j} + (\nabla \boldsymbol{V_j})^T)$

$\gamma \boldsymbol{n}\, 2H$ Normal curvature force per unit area associated with local curvature of interface and where 2H is twice the mean surface curvature and defined as,

$$2H = \nabla \cdot \boldsymbol{n}$$

$$2H = \nabla \cdot \frac{\nabla\ [\mathrm{z} - \mathrm{Z}\ (\mathrm{x}, \mathrm{y}, \mathrm{t})]}{|\nabla\ [\mathrm{z} - \mathrm{Z}\ (\mathrm{x}, \mathrm{y}, \mathrm{t})]|}$$

$$2H = \nabla \cdot \frac{\nabla \mathrm{Z}}{\sqrt{1 + |\nabla \mathrm{Z}|^2}}$$

$$2H = \frac{\nabla^2 \mathrm{Z}}{\sqrt{1 + |\nabla \mathrm{Z}|^2}} + \frac{\nabla \mathrm{Z} \cdot (-\frac{1}{2} \nabla\, |\nabla \mathrm{Z}|^2)}{(1 + |\nabla \mathrm{Z}|^2)^{3/2}}$$

$$2H = \frac{\nabla^2 \mathrm{Z}\ (1 + |\nabla \mathrm{Z}|^2) - \frac{1}{2} \nabla \mathrm{Z} \cdot \nabla\, |\nabla \mathrm{Z}|^2}{(1 + |\nabla \mathrm{Z}|^2)^{3/2}} \qquad (2.13)$$

$\nabla \gamma$ tangential stress associated with gradients in surface tension.

A surface with curvature $2H$ reflects a jump in normal stress across the interface. Normal stress balance can be obtained by having dot product of normal vector to stress balance equation. The jump in normal stress across the interface must balance the curvature force per unit area,

$$\boldsymbol{n} \cdot \boldsymbol{T_1} \cdot \boldsymbol{n} - \boldsymbol{n} \cdot \boldsymbol{T_2} \cdot \boldsymbol{n} = \gamma 2H$$

$$[-P_1 \mathbf{I} + \mu_1\ (\nabla \boldsymbol{V_1} + (\nabla \boldsymbol{V_1})^T)] - [-P_2 \mathbf{I} + \mu_2 (\nabla \boldsymbol{V_2} + (\nabla \boldsymbol{V_2})^T)] = \gamma 2H$$

Again multiplying by normal vector,

$$[[-P_1 \boldsymbol{I} + \mu_1\ (\nabla \boldsymbol{V_1} + (\nabla \boldsymbol{V_1})^T)] - [-P_2 \boldsymbol{I} + \mu_2 (\nabla \boldsymbol{V_2} + (\nabla \boldsymbol{V_2})^T)]] \cdot \boldsymbol{n} = \gamma 2H \boldsymbol{n}\ at\ z = Z\ (x, y, t) \qquad (2.14)$$

where γ is the interfacial tension and 2H is twice the mean surface curvature. The stress balance at the interface defined above in equation 2.14 gives a relation between pressure and viscous tangential stress difference balanced by the force arising from surface curvature.

For observing the instability to occur as a transition from a quiescent state of no flow or no interfacial deflection to a state of flow, a perturbation is introduced in velocity, pressure and space in the above equations by considering an infinitesimal perturbation of order ε of this quiescent state,

$$\begin{aligned} \boldsymbol{V_j} &= \varepsilon \boldsymbol{v_j} \\ p_j &= p_0 + \varepsilon p_j \\ Z &= \varepsilon \zeta \end{aligned} \tag{2.15}$$

where the base state velocity and initial interfacial deflection are zero. Introducing these perturbations and solving for same order leads to no-flow base state leads to,

$$\rho_j \left(\partial_t \, \varepsilon \boldsymbol{v_j} + \varepsilon^2 \, \boldsymbol{v_j}.\nabla \boldsymbol{v_j}\right) = -\nabla(p_{0_j} + \varepsilon p_j) + \mu_j \nabla^2(\varepsilon \boldsymbol{v_j}) + \rho_j(g + A\omega^2 \cos \omega t)\, \boldsymbol{k} \tag{2.16}$$

Gravitational modulation is balanced by a vertical pressure gradient as shown below with perturbed equation 2.17. For a small perturbation ($\varepsilon \rightarrow 0$),

$$\begin{aligned} 0 &= -\nabla p_{0_j} + \rho_j(g + A\omega^2 \cos \omega t)\, \boldsymbol{k} \\ \partial_z \, p_{0_j} &= \rho_j(g + A\omega^2 \cos \omega t) \end{aligned} \tag{2.17}$$

To map the variables from the unknown interface positioned to z = 0, a collection of the $O(\varepsilon)$ terms in perturbed equation 2.15 produces the linearized domain problem,

$$\rho_j \partial_t \boldsymbol{v_j} = -\nabla \mathrm{p}_j + \mu_j \nabla^2 \boldsymbol{v_j} \tag{2.18}$$

Kinematic condition arising from the interface position and fluid velocity produced by stress balance at z=0 from equation 2.11 leads to,

$$\partial_t \zeta = w \tag{2.19}$$

where w is the z-component of the velocity.

Perturbing stress balance equation 2.14,

$$\left[\!\left[(-p_j + \zeta\,\partial_z p_0)\mathbf{I} + \mu_j(\nabla \boldsymbol{v_j} + \left(\nabla \boldsymbol{v_j}\right)^T)\right]\!\right] \cdot \boldsymbol{n} = \gamma \nabla^2 \zeta \mathbf{n} \tag{2.20}$$

Thus with equation 2.19 and 2.20, tangential stress can be balanced on the interface as,

$$\mu_1(\partial_{zz} - \nabla^2{}_H)w_1 = \mu_2(\partial_{zz} - \nabla^2{}_H)w_2 \qquad at\ z = 0 \tag{2.21}$$

where $\nabla^2{}_H = (\partial^2/\partial_{x^2} + \partial^2/\partial_{y^2})$ is the horizontal Laplacian. The normal component of stress becomes,

$$\left[\!\left[-p_j + \zeta\,\partial_z p_0 + 2\mu_j \partial_z w_j\right]\!\right] = \gamma \nabla^2 \zeta \qquad \text{at z} = 0 \tag{2.22}$$

Combining kinematic condition, stress balance and continuity equation and applying $\nabla^2{}_H$ leads to,

$$\left[\!\left[(-\rho_j \partial_t + \mu_j \nabla^2 + 2\mu_j \nabla^2{}_H)\partial_z w_j + \rho_j(g + A\omega^2 \cos \omega t)\nabla^2{}_H \zeta\right]\!\right] = \gamma \nabla^4 \zeta \quad at\ z = 0 \tag{2.23}$$

The temporal evolution of this equation for given imposed amplitude A and frequency ω ultimately determines the stability of the linear system. In equation 2.23, subscript *j* is defined for fluid 1 and 2.

2.2.2 Linear Stability Analysis

The stability problem was solved by Floquet theory as effective gravitational acceleration is periodic in time. The periodicity of the system was accounted by including a coefficient of $e^{n\omega t}$. Solutions were assumed in Floquet form in terms of coefficient $\sigma + i\alpha$, where σ is the complex

growth rate, in the infinite Fourier series. The Fourier series were written as follows, (indices *j* has been omitted to simplify the writing of the equations),

$$\varphi_{(1,2)} = e^{i(k_x x + k_y y)} \sum_{n=-\infty}^{\infty} e^{[\sigma + i(\alpha + n\omega)]t}\, \hat{\varphi}_{(1,2)_{\boldsymbol{n}}}(z) \tag{2.24}$$

Where $\varphi = (w, \zeta)$, k is a two-dimensional horizontal wavenumber and are defined as $k^2 = k_x^2 + k_y^2$ for a rectangular system. The response frequency α is always chosen in the range 0 to ½ ω. As Kumar & Tuckerman (1994) discussed, only α = 0 (harmonic) and α = ½ ω (sub-harmonic) lead to instability; for all other values of α, the interface was completely stable. Eliminating the pressure field, by taking the $\nabla \times \nabla \times$ of the 0th order perturbed Navier-stokes equation and combining with continuity equation, we get,

$$(\rho\, \partial_t - \mu \nabla^2)\nabla^2 \boldsymbol{V} = 0 \tag{2.25}$$

Solution of above equation by introducing expanded Fourier series are the fourth-order ordinary differential equation governing each Fourier mode, n, for w,

$$[\sigma + i(\alpha + n\omega) - \frac{\mu}{\rho}(\partial_{zz} - k^2)](\partial_{zz} - k^2) w_n = 0 \tag{2.26}$$

to which the solution can be written as,

$$w_n = a_n e^{kz} + b_n e^{-kz} + c_n e^{b_n z} + d_n e^{-b_n z} \tag{2.27}$$

where

$$b_n{}^2 = k^2 + \frac{\sigma + i(\alpha + n\omega)}{\mu/\rho} \tag{2.28}$$

Conditions for no-flow and no-slip boundary conditions on the top and bottom surfaces $z = h_1$ and $z = -h_2$ respectively for fluid 1 and 2 are,

$$w_{(1,2)n} = \partial_z w_{(1,2)n} = 0 \tag{2.29}$$

Boundary conditions at interface z = 0 are,

$$\begin{aligned} w_{1n} &= w_{2n} = (\sigma + i(\alpha + n\omega))\zeta_n \\ \partial_z w_{1n} &= \partial_z w_{2n} \\ \mu_1(\partial_{zz} w_{1n} + k^2) &= \mu_2(\partial_{zz} w_{2n} + k^2) \end{aligned} \tag{2.30}$$

Inserting boundary conditions (equation in 2.30) into equation 2.23 leads to,

$$\begin{aligned} \left[\!\left[(-\rho_j(\mu + i(\alpha + n\omega)) + 3\mu_j k^2) + \partial_z w_n - \mu_j \partial_{zzz} w_n\right]\!\right] + (\Delta\rho g - \gamma k^2)k^2\zeta_n \\ = A\omega^2 \frac{\Delta\rho k^2}{2} (\zeta_{n+1} - \zeta_{n-1}) \end{aligned} \tag{2.31}$$

Here identity $\cos \omega t = \frac{1}{2}(e^{i\omega t} + e^{-i\omega t})$ is used giving relation of ζ_n mode to ζ_{n+1} and ζ_{n-1} modes. Truncated to a finite number of modes N, with the growth constant σ set to zero, the stability of the linearized problem can be casted as an eigenvalue problem for solutions of neutral stability and their corresponding eigenvalues being the amplitudes A at which they occur. They can be expressed as

$$D\varsigma = AB\varsigma \tag{2.32}$$

Here, matrix D is generated from left hand side of equation 2.32 and operates on eigenvector ς. The response frequency is set to zero for harmonic solution and ½ ω for sub harmonic solution. The matrix B is a double banded matrix of largely 1's and 0's used to select the coupled modes ζ, but differs slightly for the n = 0 mode. Truncation from n=0 to N results in the inclusion of the

ζ_{-1} coefficient in the matrix B for the n = 0 mode and is replaced with the conjugate $\overline{\zeta_1}$ for α = 0 and $\overline{\zeta_0}$ for α = ½ ω.

2.2.3 Spatially infinite system results

The linear equations defined above can be solved for all wavenumbers and solutions to produce a set of tongues of instability which is similar to the fins produced by the Mathieu equation in case of inviscid flow but tips are smoothed due to viscous effects and not descending to zero amplitude (Benjamin and Ursell, 1954). The viscosity affects harmonic or higher harmonic solution much more compared to sub-harmonic node.

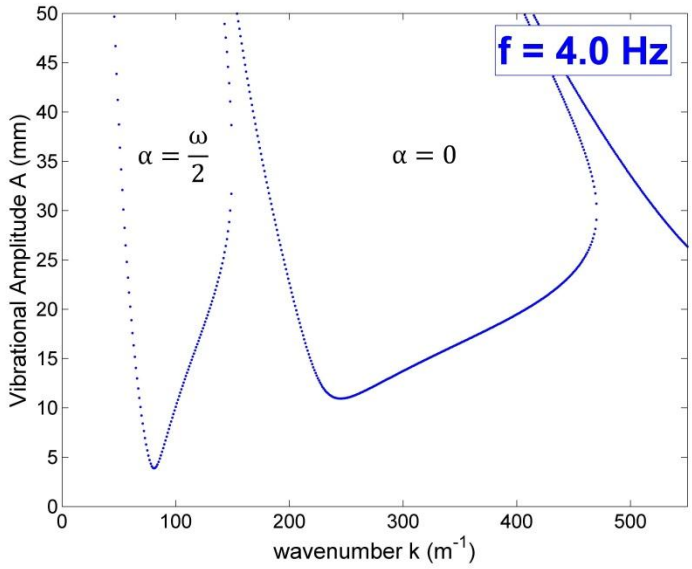

Figure 2.5: Threshold amplitude vs wave number for a horizontally infinite bilayer for a fixed frequency of 4 Hz, the first node from left represents sub harmonic (=ω/2) solution, the second node harmonic (α=ω), the third node super harmonic (α=3ω/2) and so on…

The first tongue is the solution of sub-harmonic node, the second as harmonic, the third as super-harmonic etc…, as the waves excited in these regions execute one-half, one, and three-

half periods etc..., with regards to the applied frequency, respectively. In an experimental condition, the wavenumber with the lowest threshold amplitude would be excited first in the direction of increasing vibrational amplitudes. This lowest amplitude is called as critical threshold amplitude. In an experimental system that approaches the laterally infinite limit like that of Bechhoefer *et al.* (1995), the lowest threshold amplitude of sub-harmonic node would always be the point of critical threshold amplitude. Thus for a large system only sub harmonics results are observed as had been observed by Faraday (1831) and Rayleigh (1883). Increments in frequency force tongues towards right and downward as will be explained in detail in the next section of this Chapter. For infinite system such as shown in Fig. 2.4, critical threshold amplitude – frequency curve takes the shape of smooth hyperbola with infinite number of available modes and excited for the natural frequency corresponding to the excited mode (see Fig 2.6). The MATLAB code has been made accessible in appendix C.

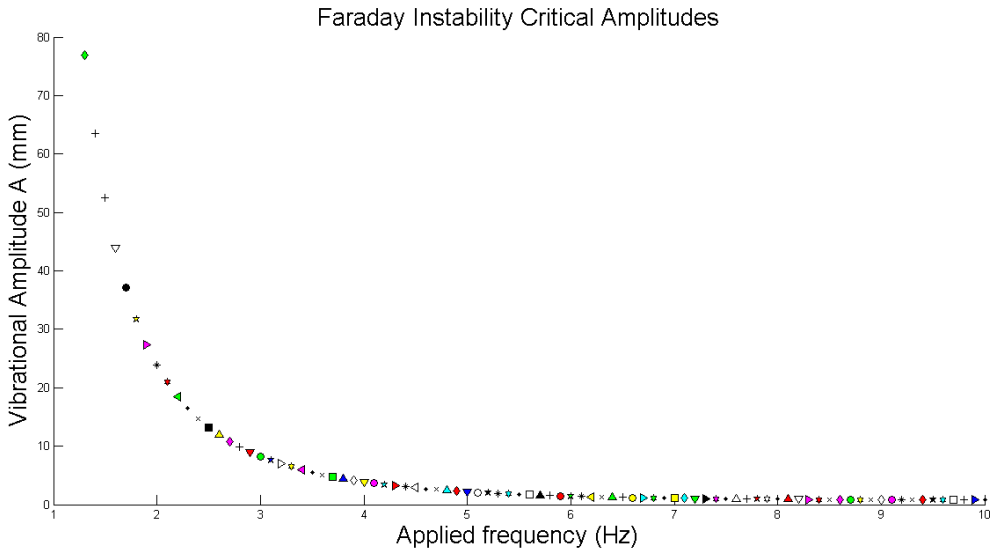

Figure 2.6: Critical threshold amplitude for infinite boundary system for a bilayer problem. All symbols define different modes.

2.2.4 Results in finite systems

Extension of the previous model to the case of a finite size cell was outlined by Benjamin & Ursell (1954) for rectangular cross-sections. For a system with a rectangular cross-section of width W and breadth L, the surface waves must satisfy the following boundary conditions,

$$\frac{\partial \zeta}{\partial x} = 0 \; and \; \frac{\partial \zeta}{\partial y} = 0 \tag{2.33}$$

where ζ is the deformation of interface (see equation 2.14). These constraints can be applied on all sidewalls (*x=0, W* and *y=0, L*). Finite size allowed wave numbers can then be calculated as,

$$k = \sqrt{\left(\frac{\pi m}{W}\right)^2 + \left(\frac{\pi n}{L}\right)^2} \tag{2.34}$$

where m, n are modes in *x* and *y* directions (for Hele-Shaw cell size such as used in present experiments, modes in the direction of width always remain zero for low frequency range. Thus here, for example, mode 1, mode 2 are referred to (m,n) as (0,1) and (0,2) respectively). Figure 2.6 shows solutions of theoretical model for critical amplitude vs wavenumber. Each tongue represents a parametric solution such as subharmonic, harmonic, super harmonic and so on.

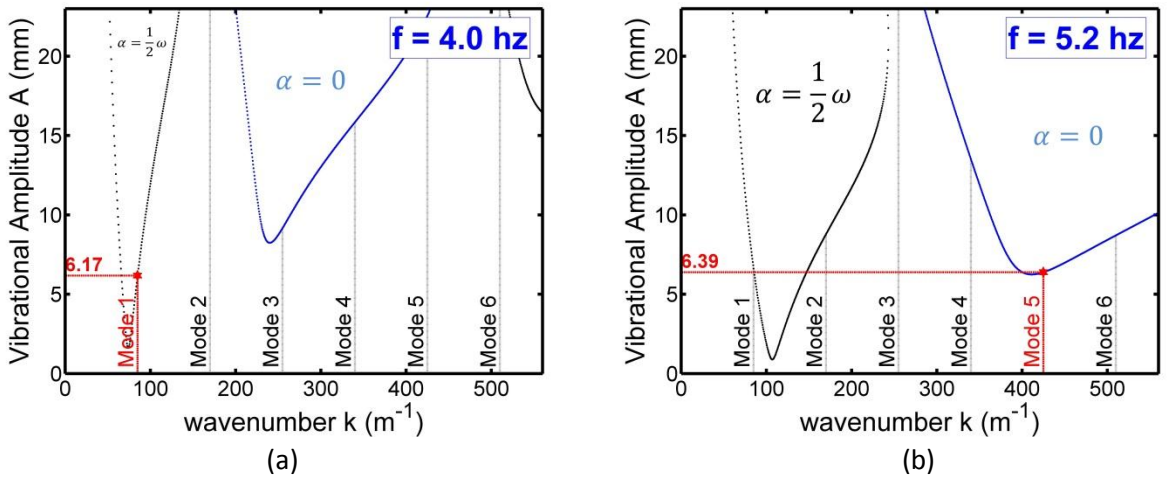

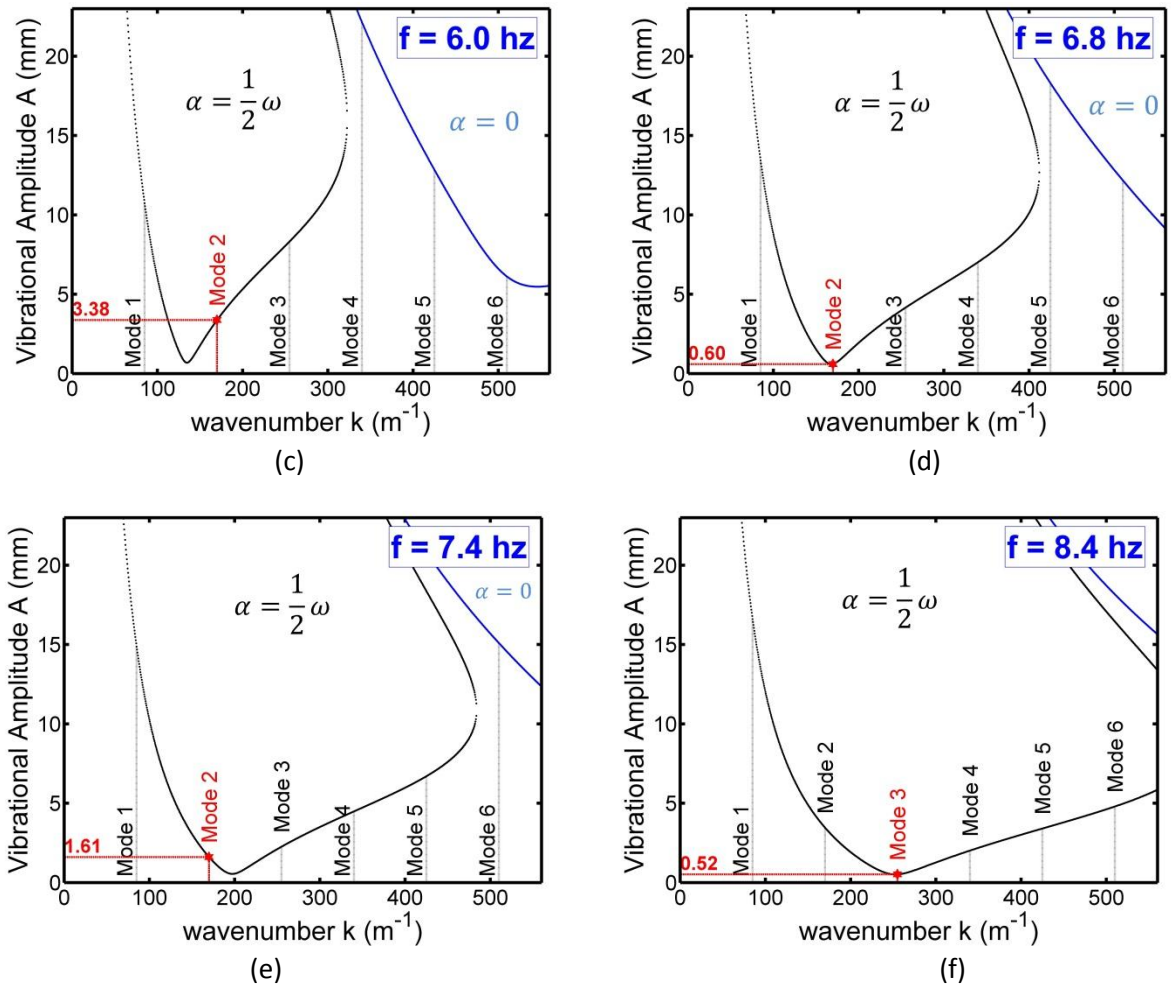

Figure 2.7: Representation of the different modes of the finite sized cell in the amplitude-wavenumber diagram for immiscible fluids system and in ground-based cases for FC-72 and 1 cSt silicone oil at 25 ^{o}C.

In high frequency system subharmonic solutions dominates over higher harmonic ones. However in lower frequency domain higher harmonic solution can appear in the cell. The vertical lines in Figure 2.7 represent excitable modes as per the cell size (defined in Eq. 2.34). The minimum amplitude of the possible solution is called the critical or the threshold amplitude for the particular frequency. This critical amplitude can be plotted against frequency in a different map in Figs. 2.8 where each mode has its own cup shape node with its own distinct wave number (presented in this Figure with different colours). The cup size (amplitude and frequency band) decreases with the increase in frequency and nodes in critical threshold

amplitude – wavenumber curves (see Figs. 2.7 and 2.8). The subharmonic solution dominates and the system becomes less stabilized. Patterns at higher frequencies correspond to situations where the range of modes is effectively continuous. If a curve is drawn with all minimum values from Fig. 2.8, it will represent the threshold curve in the absence of mode quantization (similar to curve in Fig. 2.6). Local minima and maxima appear to correspond to different tongues in the amplitude versus wave number graph. A local minima in Fig. 2.8 (say f=6.8 Hz for mode 2) represents the minimum in Fig 2.7(d) in the amplitude versus wave number graph, thus can be called as tuned frequency corresponding to that particular mode. Change from sub-harmonic to harmonic wave or vice versa corresponds to the actual jump of critical threshold from one tongue to another one (see Figs. 2.7 a-c). Harmonic and even more, super-harmonic excitation is uncommon at higher frequencies. But at low frequencies in a discretized system with smaller cell size the system can skip the first sub-harmonic tongue and excite harmonic and super-harmonic modes. The dimensions of the cell in the plane of interface define allowed wave numbers (see Eq. 2.34). As cell size is increased, the difference between one wavenumber to another one vanishes. For practical purposes, we can say that the larger is the cell; the smoother will be the threshold amplitude. In an almost infinite horizontal cell, the discretization of modes will disappear.

Thus for a particular fluid system heated to a defined temperature and vibrated to a fixed oscillation frequency, the needed assignment was to recognize the lowest excitation amplitude for which a discernible interfacial wave occurs. While it is conventional to expect the minimum critical threshold on sub-harmonic tongues in a laterally infinite system, the present confined system is characterized with both harmonic and sub-harmonic modes occurring over discrete bands of frequencies (see Fig. 2.7). And this was due to the fact that finite size system only allows certain wave numbers to appear which are defined by cell dimensions. As we move towards higher frequencies, a continuum of modes becomes easily available even in finite size system, as the mode spacing diminishes even less than the width of each mode. The mode spacing is roughly π/L, while the width of each mode is roughly $\Delta k = \pi/l_{decay}$ (where $l_{decay} \sim \gamma/4\nu\rho\omega$, ν is kinematic viscosity, ρ is density and ω is frequency) as discussed by Bechhoefer *et al.* (1995) The condition for having a continuum of modes is thus equivalent to $L > l_{decay}$.

For practical purpose infinite cell can be designed based on required frequency range. A higher frequency range would require a smaller cell for a similarity with infinite boundary or it can be said that higher frequencies correspond to situations where the range of modes is effectively continuous.

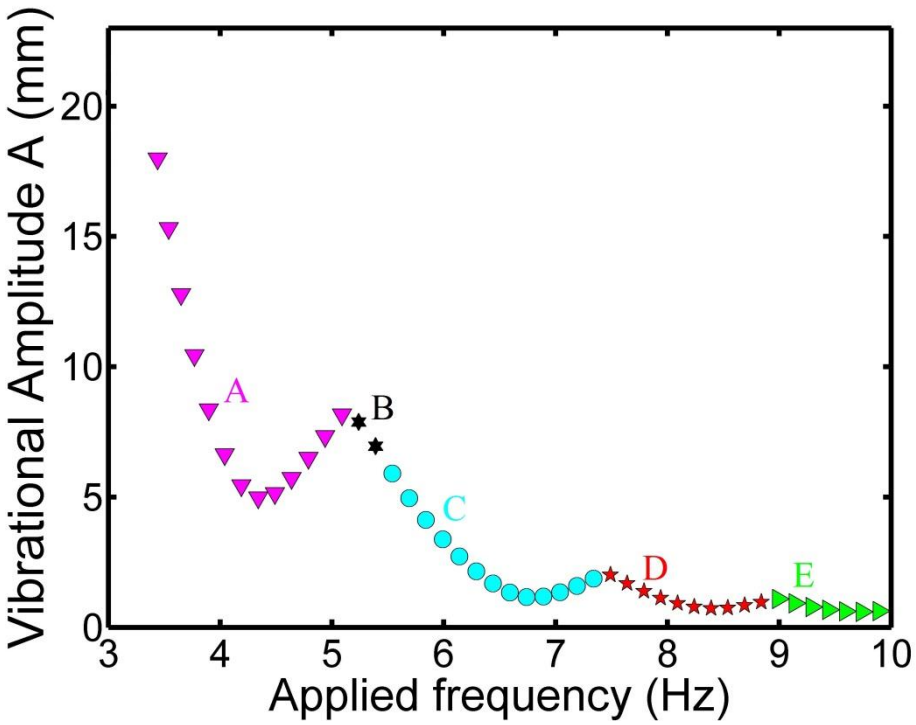

Figure 2.8: Minimum critical thresholds and markers and colours represent modes T=25°C. (For cell size 35mm (L) x 5mm (W) x 29.5mm (H))

2.3 A case study on effects of parameters

Fluid mixtures show a wide variety of properties when studied over extended ranges of temperature and accelerations. Phase equilibrium is one of the most interesting areas of investigation which can provide information on different types of molecular interaction. Faraday instability like any other phenomenon in physics is an outcome of simple properties of the fluids or constituents active in the experimentation. The properties are basically statistical in nature. The common fluid parameters such as density, viscosity, surface tension are prime

for the instability phenomenon as explained earlier, and their effects can help us in comprehending real phenomenon with variables such as gravity, temperature etc. It was thus important to understand that changing these parameters such as temperature will disturb geometric packing fraction of fluid mixture and reduced depth of potential for equal concentration of each liquid component in mixtures. In turn, all fluid properties become a function of temperature. Thus while doing the theoretical analysis for comparison with experiments, corrected values need to be taken into account to understand and validate the phenomenon with theory. Apart from that, a mixture has its own variation in properties because of interaction between molecules of two fluids. Any mixture of two fluids can show affinity (increased intermolecular forces) or aversion between its constituent molecules. For example, current binary fluid set has increased affinity with second fluid with increasing temperature. Variation of properties can also change the volume of fluid or its pressure. In certain physical experiments it was important to keep volume or pressure of the system constant in order to avoid extra uncontrollable presence of variables in the results.

For our binary fluid system, properties of fluids were varying depending on the above cited parameters and are defined based on true measurements of properties with enforced experiment like conditions. With these measurements understanding of binary fluid system has been improved and repeatability of experimental work has been validated.

2.3.1 Mass Transfer in binary fluids: Variation of density

A binary fluid behaviour is a parametrical emphasis of the phase equilibrium of fluid mixture systems. The experimented binary fluid system has a very interesting property of mass transfer when a small variation of temperature was introduced. Binary fluids start moving towards its new equilibrium state which includes partial mixing of one fluid into another. Current binary fluids show an increase in affinity towards each other molecules and change its equilibrium position with increasing temperature. Experiments conducted for current set of liquids (FC-72 &

1 cSt Silicone oil), confirm variation of density due to mixing and have been discussed in this thesis in detail.

To study temperature effects for immiscible fluids (where variation of temperature causes variation of density of top and bottom layers), which was an important aim of this thesis, the variation of density difference becomes an inevitable part of study. Mixing of binary fluids result into decrease in density difference, which in turn is a main parameter of Faraday instability phenomenon. We can simulate this effect by defining a function generating values of ρ_1 and ρ_2 with temperature based on measured and tested values in laboratory settings with controlled temperature conditions (See section 3.3). Decreasing density difference results into a domination of subharmonic waves as can be seen in Figure 2.9 (a)-(c). Another effect of decreasing density gap is the vanishing discretization making the system globally unstable.

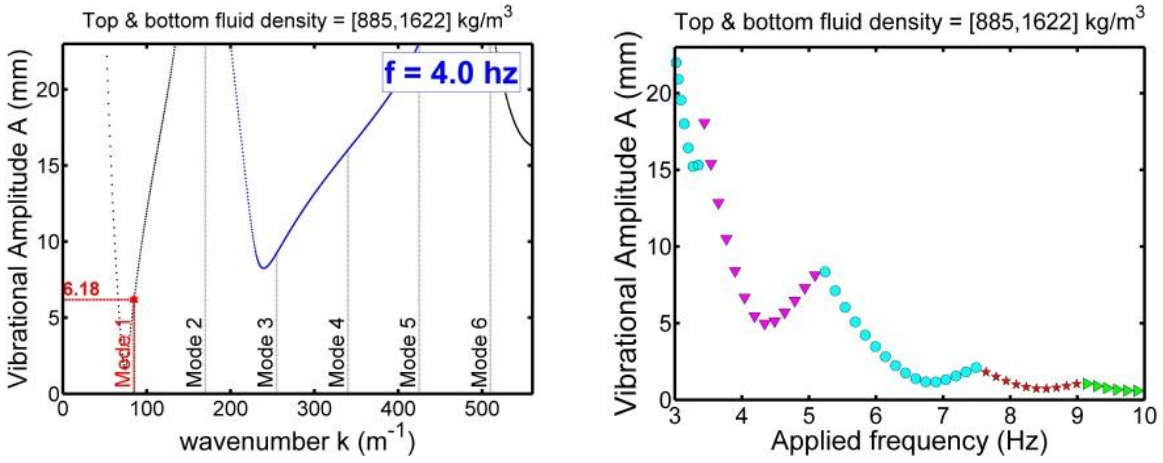

(a)

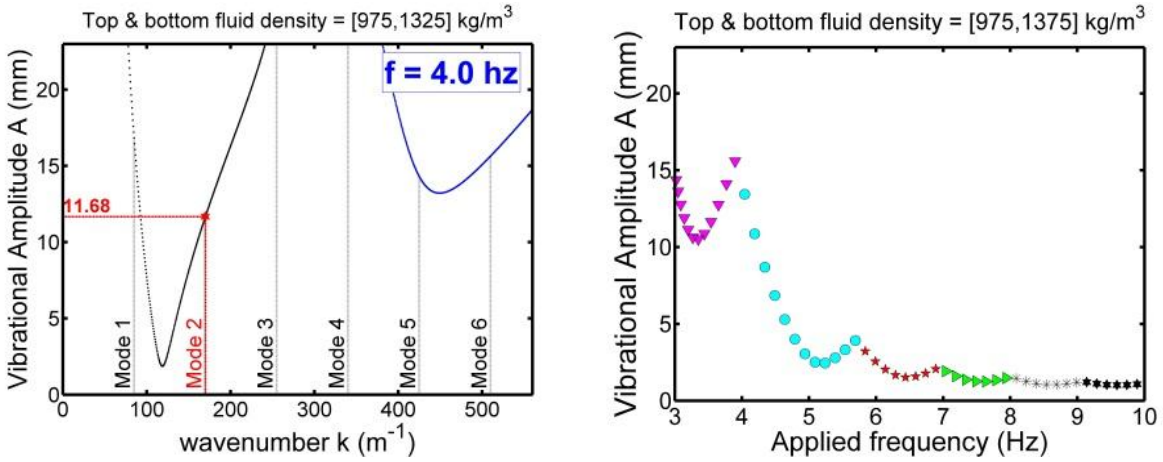

(b)

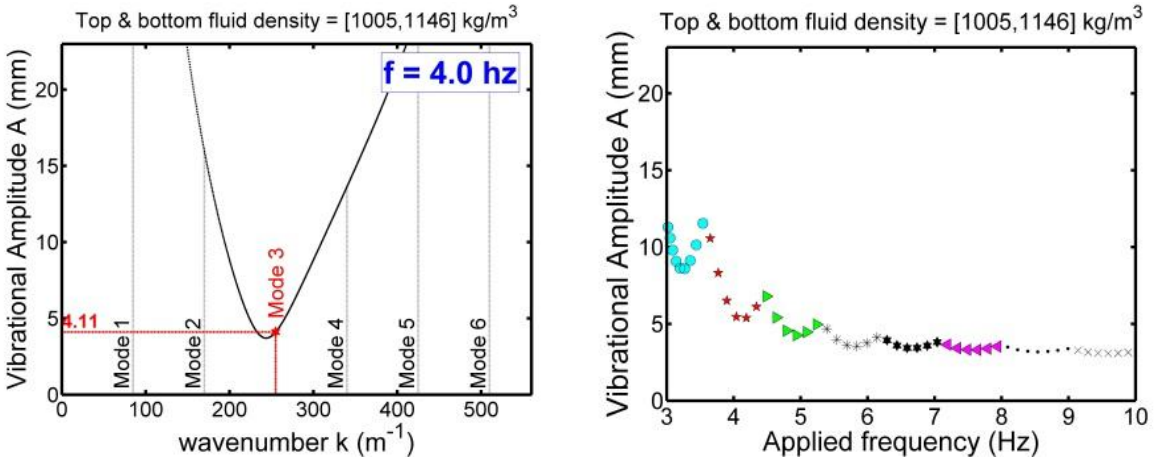

(c)

Figure 2.9: Decreasing density difference for FC-72 and 1cst silicone oil (top to bottom) [μ_1 =20.0 cSt and μ_2 = 12.8 cSt, γ = 2.45 dyne/cm] (a) $\rho_1 = 885\,\frac{\text{kg}}{\text{m}^3}, \rho_2 = 1622\,\frac{\text{kg}}{\text{m}^3}$ (b) $\rho_1 = 975\ \frac{\text{kg}}{\text{m}^3}, \rho_2 = 1325\,\frac{\text{kg}}{\text{m}^3}$ (c) $\rho_1 = 1005\,\frac{\text{kg}}{\text{m}^3}\ , \rho_2 = 1146\,\frac{\text{kg}}{\text{m}^3}$

Interestingly, decreasing density gradient somehow imitates similar effect to decreasing gravity. A low density difference system will have smaller wavelength, smaller critical threshold amplitude and higher probability for sub-harmonic waves. Critical threshold amplitude – frequency graph moves towards left, with a significant reduction in the range of frequency band for each mode, introducing availability of higher modes at same level of frequency. The graph starts to smooth down, indicating the same effect as the decrease in gravity or moving towards infinite side boundary system. This effect was very similar to as seen by Diwakar *et al.* (*Private Communication*) with variation of the fluid's temperatures. A qualitative match of Diwakar *et al.* (*Private Communication*) results in decreasing density behaviour validating the mixing phenomenon present in binary fluid system.

2.3.2 Wall proximity conditions: effects of viscosity

In a small rectangular system, where Faraday wavelength is comparable to the container size, viscous damping plays an important role (effect of cell walls is discussed through the quantization of admissible modes. For a cell with one very small dimension (Hele-Shaw cell), walls have two effects: they force a quantization of the wavenumbers and they create local friction at the boundaries, which is not taken into account in these figures and and will be discussed in section 3.4.2) and basically intensifies the effects of viscosity. Viscous force is a stabilizing agent in the Faraday instability, which can be seen with rise in viscosity causing a damping of the tongues. Increasing amplitude threshold and smoothing of edges as well as movement of tongues slightly towards higher wavenumber can be observed. It is remarkable to note that damping effect on the higher harmonic tongues is more severe as compared to lower harmonics. This can be understood by the fact that increased frequency of waves results into increased friction between fluid molecules. Friction in fluid molecules is proportional to velocity gradients, and velocity gradients are inversely proportional to the wavelength. Thus it can be said that viscous stresses tend to dominate all processes as wavelengths get smaller and smaller.

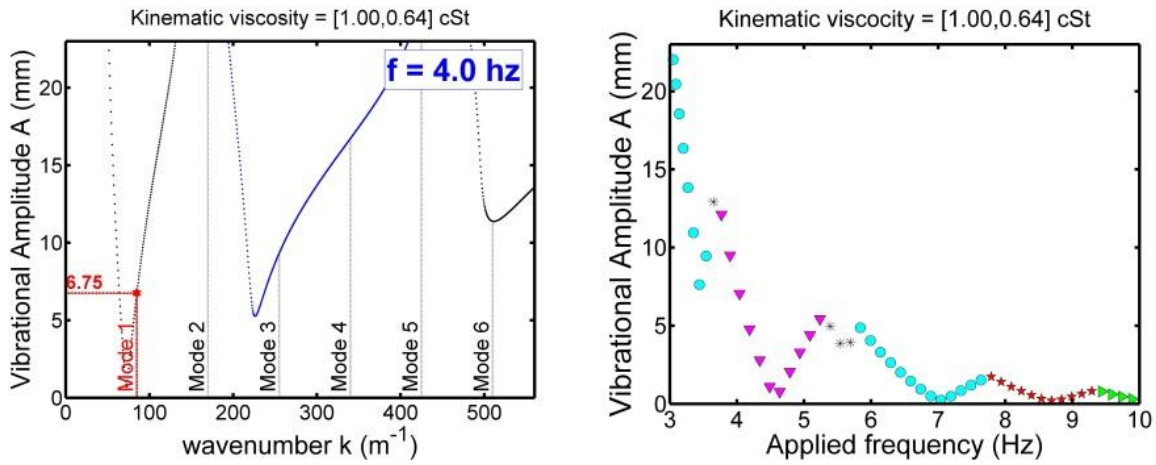

(a)

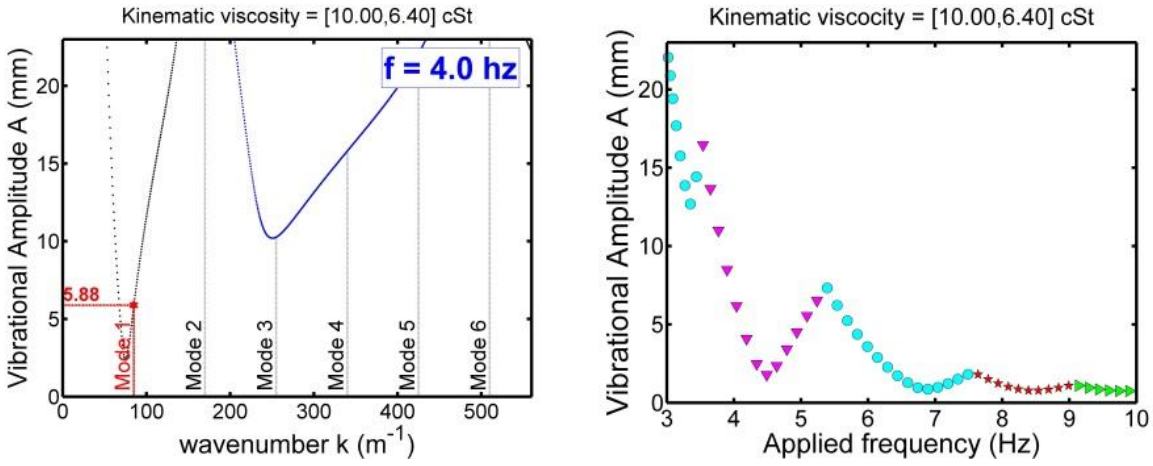

(b)

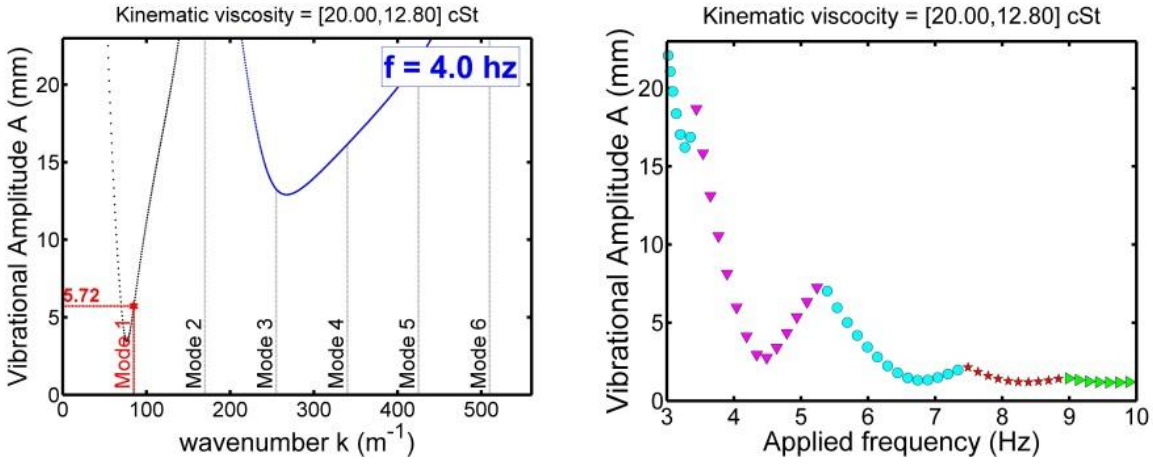

(c)

Figure 2.10: [$\rho_1 = 885\,\frac{\text{kg}}{\text{m}^3}, \rho_2 = 1622\,\frac{\text{kg}}{\text{m}^3}, \gamma = 2.45\ \text{dyne/cm}$] Increasing Viscosity (a) μ_1 = 1.00 cSt, μ_2 = 0.64 cSt (b) μ_1 =10.00 cSt, μ_2 = 6.40 cSt (c) μ_1 =20.00 cSt and μ_2 = 12.80 cSt

In the instability threshold graph it leads to the disappearance of higher harmonics, which can be explained by the presence of choppier waves corresponding to higher harmonics. For a large cell system, even the general viscous theory gives a good match to experiments as shown by Batson *et al.* (2013) utilizing Kumar and Tuckerman (1994) theoretical model. However, it was

not the case with small cell size (rectangular geometry) as explained further in experimental results (see Chapter 3).

Inviscid theory predicts a zero threshold amplitude at resonance (as seen in Figure 2.10(a), first sub-harmonic tongue tuned frequency amplitude is near to zero), whereas the actual waves must get through a viscous threshold. In actual experiments the measured bandwidth was narrow than the inviscid prediction and the measured resonant frequency was larger than the inviscid prediction.

2.3.3 Interfacial conditions: Variation of interfacial forces

While interfacial tension is a stabilizing force and for current set of fluids its effect was negligibly small because of its low value compared to density difference. However, interfacial tension greatly affects solution with higher wavenumbers/ higher harmonic solutions or solutions at lower frequency and act as a stabilizing agent as seen in fig. 2.11. Increase in interfacial tension upturns the probability of harmonic solutions to appear as can be seen in Figure 2.11. In simple terms as described by Benjamin and Ursell (1954), instability is proportional to the sum of gravity and interfacial tension terms,

$$\omega_m \propto \left[\frac{{k_m}^3 \gamma}{\Delta\rho} + k_m g \right]^{\frac{1}{2}} \qquad (2.35)$$

For current system taken in this course of study FC -72 and 1cst silicone oil has small interfacial tension of the order of $\gamma \sim 3.6\, dyne/cm$, $\Delta\rho \sim 10^3\ kg/\mathrm{m}^3$ and gravitation acceleration on earth is $g \sim 9.81\, m/s^2$ and wavenumbers starting from $k_m \sim 150\, m^{-1}$. Introducing these values in above equation shows that the ratio of interfacial term to gravity term was equivalent to 1:100. A liquid set for example water with silicone oil will show more effects for interfacial tension variation.

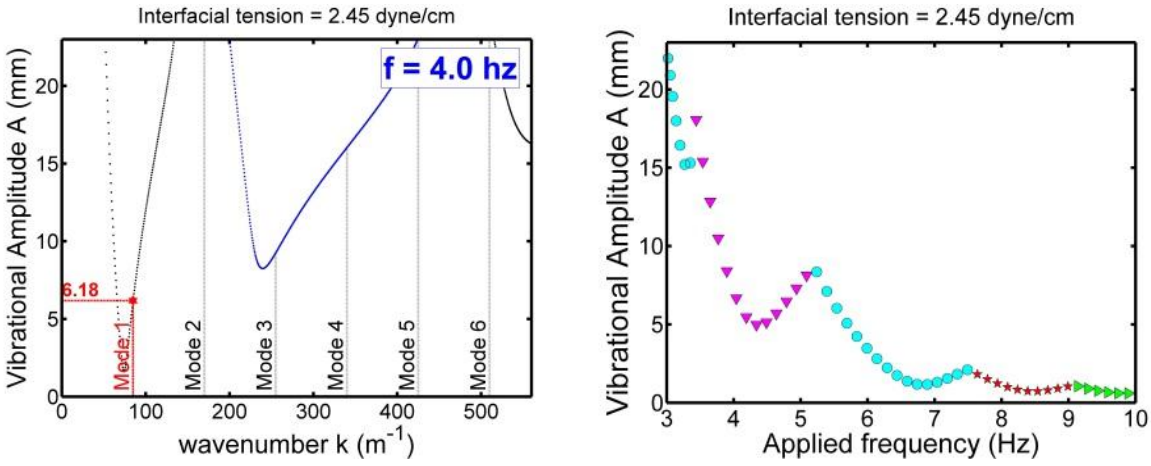
Interfacial tension = 2.45 dyne/cm
f = 4.0 hz
6.18
Mode 1
Mode 2
Mode 3
Mode 4
Mode 5
Mode 6
Vibrational Amplitude A (mm)
wavenumber k (m-1)
Interfacial tension = 2.45 dyne/cm
Vibrational Amplitude A (mm)
Applied frequency (Hz)

(a)

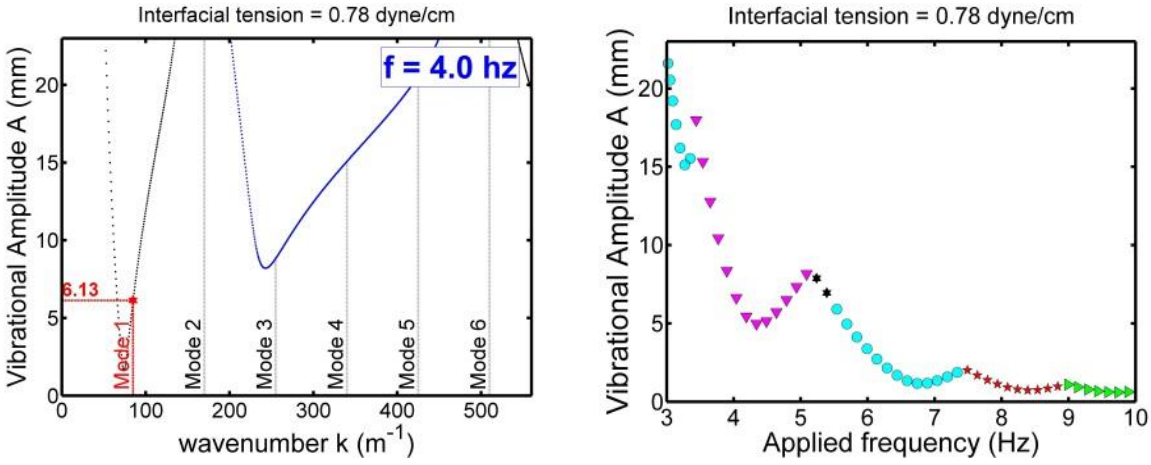
Interfacial tension = 0.78 dyne/cm
f = 4.0 hz
6.13
Mode 1
Mode 2
Mode 3
Mode 4
Mode 5
Mode 6
Vibrational Amplitude A (mm)
wavenumber k (m-1)
Interfacial tension = 0.78 dyne/cm
Vibrational Amplitude A (mm)
Applied frequency (Hz)

(b)

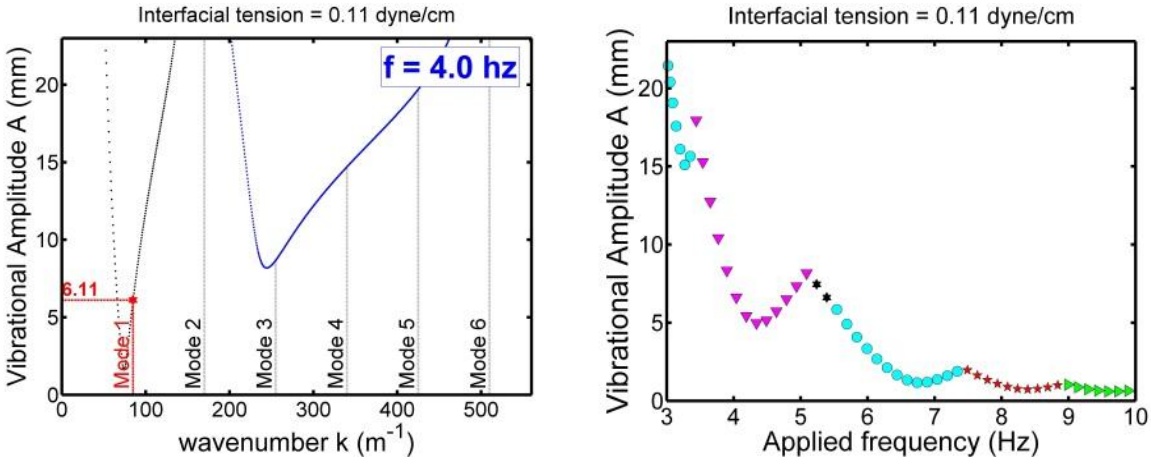
Interfacial tension = 0.11 dyne/cm
f = 4.0 hz
6.11
Mode 1
Mode 2
Mode 3
Mode 4
Mode 5
Mode 6
Vibrational Amplitude A (mm)
wavenumber k (m-1)
Interfacial tension = 0.11 dyne/cm
Vibrational Amplitude A (mm)
Applied frequency (Hz)

(c)

Figure 2.11: Decreasing Interfacial tension from (a) γ = 2.45 dyne/cm, (b) γ = 0.78 dyne/cm and (c) γ = 0.11 dyne/cm (values taken are predicted values with temperature variation). $[\rho_1 = 885\,\frac{\text{kg}}{\text{m}^3}, \rho_2 = 1622\,\frac{\text{kg}}{\text{m}^3}, \mu 1 = 20.00\ \text{cSt and}\ \mu 2 = 12.80\ \text{cSt}]$

2.3.4 Effect of gravity: Simulating Faraday instability in microgravity

Space applications like vibrating propellant in rocket engine have variable acceleration. The gravity effects have been studied historically in ISS (International Space Station) and parabolic flight. Decrease in gravity causes tongues to shift rightwards to higher wavenumbers and forces the widening of tongues. Interestingly, the rate of spreading of the first sub-harmonic tongue was much higher in comparison to higher harmonics. This movement causes smaller wavelength and spreads nodes causing higher probability of sub-harmonic waves as well the decrease in mode width. Thus, a reduced gravity solution will have continuity of modes and will behave much more like an infinite boundary system.

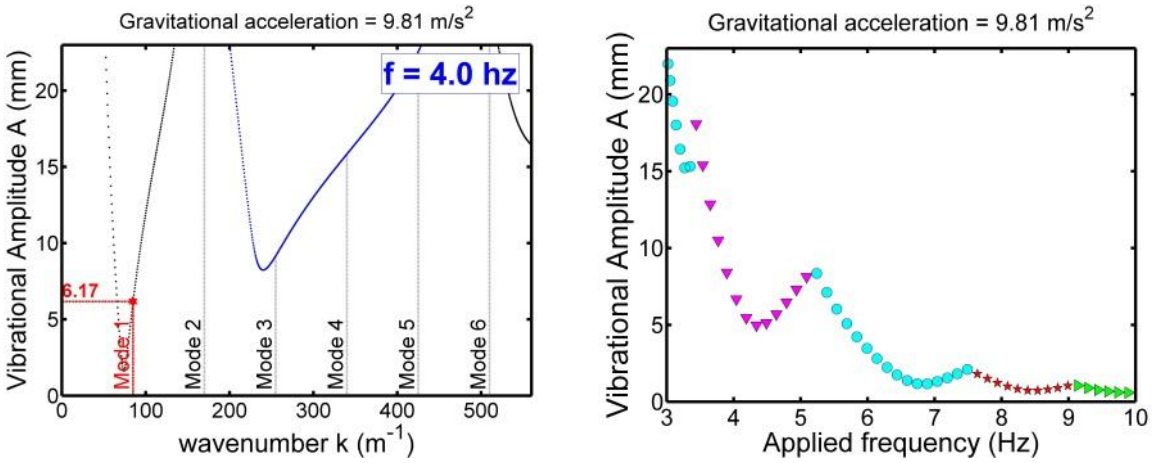

(a)

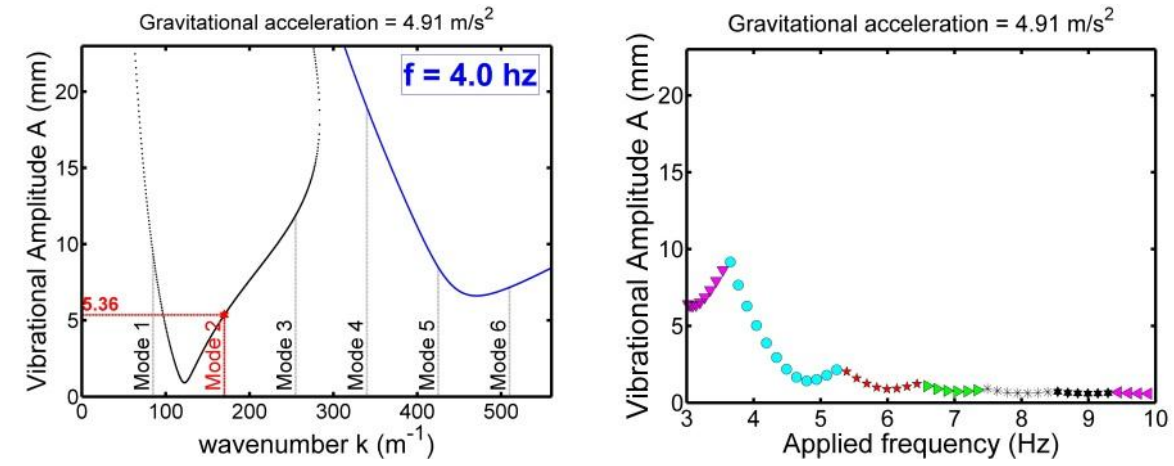

(b)

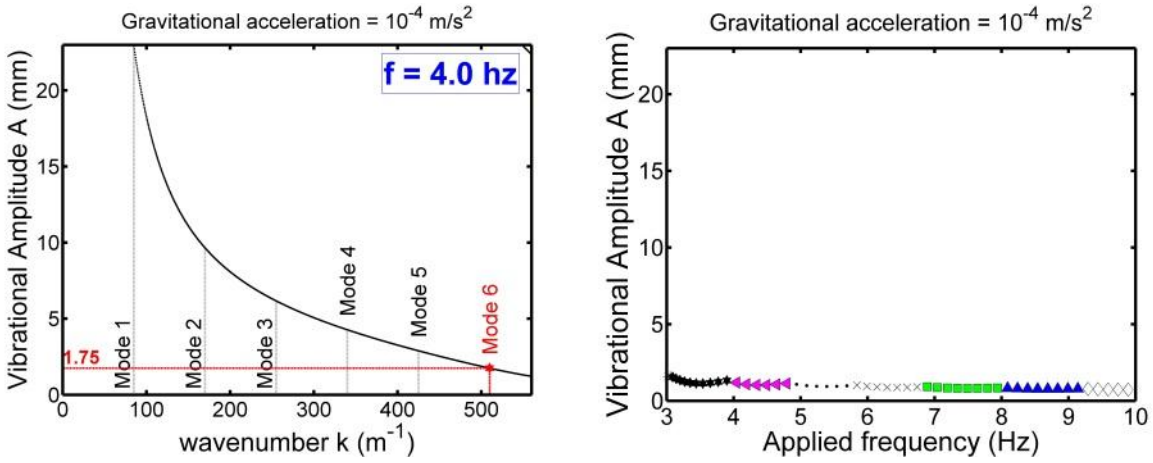

(c)

Figure 2.12: Decreasing gravity from (a) g = 9.81 m/s^2, (b) g = 4.91 m/s^2 and (c) g = 10^{-4} m/s^2.

[$\rho_1 = 885\,\frac{\text{kg}}{\text{m}^3}, \rho_2 = 1622\,\frac{\text{kg}}{\text{m}^3}$, $\gamma = 2.45\,\frac{\text{dyne}}{\text{cm}}$, μ_1 =20.0 cSt and μ_2 = 12.8 cSt]

Chapter 3

Ground based experiments of Faraday instability

The theoretical part was crucial to have an understanding of the instability and parameters affecting instability. The experimental work confirmed prediction of theory qualitatively & quantitatively and the analytical study gave an insight in understanding physics behind the instability. This has been done using an electro mechanical shaker with a pair of binary fluids. Binary fluids pose a very unique property of being soluble in each other depending on the temperature and are completely miscible above consolute temperature. At below and near the consolute temperature, the surface tension between the two fluids tends to zero and so does their density difference. The results had been explored to investigate the effect of vanishing surface tension and the reduction of density difference in the development of the instability. The effect of confinement and the gravity on the development of the instability had also been investigated. The results were then compared to the theory. It has been shown that in experiments the assumption of stress-free sidewalls was not feasible and thus produces variation from established theory specifically in the vicinity of boundaries. Two liquids contacting a solid sidewall inevitably produces a static meniscus, which emits waves during vibration, and violates the assumptions of a flat interface. Also rectangular geometry produces corner stresses which were not taken into account in linear stability analysis. Fluid shearing at the sidewalls and capillary hysteresis are other examples of complex stresses which arise in real systems and must be considered. Experiments and theory of Faraday instability are observed over a range of temperature in which a choice fluid system goes from immiscible to miscible character.

3.1 Description of the experimental set-up

The experimental system considered in this study used a transparent cell containing FC-72 and 1.0 cSt Silicone oil taken at equal proportions by volume. The temperature of these liquids, which determines the coefficient of interfacial tension, was controlled by circulating water around the cell. The actual configuration of the cell has been shown in Figure 3.1. The outer dimensions of the cell were 55 mm (width) × 55 mm (height) × 7 mm (depth). The cell consisted of a polycarbonate frame which was sandwiched between two 55 mm × 55 mm × 1 mm

(thickness) sapphire glasses at the front and the back. The use of sapphire material reduced the resistance for heat transfer between the liquids and the circulating water. A sealed copper capsule with trapped air was placed in contact with the silicone oil in the cell interior. This capsule easily contracted/expanded to compensate for the thermal expansion/contraction of the liquids. The dimensions of the inner region encompassed by the liquids (excluding the volume occupied by the copper capsule) were 35 mm (width) × 29.3 mm (height) × 5 mm (depth). The current cell depth of 5 mm is an optimum value considering the necessity for attaining faster thermal equilibrium of liquids with the circulating water, particularly in the parabolic flight experiments. Though a cell even narrower than 5mm would have suited better both for heating/cooling of liquids and for making the interfacial tension effects dominant, it has been avoided so that the critical amplitude remains within the measurement range of the current linear oscillator. Note that the critical amplitude increases drastically with the increase in wall proximity.

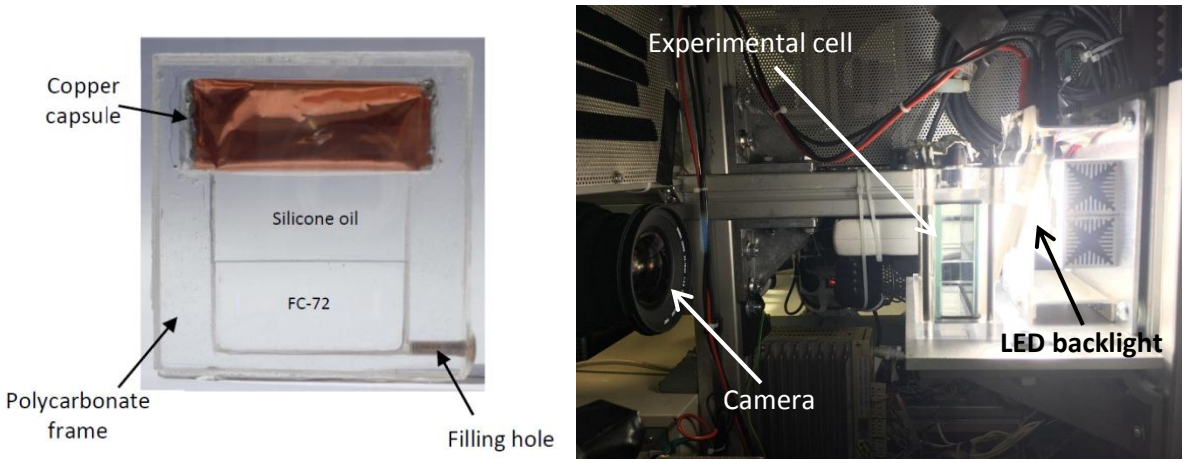

(a) *(b)*

Figure 3.1: (a) Experimental Cell (b) Experimental cell installed in setup

In the present configuration, the binary liquids were filled through the side hole by suitably tilting the cell to completely evacuate the air. Once the cell was fully filled with liquids, the hole was sealed using a threaded screw wrapped with PTFE (Poly tetra fluoroethylene).

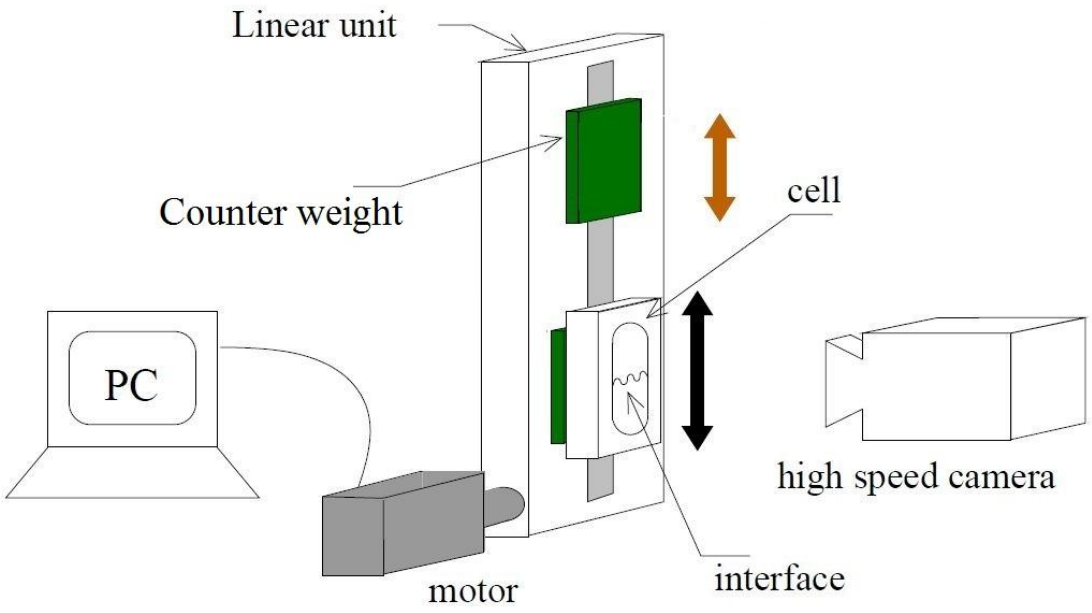

(a)

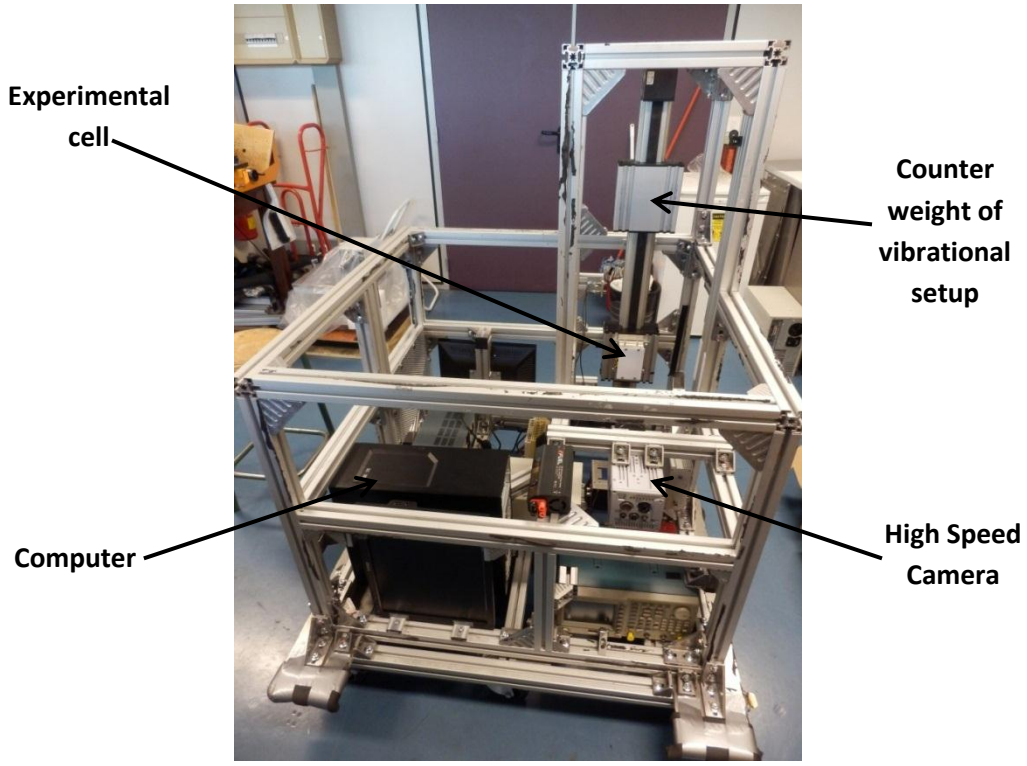

(b)

Figure 3.2: (a) Sketch of the experimental setup in which electro mechanical shaker used to initiate the vibration of Fluid (b) Pictures of experimental setup

The circulating water for the control of the liquids' temperature was actuated by a pump. The desired temperature in the circuit (with a stability of ± 0.010 °C) was achieved using a PID (proportional–integral–derivative) controlled immersion heater. The heater controller received temperature feedback from a Pt-100 probe suitably located in the circuit. Aside of the heating, the water circuit was also equipped with a feedback controlled Peltier element for cooling the liquids when required.

The cell along with the enclosure for the circulating water was mounted on a vertically oscillating platform (the total weight of the cell with enclosures and back lighting is around 3kg) which was actuated by a linear drive with servo control of speed (see Figure 3.2 (a)). The motion of the drive was computer controlled and allowed a maximum acceleration of approximately 3g with frequencies up to 15 Hz. The amplitudes (A) and frequencies (f) were observed to be within 2% and 0.1% of their respective set values.

The onset of the instability was recorded using a high speed camera (Photron SA3 60K M2). The illumination for the imaging process was obtained through a LED light placed behind the cell, on the moving platform. Generally, the motion of the interface was captured at 250 images per second with an exposure time of 5 μs. The recorded images were digitized and calibrated into length scales from which the size of the instability (wavelengths) was measured. The error in wavelength measurements was estimated to be about ±5% based on the processed images. In order to maintain the saturation of fluids with respect to solubility, they were shaken vigorously (A = 30 mm and f =3 Hz) for 30 s followed by a wait time of 30 s before each experimental trial. This was necessary to obtain repeatable results from the experiments. The detailed experimental equipment explanation can be seen in Appendix A.

3.2 Choice of Liquids

For analysing two fluids Faraday instability, a liquid set was necessary which (i) forms an interface that glides across the container wall, representing a minimization of the associated capillary sidewall stresses or any disturbance generated by wall effects and (ii) produces an

interface with a minimum meniscus in order to achieve a near flat interface and reaches nearest possible assumptions of theory. Another important and primary goal was to have a binary fluid of accessible consolute temperature (well below the boiling temperature of fluids) and also not toxic in case of leak in parabolic flight campaign and for future experimental use in ISS (International Space Station). The meniscus waves produced by sidewalls lead to parasitic surface ripples which disturb the parametric waves generated from the vibration force. A binary fluid system consisting of Perfluorohexane (FC-72), a dense and inert fluorinated hydrocarbon, and Octamethyltrisiloxane (1.0 centistoke silicone oil), produces an interface with very small negligible meniscus. The slight pinning was verified by angling the experimental cell in an even position in which case a rapid (less than 1sec) reappearance of the interface to a flat position could be observed, which signified low sidewall stresses. Low surface tension (0.77 mN/m at T = 25 ^{0}C corresponding to experimental value) was useful in reducing the capillary sidewall stresses. Low surface tension also leads to minimum meniscus and an almost not pinned triple contact line at wall. Silicone oil also forms a tiny film on sidewall around FC-72, making the interface floating almost stress free on side walls. The fluid consolute temperature was ~ 42.5 ^{o}C which is well below the boiling temperature of more volatile (FC-72) component of fluid system (for which boiling temperature is 56 ^{o}C).

The analyses of miscible fluid systems were difficult with experimental challenges; an exact repeatability carries a demanding task in experimentations. In order to have the same initial conditions prior to experimental runs, an experimental protocol consisting of vigorously shaking the cell was set. This ensured the suppression of any eventual stratification of the two liquid layers (whose degree of miscibility increases with temperature) near the interface. Ideally, a binary fluid system should have a step transition of mixing with consolute temperature to make initial conditions less important and increase importance of interfacial thickness and tension. The steady existence of molecular diffusion and mixing with the rise of even slightest amount of temperature makes the meaning of exact initial conditions for experiments indefensible. The fluids considered in the present experiments have an important characteristic of being miscible above a certain temperature (consolute temperature) and partially immiscible below it. Thus, when the fluids temperatures were lowered, they become partially immiscible and separable

into two distinct entities. The temperature can be subsequently increased to make them completely miscible, giving exact similar conditions before start of each experiment which could be used to analyse the influence of parametric oscillations on the evolution of instabilities. As well as, a single charge of fluids can be repeatedly utilized for all the planned experimentations. Also, by controlling the temperature of the fluids, it was possible to alter the mass diffusion coefficient of the fluids, which was the most important property that governs the fluids mixing process. In literature it was shown that the sidewall stresses (viscous and capillary) can control the overall system dissipation, even when the capillary effects were lessened by addition of surfactant, as in the experiments of Henderson & Miles (1990). FC72, a dense and inert fluorinated hydrocarbon, and 1.0 centistoke silicone oil produce an interface with very small negligible meniscus. Angling of the experimental cell resulted in uneven and rapid reappearance of the interface to a flat position, signifying low capillary sidewall stresses.

3.3 Experimental repeatability

The chosen binary fluids have a unique property of a continuous process of mass transfer. The rate of mass transfer was dependent on the system temperature, thus making the fluids' densities, viscosities and surface tension changing with temperature. For the current fluid system, densities and viscosities were measured with temperature and shown in Fig 3.3(a) and 3.3(b) respectively. The measurement of both densities (top and bottom fluid systems) clearly shows the mass transfer of fluids (the density of the top fluid phase was increasing even if temperature increases showing the partial miscibility of the two fluids). A complete mixing arises at consolute temperature (42.7 ^{o}C). For the repeatability of experiments it was necessary that fluids be in an equilibrium condition with respect to the imposed temperature of the system before the initiation of vibration. However, it was difficult to attain the perfect initial condition for each experiment for a miscible fluid system such as the one used in the present experiment. The process of getting the same initial conditions makes the analysis of partial miscible fluids systems at any temperature difficult and long. The steady existence of molecular diffusion and binary fluid mixing with the rise of even a slightest amount of temperature makes

the meaning of exact initial conditions for experiments indefensible. For this purpose, a process of rigorous equilibrium mixing (shaking the fluid system at given amplitude and frequency) followed by fixed waiting time has been achieved before each experiment. Densities and viscosities of fluids have been measured in these equilibrium conditions. Initial condition was used to vibrate the cell rigorously at amplitude of 25mm with frequency of 3 Hz for a period of 30 seconds (to cause complete mixing of fluid by vibrating well above critical threshold of system). It was done so that the two liquids could be in equilibrium state with the desired temperature of experiment and allow the interface to stabilize for 30 seconds before it starts perturbing the interface in the experiment. Timer was included in the program to avoid any possibility of manual errors. For the miscible case similar condition was needed. Thus, Initial condition was set up at 41 ^{o}C for miscible experiment followed by raising the temperature up to 43.82 ^{o}C (to achieve conditions of parabolic flights for miscible experiment) and wait time of 2 minutes and 20 minutes for two different sets of data. Waiting time permits to control the interfacial thickness and density gradient due to diffusion, before starting the experiment. Experiments were performed to measure density and viscosity values of the binary fluids used in the system. For this reason, fluids were mixed in ratio of 1:1 by volume and put into temperature bath for measurement of density and viscosity values as shown in Figure 3.3.

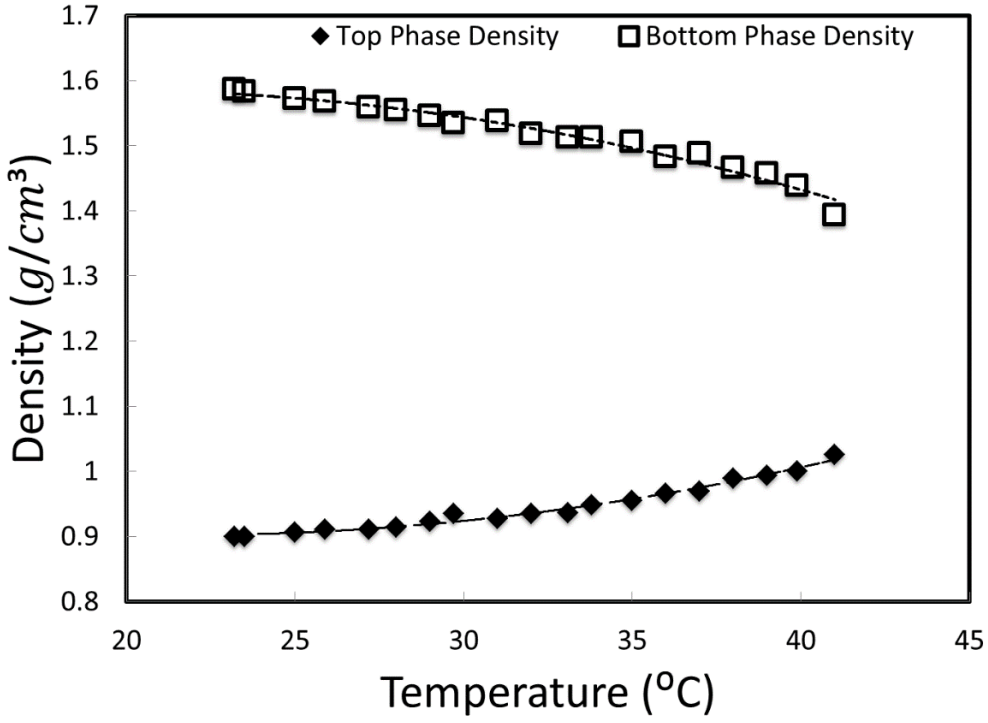
Top Phase Density
Bottom Phase Density
Density (g/cm^3)
1.7
1.6
1.5
1.4
1.3
1.2
1.1
1
0.9
0.8
20
25
30
35
40
45
Temperature (°C)

(a)

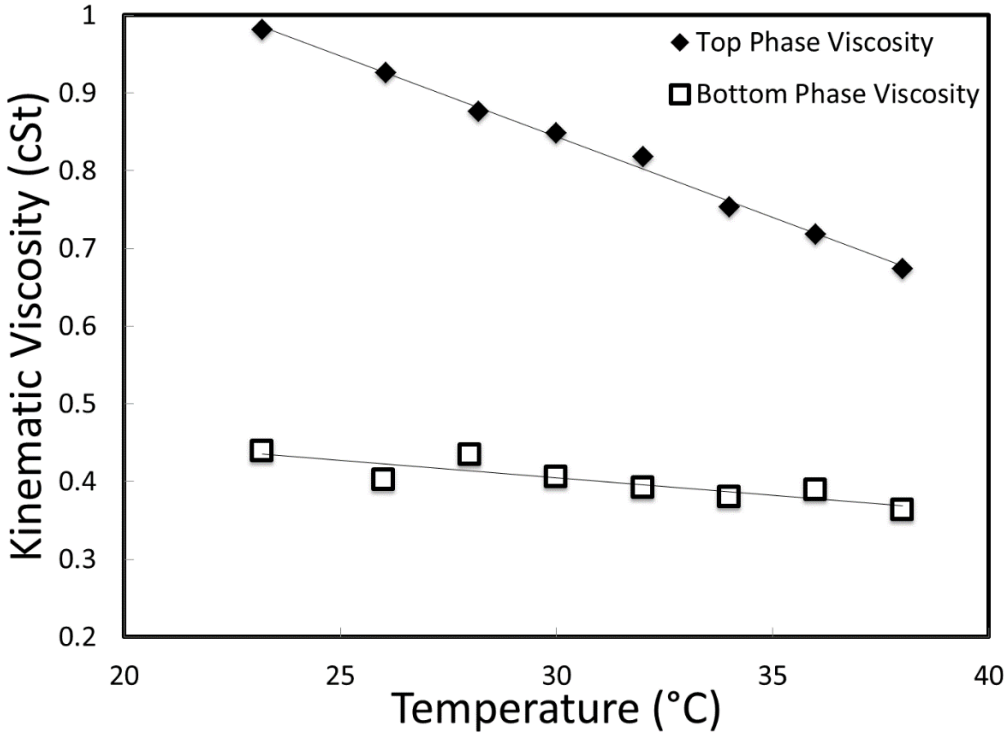
Top Phase Viscosity
Bottom Phase Viscosity
Kinematic Viscosity (cSt)
1
0.9
0.8
0.7
0.6
0.5
0.4
0.3
0.2
20
25
30
35
40
Temperature (°C)

(b)

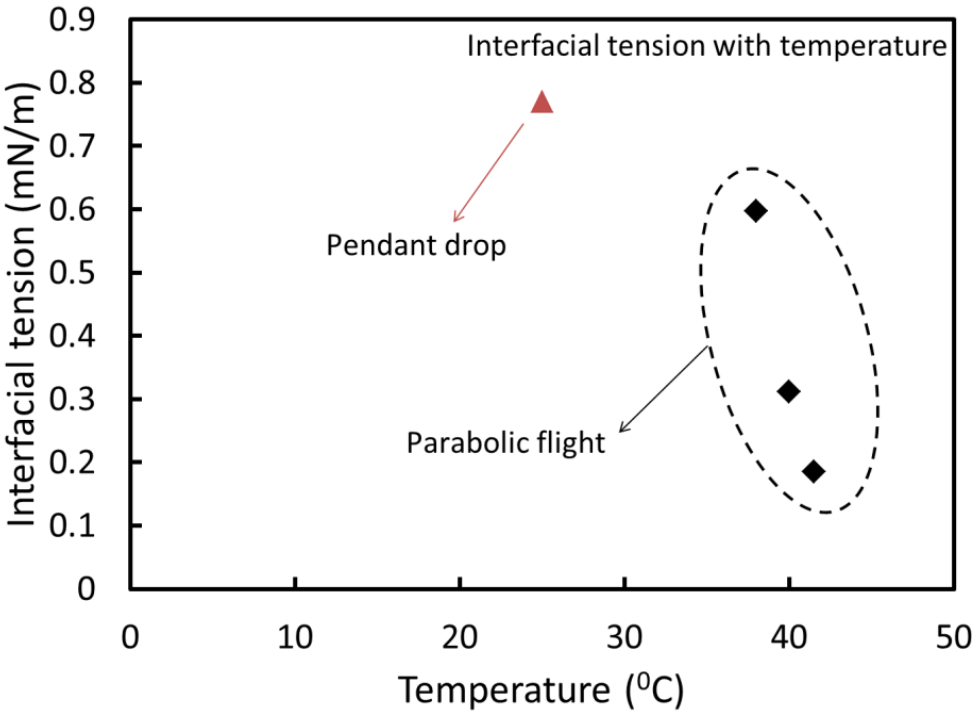

Figure 3.3: Experimental measurement of (a) density values (b) viscosity values (c) Interfacial tension with temperature (top and bottom phase fluid were in equilibrium)

Another important aspect in maintaining initial condition was to observe wetting behaviour of the FC72-silicone oil film and the stick-slip behaviour of the contact line. Silicone oil creates a film on the sidewalls that helps in maintaining the low sidewall stress and results into a lower instability threshold in comparison to the conditions when film was not present. It was important that wetting condition was similar for all experiments to offer constant stress from sidewalls for the phenomena. This was achieved with a constant waiting period after a rigorous shake of fluids.

3.4 Results and Discussion

For a particular fluid state and oscillation frequency, the essential task involves identifying the lowest excitation amplitude for which a discernible interfacial wave occurs. While it is conventional to expect a continuum of sub-harmonic modes in a laterally infinite system, the

present confined system is characterized with both harmonic and sub-harmonic modes occurring over discrete bands of frequencies, as finite system only allows certain wave number to appear which is defined by cell dimensions. For a rectangular cell allowed wavenumbers can be defined as (Bejamin and Ursell, 1954),

$$k = \sqrt{\frac{\pi^2 m^2}{W^2} + \frac{\pi^2 n^2}{L^2}} \tag{3.1}$$

Where *m* and *n* are integers and *'W'* and 'L' are dimensions of rectangular cell in the plane of interface. The gap between allowed wave number gives birth to discretized solution of the problem. Within each discrete band, the critical amplitude attains minima at the natural frequency of the mode. Such a behaviour occurs on the account of a trade-off between the variation of inertial forces and the viscous dissipation, both of which increase when the imposed frequency increases. The former is destabilizing while the latter is stabilizing. The variation of inertial forces is feeble at lower frequencies and it requires a large acceleration for the instability to originate. At higher frequencies, the viscous dissipation however becomes predominant and a large imposed acceleration is once again required to attain criticality. Their cumulative effect ultimately leads to minima of the critical acceleration/amplitude at the natural frequency.

Similar to the observation of Batson *et al.* (2013), the high wetting nature of silicone oil allows the liquid interface to smoothly slide over the side walls. As current cell in question has dimension 35mm in long side of plane of interface and 5mm in short side of plane of interface, short side dimension is negligible enough compare to longer side for early mode appearance. Hence, we can safely assume that the flow features are primarily two dimensional except for the occurrence of a small meniscus which gives rise to persistent harmonic excitation of the interface even before the occurrence of the actual Faraday modes for the observed frequency (as shown in figure 3.5, there is no mode observed in the width direction of the cell)The meniscus waves do not have any detrimental effect on the prediction of thresholds for the sub-harmonic modes for whom the bifurcation is sub-critical. The non-linear growth pattern of these detuned modes results in a perpetual growth of interfacial perturbation until the

discernible interface wave ruptures into some irregular pattern. Hence for any amplitude larger than the threshold, the instability manifests itself in a matter of time and makes the prediction of the critical threshold convenient. However the time for the instability to become noticeable is inversely relative to the closeness of the applied amplitude to the threshold. Contrastingly for a harmonic mode, the bifurcation is supercritical and the amplitude of the interfacial wave saturates at a value proportional to the excessiveness of the imposed excitation to the threshold. This complicates the prediction of criticality in harmonic cases closer to the threshold; where the meniscus wave might have amplitude larger than the actual Faraday wave near to critical threshold. Hence, observing the convergence of the Faraday wave at threshold becomes difficult and it introduces a bit of uncertainty in the predicted criticality for the harmonic modes.

3.4.1 Immiscible Instability threshold

Experiments were performed for immiscible instability threshold below consolute temperature for temperature range 25 ^{o}C – 42 ^{o}C as explained above and are shown in Figure 3.4. The mismatch observed in experimental threshold to theoretical threshold cannot be explained with the theoretical approach presented in this thesis (see Chapter 2). Imposed oscillation frequency and the lowest possible excitation amplitude for which a distinct visible interfacial wave occurred was measured and recorded. These experiments had shown the shifting of modes towards lower frequency as predicted qualitatively by the theory (Benjamin and Ursell, 1954). Figure 3.4 shows the critical threshold amplitude, A, (on y axis) obtained for frequencies ranging between 3 and 8 Hz (on x axis) at five different temperatures, viz., 25 ^{0}C, 38 ^{0}C, 40 ^{0}C, 41.5 ^{0}C, and 42 ^{0}C. In this temperature range, the interfacial tension coefficient and density contrast drastically diminished as the temperature of the fluids approached the consolute value (42.5 ^{0}C). The current confined system at low frequencies was characterized by both harmonic and sub-harmonic modes occurring over discrete bands of frequencies. This was in contrast to a continuum of sub-harmonic modes that were observed in large aspect systems. The various modes have been labelled as A, B, C, etc., and shown in Fig. 3.5. Here, mode B alone was

harmonic and it consists of two and half waves. The rest of the modes were sub-harmonic and feature as multiples of the half wave, i.e., A consisted of half wave, C consisted of a full wave, D consisted of one and half waves and so-forth. The different modes interconnect at co-dimension points where the pattern consists of a superposition of both modes, dynamically changing from one state to the other. Within each of the discrete bands, the critical amplitude attained a minimum at the natural frequency of the mode. This phenomenon is equivalent to that of a simple pendulum whose fulcrum is subject to enforced pulsations. The response amplitude of the pendulum bob reaches a peak value when the forcing amplitude of the support crosses a threshold. This critical amplitude primarily depends on the forcing frequency and attains a minimum when the parametric frequency equals the system's natural frequency. For the present case of Faraday instability, a similar effect produces a minimum of criticality at the natural frequency of each mode and that frequency is called tuned frequency for that mode. Generally, any perturbation of the fluid interface will produce ingress of heavier fluid into the lighter fluid along the crests and the case vice-versa along the troughs. The inertial forces acting on these masses induced by the imposed acceleration provoked the onset of instability and effects such as gravity, interfacial tension and the viscous diffusion acted as restoration forces that bring back the interface to its initial flat condition.

In the case of the present experiments where the increase in temperature led to the decrease in both the density difference (note that the density of each layer changes on account of the solubility and depends on temperature, see figure 3.3a) and the interfacial tension, the earlier discussion in section 2.3, aids in understanding the fluid behaviour. The impact of changing fluid temperature on the onset characteristics has been depicted in Figure 3.4. An important feature that can be observed here is that the frequency band for each mode shrunk with an increase in the fluid temperature. This shrinkage was due to a drift of modes toward lower frequencies of excitation. In other words, the natural frequency of each mode became smaller. This did not come to a surprise as reduction in both the density difference and interfacial tension ought to lead to reduction in the natural frequency of each mode.

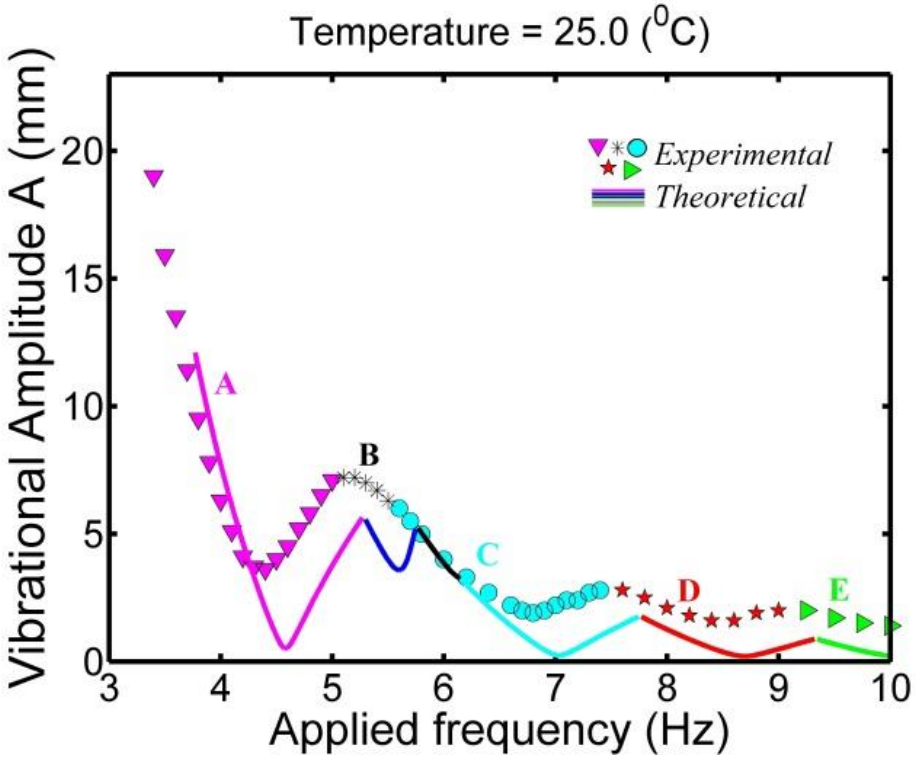
Temperature = 25.0 (^{0}C)
Vibrational Amplitude A (mm)
Applied frequency (Hz)
Experimental
Theoretical
A
B
C
D
E

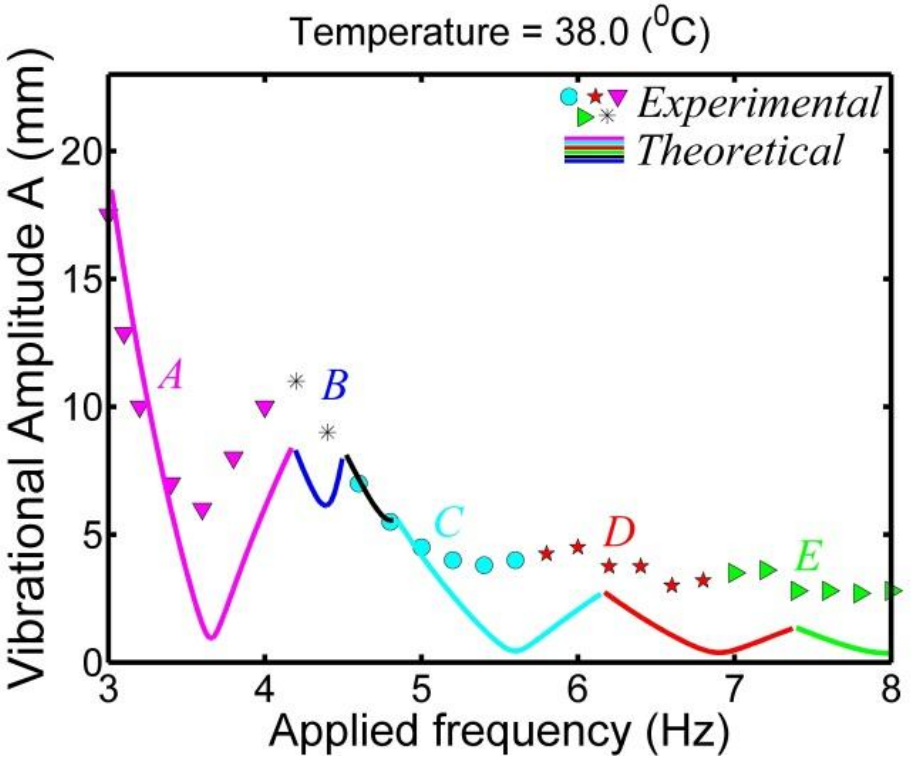
Temperature = 38.0 (^{0}C)
Vibrational Amplitude A (mm)
Applied frequency (Hz)
Experimental
Theoretical
A
B
C
D
E

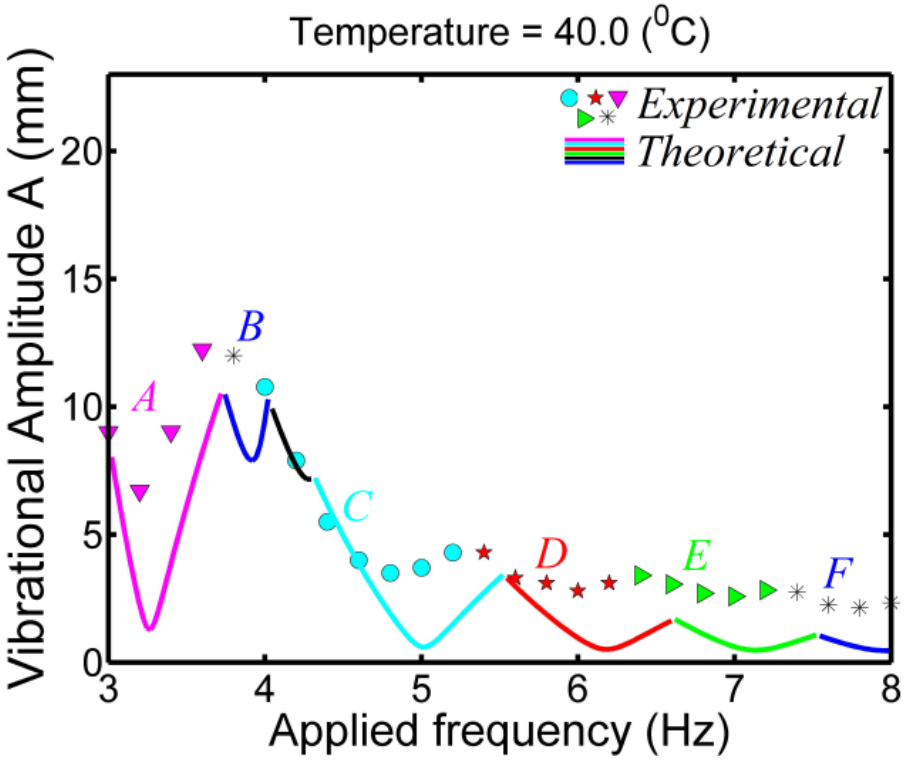
Temperature = 40.0 (^{0}C)
Vibrational Amplitude A (mm)
Applied frequency (Hz)
Experimental
Theoretical
A
B
C
D
E
F
0
5
10
15
20
3
4
5
6
7
8

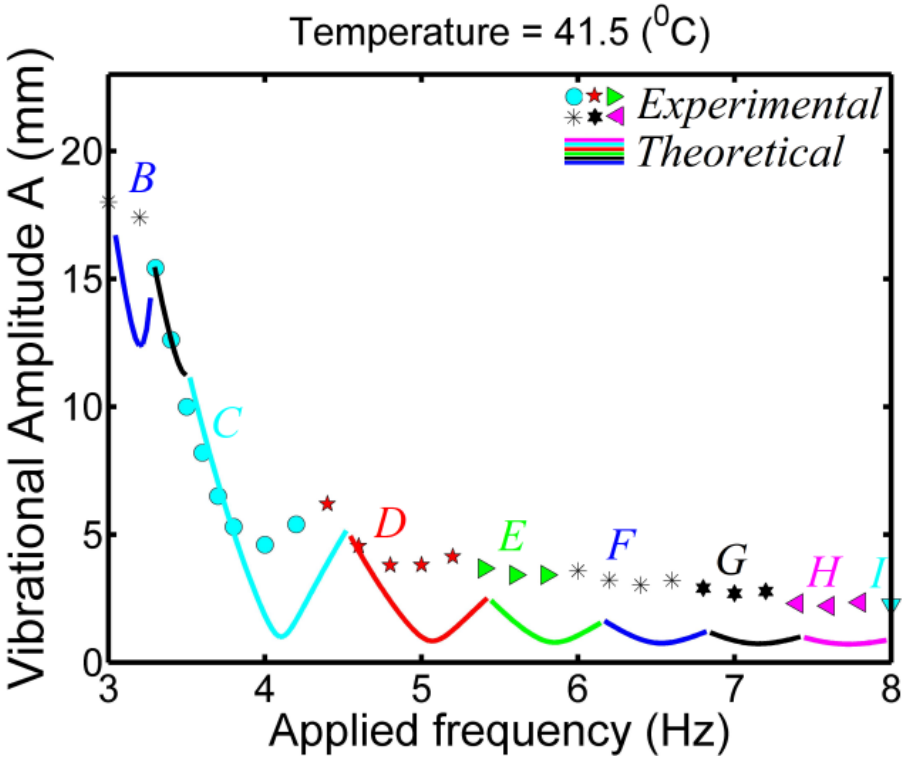
Temperature = 41.5 (^{0}C)
Vibrational Amplitude A (mm)
Applied frequency (Hz)
Experimental
Theoretical
B
C
D
E
F
G
H
I
0
5
10
15
20
3
4
5
6
7
8

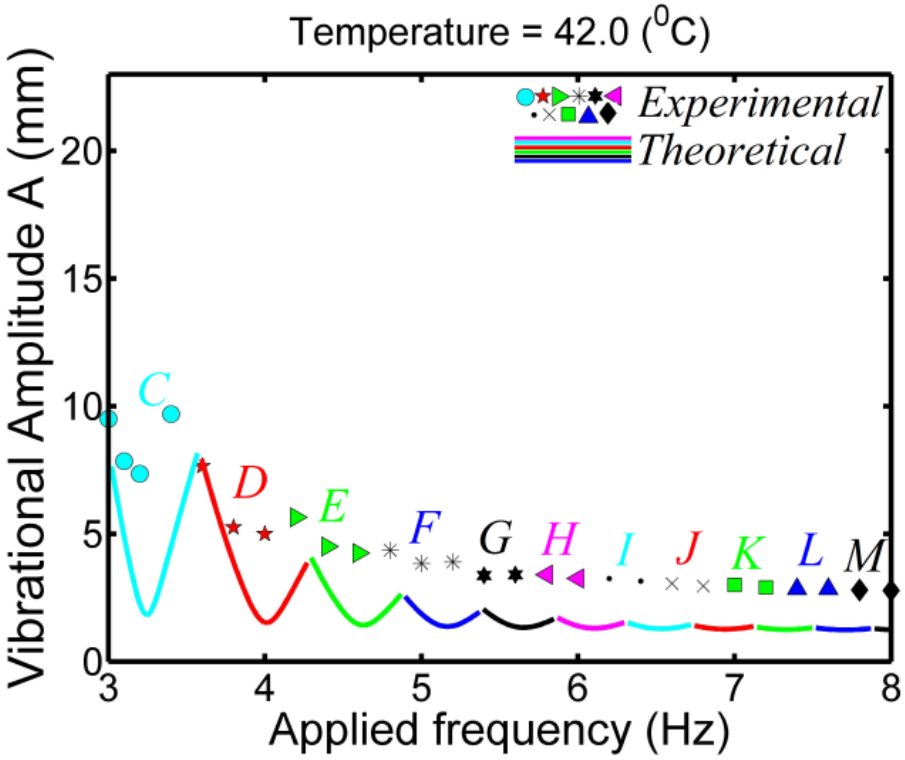

Figure 3.4: Immiscible threshold experiments compared with analytical solution (see Chapter 2).

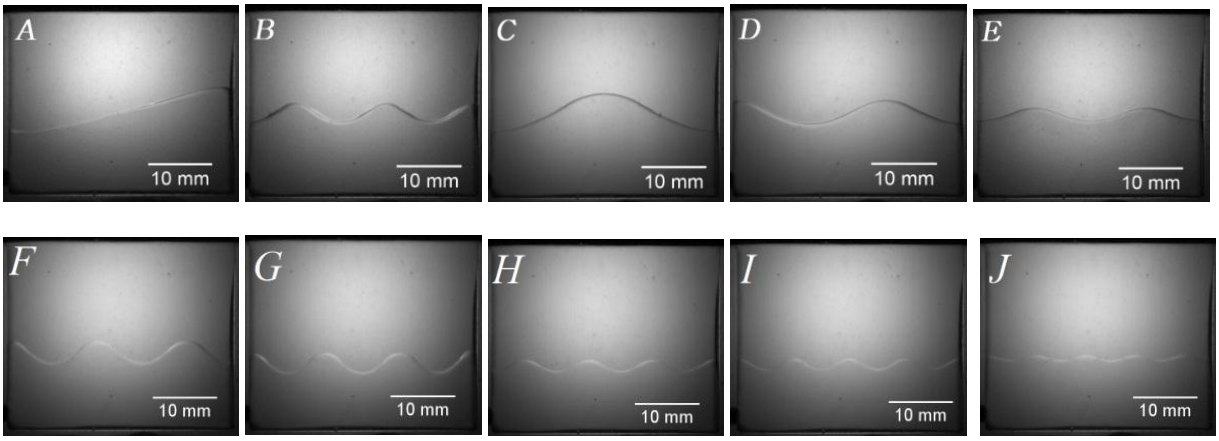

Figure 3.5: Observed Experimental modes

Larger wavelengths corresponded to density difference dominance and smaller wavelengths corresponded to interfacial tension and viscosity dominance. Considering the present confined system where the critical wavenumbers at onset for lower frequencies were small (see Figure 3.4), any change in the interfacial tension could not have a notable impact on the instability

pattern. Therefore, the only significant contribution for the natural frequency came from the gravitational term, $(\rho_1 - \rho_2)kg$. It may be recalled that for resonant interfacial oscillations, there ought to be a match between the imposed frequency and the natural frequency of the system. Hence, for a given imposed frequency in the low frequency range, the gravitational term has to be maintained constant irrespective of the temperature of the fluids. This implies that any change in the density difference should come attended with an increase in the critical wavenumber and this is what is observed in the experiments. Only at high frequencies where the response wavenumbers are higher, the reduction in interfacial tension influences the instability.

The decrease in the interfacial tension is expected to be significant near the consolute temperature and the response wavenumber must become very large to maintain the system's natural frequency. The mode discretization therefore becomes difficult to discern and one can even expect a continuous change of wavelength with the frequency, for which the evidence starts to appear at 42 ^{0}C (see figure 3.4). As far as the critical threshold is concerned, it is difficult to give its exact trend of variation at lower frequencies as the drifting of modes can correspondingly make a frequency either more stable or more unstable with respect to the temperature. One may see this effect for the frequency of 4.4 Hz at different temperatures in Fig. 3.4. However, a clearer pattern was apparent at higher frequencies where the curves moved towards a constant value of critical amplitude, independent of the frequency/mode. Interestingly, this amplitude has shown an increase with the increase of temperature. In other words, the system actually became more stable with the reduction of interfacial tension (critical amplitudes decreases in Fig. 3.4). This behaviour might appear counter-intuitive as one would normally expect less stability in such situations. However, the selection of higher wavenumber that leads to larger viscous dissipation must play a stabilizing role. In other words, the instability brought in through the reduction of interfacial tension effects was overwhelmed by the viscous stabilization, particularly when the operating conditions were closer to the consolute point. Another notable outcome of temperature change in the vicinity of the consolute value was the reduction in meniscus thickness which minimized the damping effects brought in by the meniscus waves.

In summary, we can clearly see from the ground experiments that the entire modes shift towards a lower frequency as the fluids' temperature is increased. In fact, this mode shift is what that might be expected upon inspection of the natural frequency given in equation 2.35. However, both the density difference as well as the interfacial tension decreased with an increase in temperature and it was impossible to experimentally isolate the change happening due to one effect from the other. It was evident from the theory that the density difference plays a dominant role at low frequency and interfacial tension at high frequency.

3.4.2 Correction with viscous damping

To understand the physics behind these mismatches, sidewall stresses, contact angles, meniscus wave's effects were studied. In previous theoretical approaches such as Benjamin and Ursell (1954) & Kumar and Tuckerman (1994) & Batson *et al.* (2013), meniscus waves and sidewall effects were neglected, which is in fact true for large size cylindrical cells. However the same cannot be said for small rectangular cell where damping coming from the sidewalls and internal damping within fluids motions affects the threshold.

A simple way to measure damping viscous effects is to measure the rate at which an excited mode decays once excitation force has been stopped. Thus the damping rate is measured over full grown wave decay over time under its own resistance to fluids. Viscous forces in liquids will force the instability to die out with time in the present case with the following equation,

$$a(t) = a(0)\, e^{\eta_{visc}^{exp}\, t} \tag{3.2}$$

Where $a(t)$ is the wave amplitude and $a(0)$ is its initial value; η_{visc}^{exp} is the experimental damping rate in the system. The exponential rate of decay is determined by the slope of the logarithm of the ratio of the wave amplitude ($a(t)$) scaled to the initial value ($a(0)$) and plotted against time for each frequency (see Figure 3.6). The experimental rate of damping can be plotted against frequency with corresponding modes appearing for that frequency as shown in Figure 3.7. Henderson & Miles (1990) made the first attempt at matching single-mode

experiments to a theory incorporating viscous effects. They performed experiments in large cylindrical cell with water as the operating fluid, using a surfactant to minimize the pinning of the interface to the sidewalls. The linear damping coefficient due to viscous effects in the bulk phases, given by Kumar & Tuckerman (1994) and derived by Landau & Lifshitz (1987), ignoring interfacial effects, is given by,

$$\eta_{visc}^{theo} = 2k^2 \frac{\mu_1 \coth kh_1 + \mu_2 \coth kh_2}{\rho_1 \coth kh_1 + \rho_2 \coth kh_2} \tag{3.3}$$

Where η_{visc}^{theo} is the theoretical viscous damping rate used by Kumar & Tuckerman (1994) for the wavenumber k in the system of the two fluids with densities ρ_1, ρ_2 , viscosities μ_1, μ_2 and heights h_1, h_2 for fluids 1 and 2, respectively.

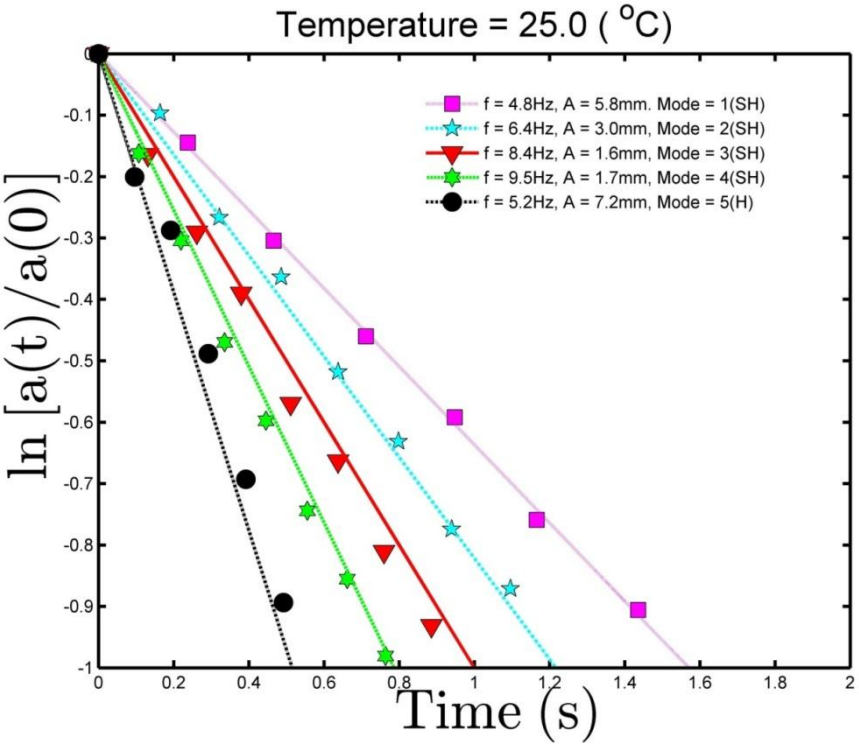

Figure 3.6*:* Measurements of linear damping rate at 25 °C with various modes, "*SH*" means subharmonic mode and "*H*" the harmonic mode.

The theoretical curves in Figs. 3.7 were obtained by measuring the wave numbers corresponding to the applied frequency. The damping rate was found to be constant for a particular mode over a range of frequencies in the observed range. In rectangular geometry, the measured linear damping rate was found to be higher compared to the theoretical one. This difference corresponded to the higher viscous damping rate which was incorporated in the theoretical model as an effective viscosity. The effective viscosity was defined as the value of viscosity which offers the same amount of resistance to the fluid motion in the theoretical model. The effective viscosities were measured from Figs. 3.7 and Eq. 3.3 by considering a mode in a band of frequencies for which the damping amplitude rate was constant to get the effective viscosities μ_1 and μ_2 , knowing h_1, h_2, ρ_1 and ρ_2.

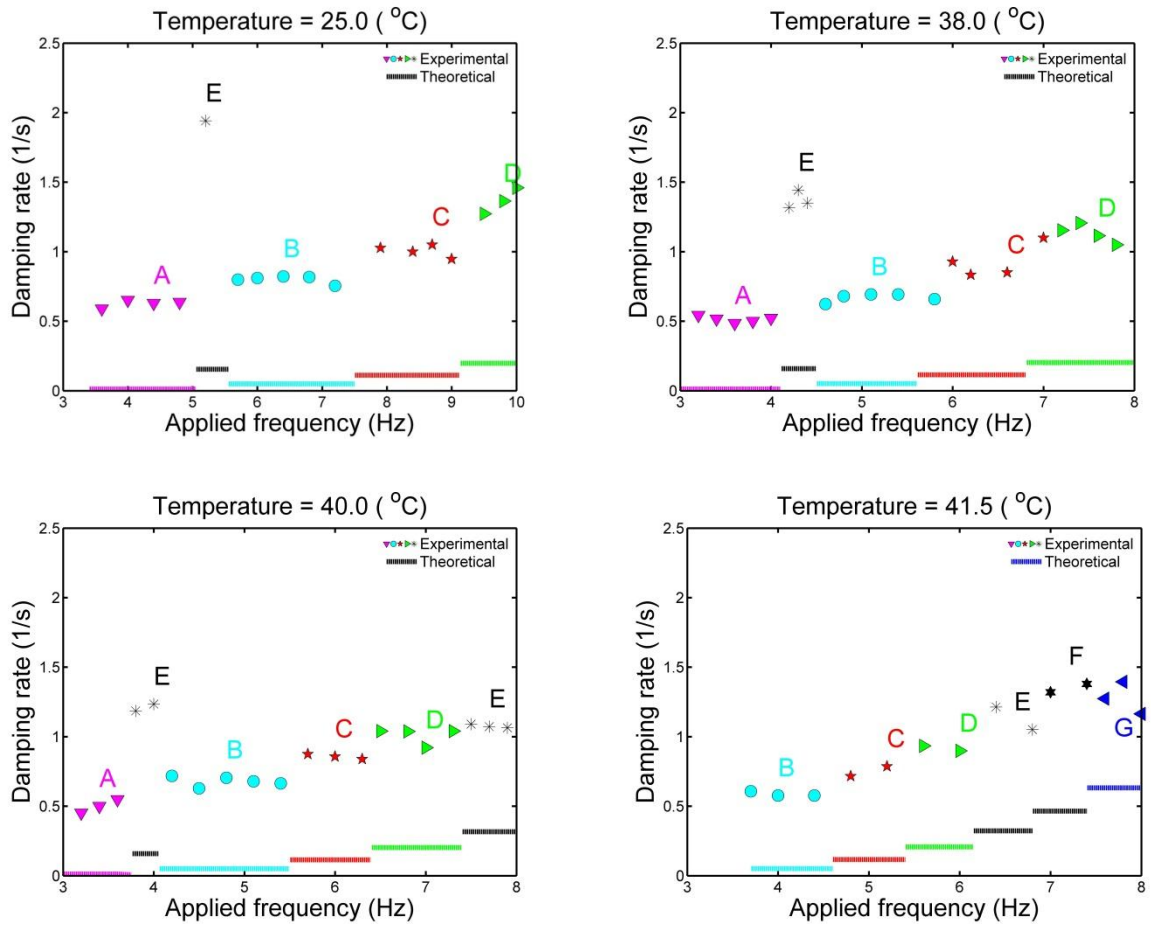

Figure 3.7: Measurements of linear damping by measuring slope of viscous linear damping rate as a function of frequency. Plots are given for critical amplitude.

Viscous damping does not only come from sidewalls and internal dissipation but also from bottom and top walls, where the wavelength of the standing wave is comparable to the container dimensions. The increase in effective viscosity drastically increases sub-harmonic threshold in comparison to harmonic threshold. Harmonic waves have frequency in synchronization to cell motion in contrast to subharmonic waves. Subharmonic mode influences the fluid flow on a larger extension than a harmonic one. Therefore, the effect of friction on the top and bottom walls is necessarily larger for subharmonic modes than for harmonic modes. Thus harmonic waves face much lower effects of fluid heights in comparison to subharmonic waves. However, introducing an equivalent viscosity to compensate for the lack of friction on the side walls will artificially exaggerate the friction on the top and bottom walls.

In the theoretical approach as explained in previous section, the contact angle between the interface and the side walls is assumed to be 90^{o} (on the wall surface). The present fluid system has been chosen with great care such that they provide a flat interface. However in these experiments it has been observed that the fluids make a small contact angle with walls, giving thus a larger sensation of the length for the fluid in the cell and corresponds to around 1-2mm / 3-5 % to the actual length of the cell. For a larger cell this deviation can be ignored but for the cell size as used in current experiments (L=35 mm), this deviation can cause noteworthy difference from theoretical calculations. This effect has been taken into account in the present calculations of the theoretical curves.

It shows that the viscous dissipation of the system for a finite size cell is dominated by walls and interfacial dissipative effects. Kumar & Tuckerman (1994) pointed out in their analysis of a single fluid layer open to air that if the wavelength of a standing wave becomes comparable to the filling depth, the dissipation from the bottom boundary layer becomes dominant and results in harmonic waves.

Experiments for the present cell were run at various temperatures and for complete range of frequencies in order to measure the decay of wave amplitude, once the excitation forces were stopped. The results helped us to understand the relationship between theoretical and

experimental measured values of damping. As the mode number increased, theoretical and experimental viscous damping rate difference decreased. This was due to the fact that the wavelength considerably decreased and became negligible with respect to the cell size moving thus to an infinite size system. This observation was in line to the observation made by Hill (2002) who stated that as domain size became large enough the viscous damping diminishes.

Experimental results have been compared with modified analytical solutions at complete temperature range (25 ^{o}C, 38 ^{o}C, 40 ^{o}C, 41.5 ^{o}C, 42 ^{o}C) in Fig.3.8. Figure 3.8 shows clearly a better match between theory and experiment and validates the measured viscous damping rates which quantitatively influence greatly the input of effective viscosity in the linear model.

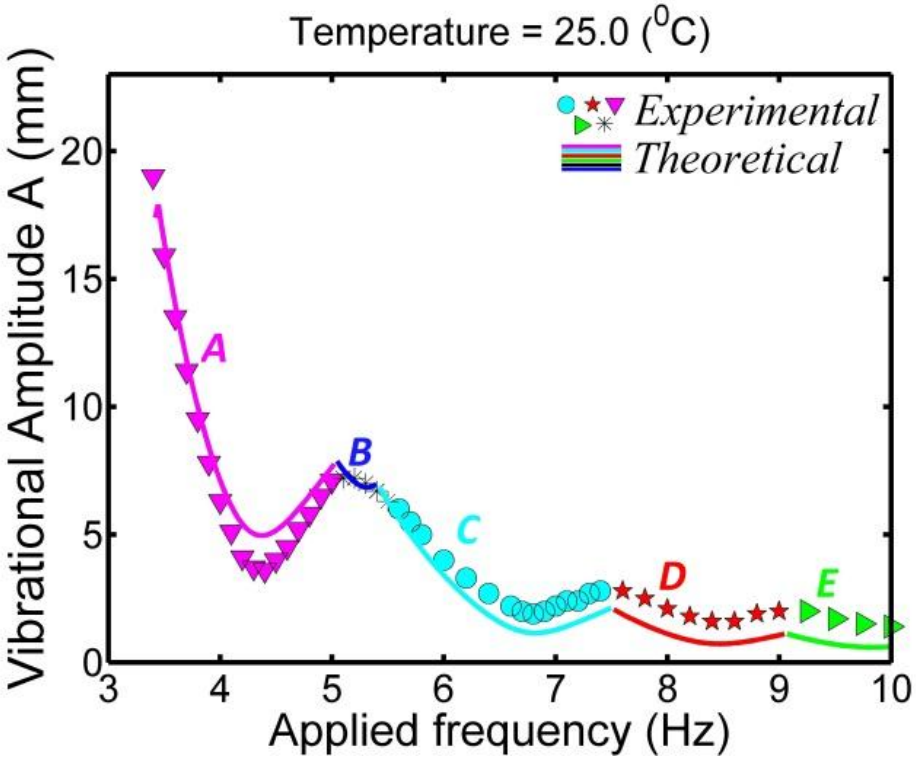

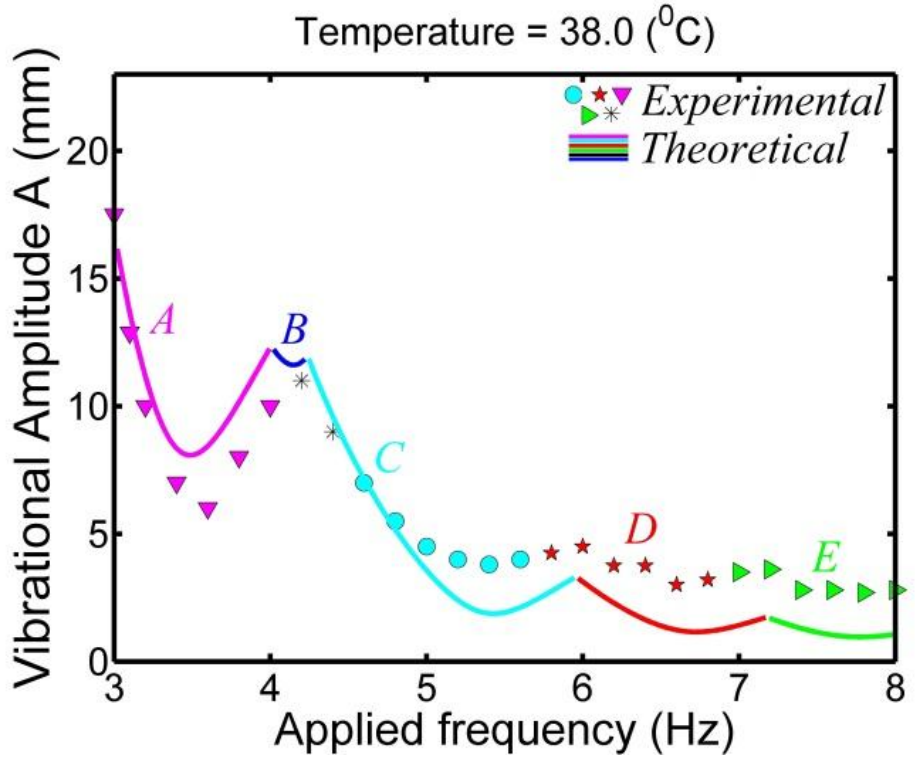
Temperature = 38.0 (^{0}C)
Experimental
Theoretical
Vibrational Amplitude A (mm)
Applied frequency (Hz)
A
B
C
D
E
0
5
10
15
20
3
4
5
6
7
8

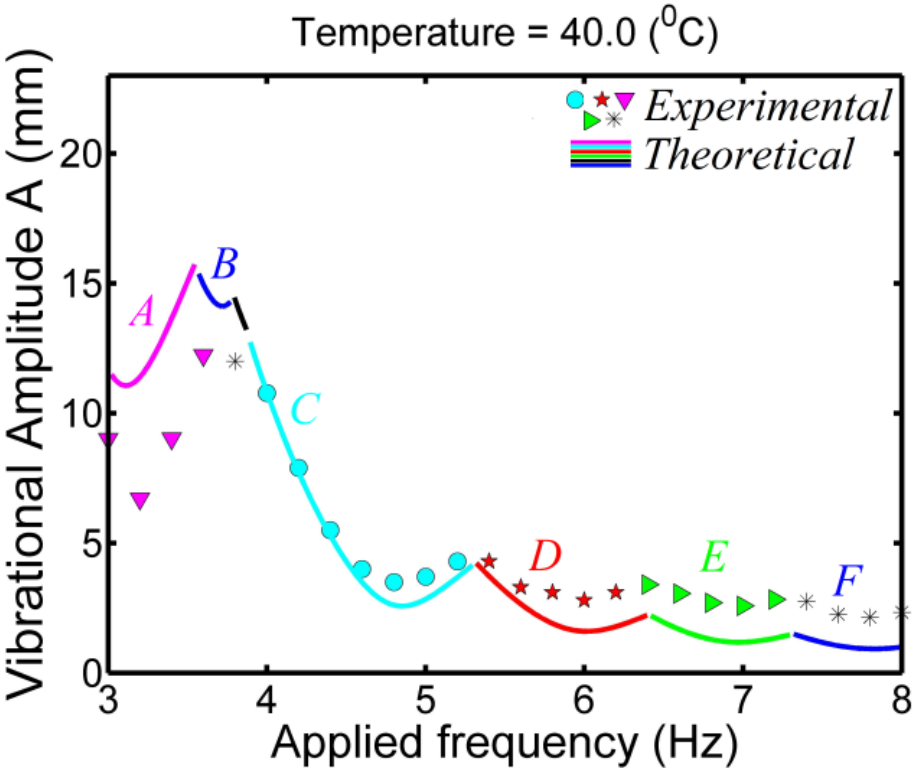
Temperature = 40.0 (^{0}C)
Experimental
Theoretical
Vibrational Amplitude A (mm)
Applied frequency (Hz)
A
B
C
D
E
F
0
5
10
15
20
3
4
5
6
7
8

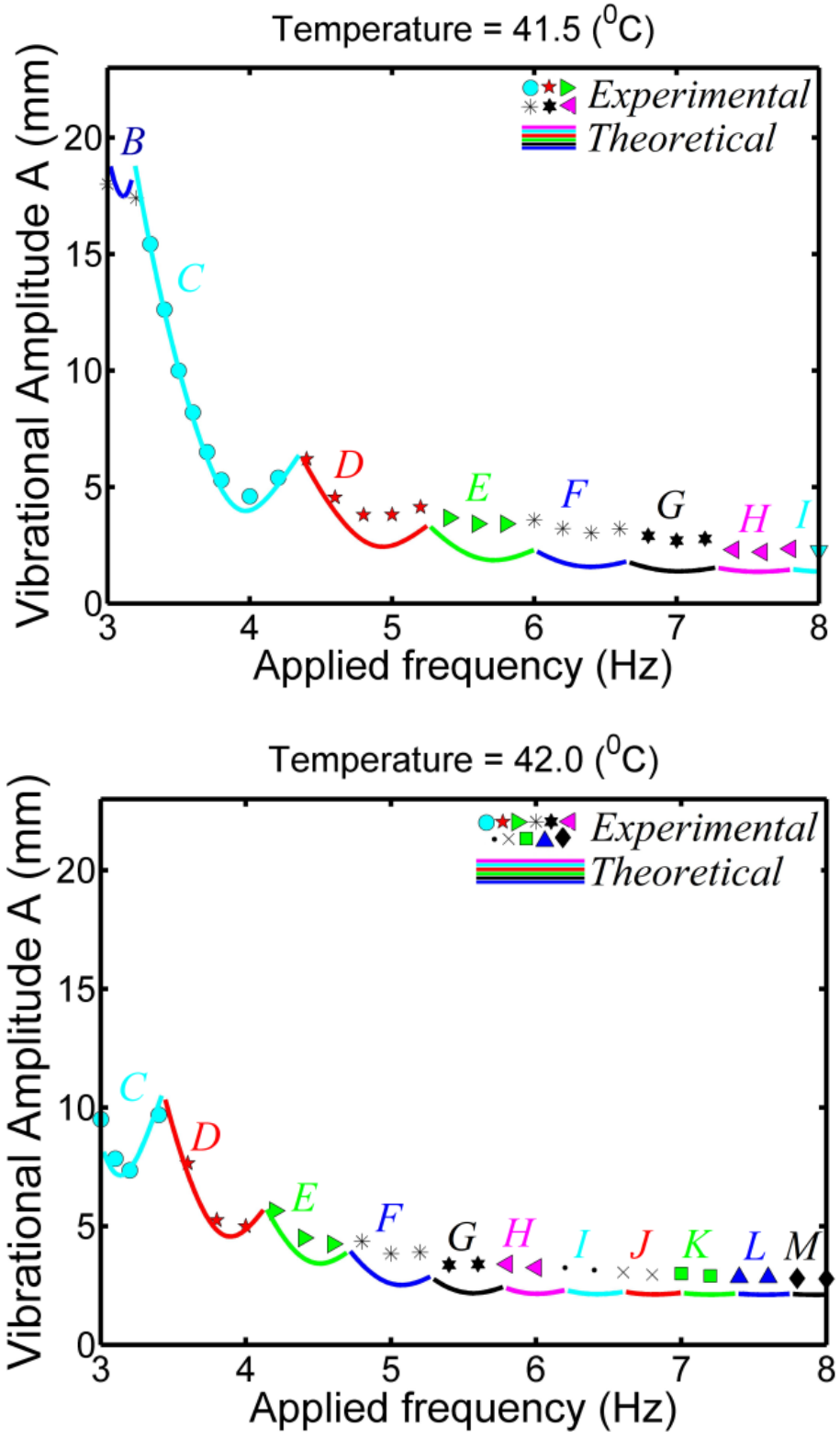

Figure 3.8: Direct comparison between experimental data and the theoretical results based on linear stability analysis with viscous damping correction

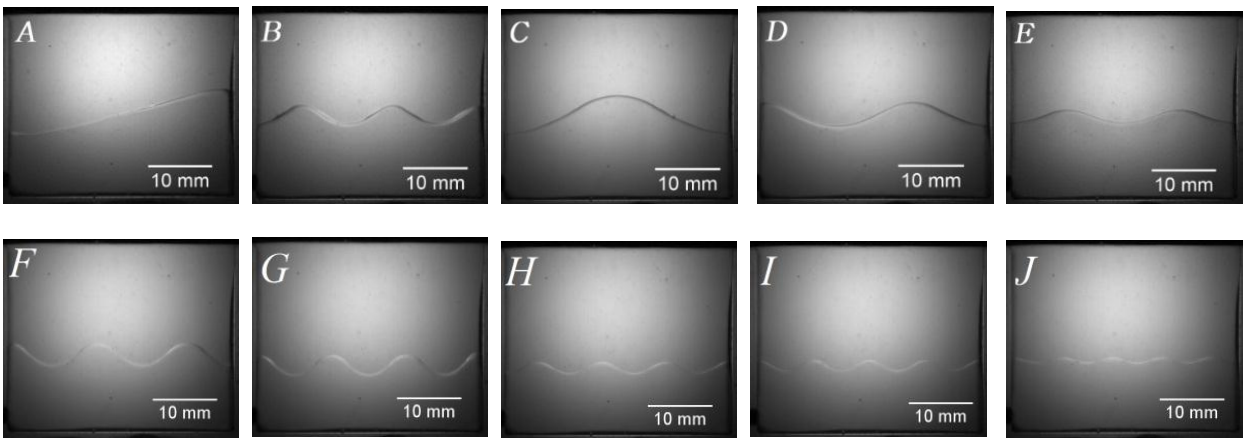

Figure 3.9: Interfacial modes of excitation. B alone is harmonic, all other modes are sub-harmonic.

However it should be noted that the accuracy of the measurement of linear damping rate decreased with the increased in the number of waves. Data recording images had limited resolution and as the number of waves increased the accuracy of the measurement decreased. Also for Mode A, inclusion of damping resulted in overshoots to the predicted threshold in comparison to experimental work. This is due to the fact that increased viscous damping results from boundary layer and bulk phase stresses. However for current theoretical results measured linear damping rates are naturally introduced via bulk viscous damping modelled by effective viscosities in the Navier-Stokes equations. For initial modes wall effects dominate as explained above but for higher modes wall damping effects diminish and bulk phase stresses start dominating.

3.4.3 Miscible Instability Threshold

Immiscible Faraday instability, as explained and analysed above, has been well studied and, with certain assumptions, provides a good prediction for experiments from theoretical work. However miscible Faraday has generated very less attention in previous research work. This section is a brief description of miscible Faraday methodology, challenges and results in

comparison to immiscible Faraday instability. It is important to understand that assumption of very thin interface as considered in immiscible fluids system is not true in miscible case.

In miscible Faraday instability the cell is initially in stable configuration with initial condition at fixed temperature below consolute temperature, then heated above consolute temperature (42.5 ^{0}C) and let the interface grow for a required thickness for a fixed time with the diffusion process, and then after subjected to vertical vibrations. The initial phenomenon of the interface was observed similar to immiscible instability and grew itself to an extent which later led to the mixing of the liquids (see Fig. 3.10). The instability grew and ended with complete mixing of two liquids over a volume. This mixed volume was found to be considerably larger than the initial diffuse region.

(a)

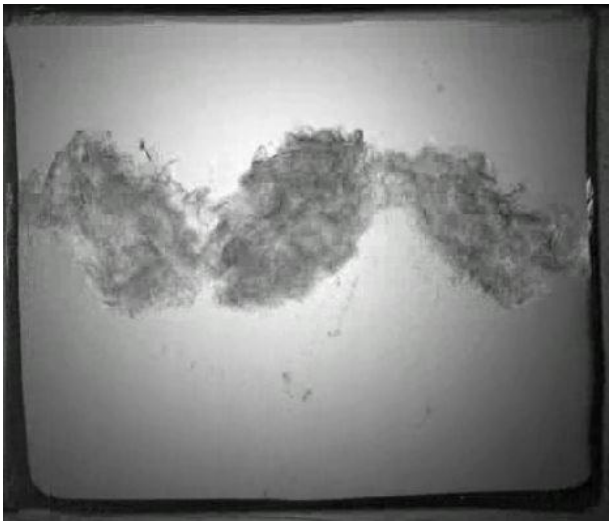

(b)

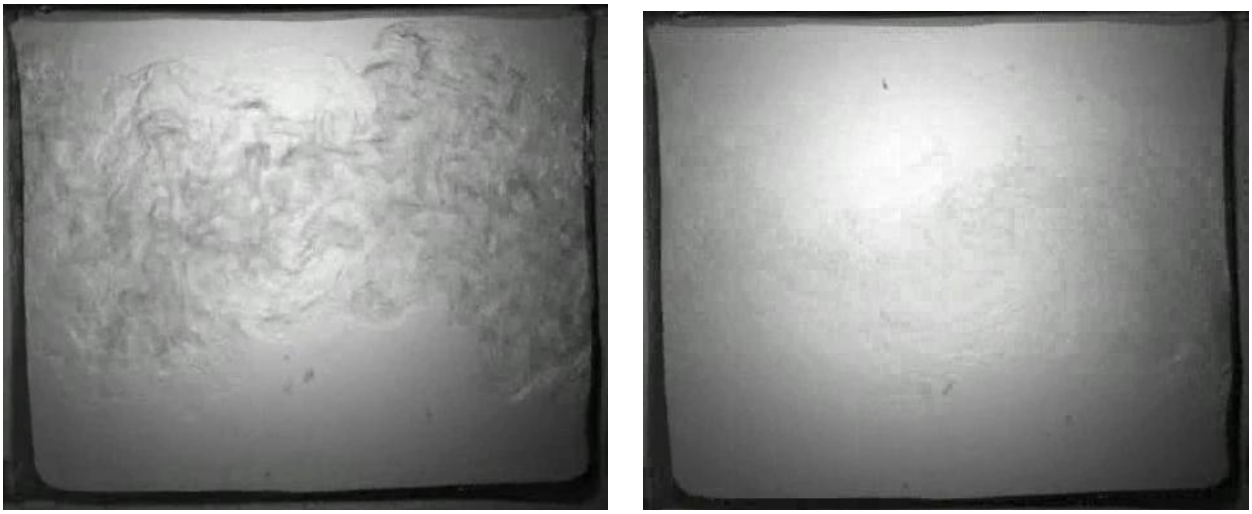

(c) (d)

Figure 3.10: Development of Faraday instability in miscible fluids, instability destroy itself and result in complete mixing

The miscible fluids situation was unlike immiscible Faraday with diffused interface and close to zero interfacial tension. In the miscible Faraday, the diffusion of momentum and species stabilize the diffused interface. Also distinct surface elevations or depressions do not exist in miscible fluids system in opposite for immiscible systems where these elevations exist due to inertial forcing from external acceleration. In its place the destabilization effect of short wavelengths is believed to occur from the transverse variation of density. In other words the destabilization of a diffuse interface in the presence of vibration is analogous to the Bénard instability where even an erstwhile quiescent layer that is stably stratified can experience sustained flow when subjected to inertial vibrations (Shukla & Narayanan, 2002). In such a problem, larger external acceleration results in small wavelength at the onset of the instability.

While immiscible system has a density jump on interface, miscible system has density gradient to initiate the instability. Near the critical threshold, immiscible Faraday instability reaches a steady state. However in miscible case, instability destroys itself, mixing fluids by convective forces eventually. Once the instability sets in, the gradients begin to weaken as a result of convective mixing. This in turn causes the waves that characterize the secondary motion, to

disappear. In other words the miscible layer Faraday problem is necessarily transient and can never attain a periodic steady state unlike its immiscible counterpart.

When this interface was subjected to vibration, concentration gradients were reduced, wave structure vanished and liquids formed a mixture layer in between two pure solutions. Miscible threshold also had dependency on the fluid interface thickness which is in turn a function of the waiting time before initiation of vibrating motion. The existence of diffusion layer shortens the time of a rise of instability at the interface. For this study experiments were done with fixed waiting period to study effects of the interfacial thickness.

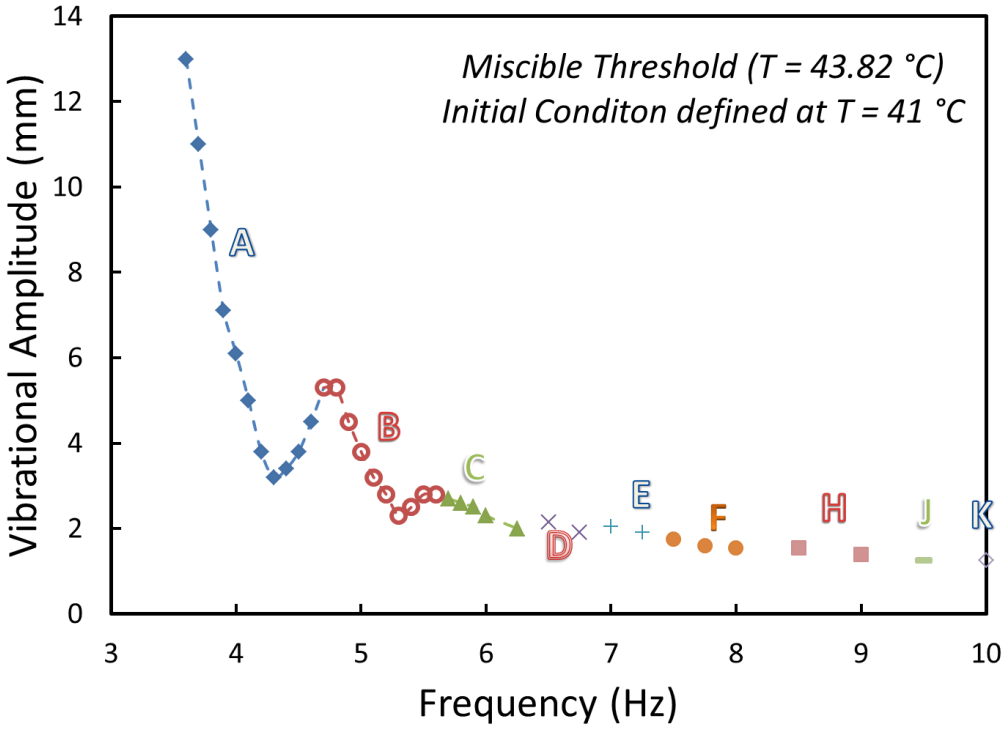

(a)

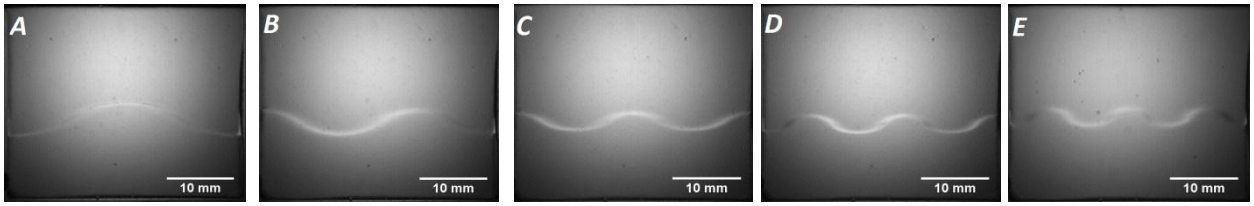

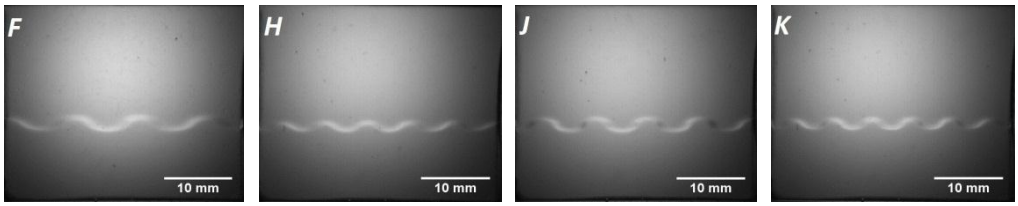

(b)

Figure 3.11: (a) Experimental thresholds for a bilayer of FC72 (h1= 12.75mm) and 1 cSt silicone oil (h2=16.75mm) in a 35mm*29.5mm*5mm cell. Data points differentiated with colour and marker indicate the excited mode with initial conditions defined at 41 ^{0}C and waiting time of 2 minutes (b) Interfacial modes of excitation at onset. All modes observed are sub-harmonic.

In the miscible fluid set, the diffusion of species stabilized the mixing region in contrast to immiscible fluid set in which interfacial tension stabilized the system. As in the experiment heavier liquid was kept below and lighter liquid was filled in the upper part of the cell, so that in ground based experiments, natural convection oppose the mixing of solution with diffusion (stabilizing buoyancy force). Thus, the effect of gravitational acceleration matched with previous observations that smaller diffusion layer gives the effect of delayed development of instability. However, for higher gravity level a larger gradient of density can exist and can generate higher amplitude of wave. While inertial forcing promotes destabilization of the interface in immiscible case, miscible case has density variation to achieve the same effects.

It has been shown in Figure 3.11, sets of threshold data for cells filled with FC72 and 1 cSt silicone oil obtained in miscible fluid experiment at temperature T = 43.82 ^{o}C (well above consolute temperature value which is equal to 42.7 ^{o}C) with initial condition set at immiscible at temperature T = 41 ^{o}C. Frequency ranges were chosen to best showcase discretization. At higher frequency, the system behaved likes an infinite system and modes started to change frequently without much change in amplitude. Lower bound of frequency is restricted with experimental constraint for achieving amplitude. However the lowest mode achieved corresponds to one wave, representing the second mode. Only sub harmonic modes were

observed. The experimental data were differentiated with mode number and corresponding mode images are also presented in Fig. 3.11 (b).

3.4.4 Comparison between immiscible and miscible systems

The classical form of the Mathieu equation (discussed in section 2.1), depicts the parametric excitation of a linear harmonic oscillator. The dispersion law presented by Benjamin & Ursell (1954) shows that the square of the natural wave frequency of a Faraday system is determined by the fluid density and surface tension. For this particular fluid system density difference overpowers the effects of surface tension, thus giving importance to initial conditions used for miscible system. For results shown in Figure 3.11 initial condition was set at temperature T = 41 ^{o}C. It is thus necessary to compare immiscible fluid system results at temperature T = 41 ^{o}C with miscible fluid system.

From Figure 3.12 it became evident that the initial condition used for experimental repeatability played an important role in miscible experiments results. Miscible experiments results obtained with initial condition of temperature T = 41 ^{o}C, fits well with results of immiscible experiment results at temperature T = 41 ^{o}C with miscible fluids results slightly unstable in comparison with the immiscible ones This comparison confirmed the theoretical deduction that density difference plays a much greater role in determining the threshold and wavelength.

However miscible Faraday wave's critical threshold showed a little shift when compared to its immiscible part. As shown in the figure 3.12 miscible Faraday requires a less vibrational energy ($A\omega^2$) in comparison to immiscible fluid. This behaviour is explained by the fact that vanished interfacial tension in miscible fluids and lower density gap in between fluids make the system more unstable which has been shown as stabilizing agent in the previous chapters.

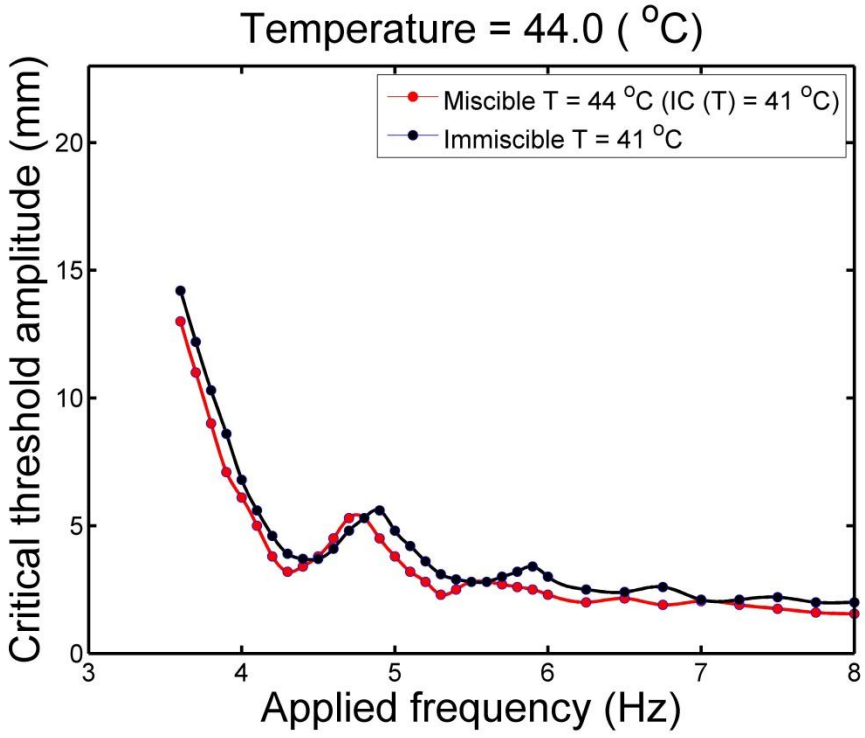

Figure 3.12: Comparison of miscible system to corresponding immiscible system with waiting time of 2 min

3.4.5 Thickness of diffused interface in miscible fluids

Miscible experiments are also defined by thickness of interface before starting of vibration. This interface thickness depends on the waiting period. A constant waiting period was used to make constant interface thickness for miscible experiments. However its effects on the wavelength of the instability were of importance. Large waiting periods led to thicker interface and weaker density gradients and were found to be more unstable for defined amplitude. In simple words for defined vibrational amplitude, instability grew for lower value of frequency in long waiting period experiments. This has been shown experimentally in figure 3.13 below.

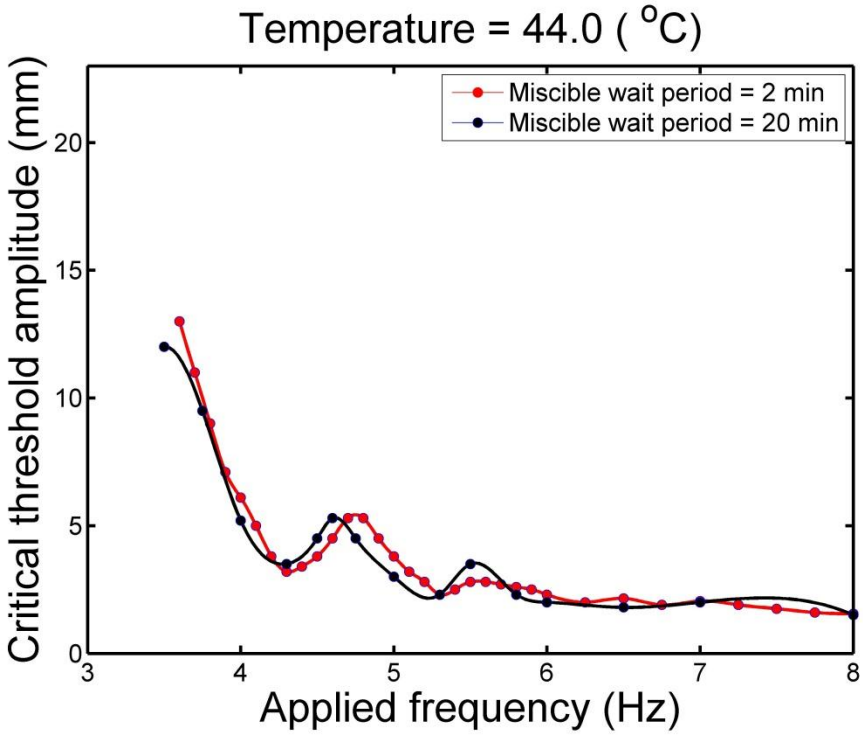

Figure 3.13: Comparison of miscible system with different waiting period

Chapter 4

FARADAY INSTABILITY IN A MICROGRAVITY ENVIRONMENT

It is well known that the Faraday instability is a manifestation of gravity-capillary wave phenomena wherein discernible wave patterns emerge on a fluid interface that is subjected to perpendicular oscillations. Here, the resonant behaviour is governed by various factors such as the system geometry, gravity, and interfacial tension. A comprehensive understanding of the Faraday instability thus entails a clear demarcation of the role played by each of these effects. Interestingly, both gravity and interfacial tension play conflicting roles which are primarily determined by the imposed frequency of excitation. For example, it has been shown by Batson *et al.* (2013) that the gravity plays a dual role of aiding the instability at low frequencies of excitation and suppressing it at higher values. Though a similar effect is also manifested by interfacial tension, understanding its sole influence becomes very difficult under terrestrial gravity conditions as the density difference effects dominate here over the capillarity. Hence, performing experiments under reduced gravity conditions were very essential and the micro-gravity platform (where density difference effects are vanishing) offered by aircrafts that follow parabolic trajectories are very conducive in this regard. It may be noted that such a study was motivated not only from an academic point of view, but also with regard to relevant applications involving fluidic and microfluidic systems in the space station.

The present experiments on Faraday instability involves oscillating a Hele-Shaw type cell containing binary fluids, perpendicular to their interface during the zero-g phase of a parabolic flight. The use of binary fluids here provided a convenient option of changing the coefficient of interfacial tension by temperature control. Here, the interfacial tension between the fluids pair approached to zero as their temperature tends to the upper consolute value and there is no drastic alteration to the other properties of the fluid layers.

Micro-gravity experiments with a gravity level of the order of 10^{-2} g were conducted on-board an aircraft undergoing a parabolic path. For this purpose we participated in three CNES parabolic flight campaigns for zero-g experiments (CNES PFC VP115, 11-22/05 2015, CNES PFC VP123, 14-25/03 2016 & CNES PFC VP128, 27/03-07/04 2017). This chapter discusses the flight dynamics, microgravity experiments, associated results in comparison with ground-based results, challenges and uncertainty in the microgravity experiments.

4.1 Parabolic flight dynamics

Parabolic flights are widely used to create free-fall conditions for microgravity experiments on earth. It is easily accessible and provides cost effective interaction between the on-going experiment and researcher in zero-g environment. Though experimentalist in parabolic flight identifies gravity to be zero, the acceleration is changing in reality and the terms "microgravity" and "zero gravity" are not thus technically correct.

Aerospace engineering has melodramatically enriched since the dawn of first human flight. Aircrafts' pilots have become skilled in altering the forces and accelerations that passengers experience. Weightlessness is often used to describe the perception that astronauts experience during free-fall. Astronauts perceive themselves to be weightless because they are falling under the influence of the same gravitational field as the spacecraft, so there is no reaction force on the astronaut by the spacecraft. As per the Einstein's equivalence principle, no simple physical transducer can conclude if an applied acceleration is due to gravitational or inertial force and this includes the sensors in the human body also known as vestibular system that helps to keep us balanced and to give realization of directions. Zero-g parabolic flights provide similar free-fall conditions, providing experimentalist a ground to develop and collect initial data for ISS (International Space station) experiments.

For manoeuvring the parabolic flight, at a set point, the pilot gradually pulls up the nose of the aircraft and it starts climbing at an angle (see the sketch in Fig. 4.1 for the trajectory of the airplane for one parabola). This phase lasts for about 20 seconds, during which the aircraft experiences acceleration between 1.5 and 1.8 times the gravity value at the surface of the Earth, i.e. 1.5 – 1.8 g. At an altitude of 7500 meters, with an angle of around 47 degrees to the horizontal and with an air speed of 650 km/h, moving from hyper-gravity phase to microgravity phase, the pilots manoeuvre to cancel the lift generated by the wing (angle of attack of the wing equals zero). While at the same time the flight engineer reduces the thrust from the engines to compensate the drag. This is because of the aircraft generating appropriate lift and thrust to produce the desired vertical and longitudinal accelerations, respectively. By following the above procedure microgravity levels of the order of 10^{-2} g is obtained for the experiments.

The aircraft is surrounded by air and thus aero-dynamic lift, drag and thrust play a major role. At this point the aircraft follows a free-fall ballistic trajectory, i.e. a parabola, lasting approximately 20 seconds, during which weightlessness is achieved.

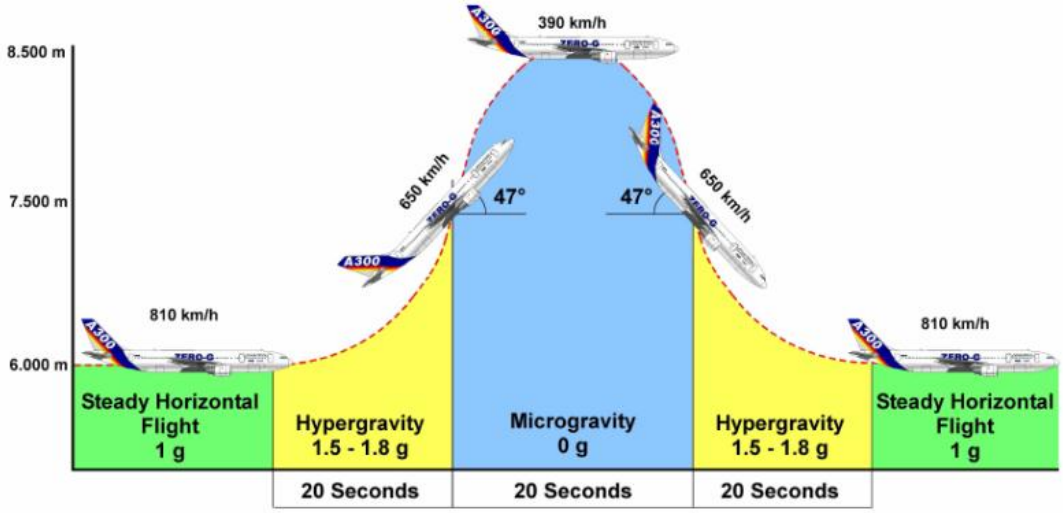

Figure 4.1: Path of one parabola in a parabolic flight. Approximately 20 second of microgravity time available for experiment in each parabola.

The path of parabola is a part with one of its locus located at the centre of the earth. The peak of the parabola is achieved at around 8500 meters, at which point the speed has dropped to about 390 km/h. At the end of the weightlessness period, i.e. again at 7500 m, the aircraft must pull out of the parabolic arc, a manoeuvre which gives rise to another 20-second period of approximately 1.8 g on the aircraft. At the end of these 20 seconds the aircraft again flies a steady horizontal path at 1 g, maintaining an altitude of 6000 m. The period between the start of each parabola is three minutes, i.e. a 70 second parabolic phase (20 seconds at 1.8 g + 3 to 5 seconds of transition + 20 seconds of weightlessness + 3 to 5 seconds of transition + 20 seconds at 1.8 g), followed by a 110 second period at steady level 1 g flight. Regardless of the aircraft trajectory including large (45°) pitch-up and pitch-down attitudes, the experimentalist feel a net force perpendicular to the floor of the aircraft.

Parabolic flights are prone to environmental conditions and are also limited by flight dynamics. Flying in ever changing earth's environment generates some unwanted residual acceleration, which can be detrimental to physical experiments. The pilots are always trying to compensate for the disturbing forces from surrounding environment and engine vibration. As a result, the microgravity level attained in a parabolic flight has some deviations of the order of +/-0.05g at a frequency of around 1 Hz. Also mechanical vibrations caused by engines and shocks in the aircraft also exist and are noticeably higher due to the nature of the flight.

For some physical experiments even small disturbances in gravity level can affect results in great order, Faraday waves are an example of that. Section 4.3 carries out a case study for a particular parabola to study its effect on generated waves. The Faraday instabilities discussed in previous chapters have shown a great deal of dependency on gravity. It is thus interesting to understand how instabilities will behave in the absence of gravity. A relevant application of this behaviour is for the propellant dynamics in a rocket fuel tank, whereupon vibrations during take-off are known to induce Faraday initialized sloshing. Another example is related to spacecraft maneuvers done for the altitude control in orbitfor which spacecraft sends short-timed bursts of gas in order to control their orientation, in azero-g environment. In Faraday instability, gravity not only possesses a destabilizing effect (similar to its role in the Rayleigh-Taylor instability in half a period of vibration), but also its contribution to the natural frequency of a mode results in a shift towards higher wavenumbers when it is removed.

4.2 Results and Discussion

A series of immiscible and miscible experiments were performed in CNES Parabolic flight campaign to determine behaviour of Faraday instabilities in gravity free environment as the Faraday instability is a demonstration of capillary-gravity waves. Current set of binary fluids gives a unique opportunity to understand its behaviour when both the capillary and gravitational effects vanish. An experimental study has been performed and discussed in previous sections where the reduction in capillarity is achieved through the temperature

increase of the binary fluid system whereas the microgravity condition was realized in a parabolic flight environment. Interestingly, in microgravity environment and low surface tension region with thermal control results into a system where wall boundary effect diminished and continuum of modes are observed. Only certain experiments are performed in parabolic flight limited to time availability in parabolic campaign. Certain miscible experiments were performed as well, but they have been found to be dependent upon initial conditions (see Chapter 3). However due to a very short period of two minutes between two parabolas of same series, it was difficult to maintain similar initial conditions.

Very importantly, for the purpose of understanding the evolution of Faraday instability in micro-gravity conditions, it is planned to carry out miscible Faraday instability experiments in the ISS. The additional benefit that comes out of the microgravity experiment is its ability to form exact diffuse interface between the fluids. Under terrestrial conditions i.e. normal gravity, there is always an alteration of the mixing region due to the convection associated with change of temperature of the liquids. This can be completely eliminated in the zero-gravity conditions. Carrying out these experiments in the ISS is necessary due to the fact that the thermal time scales are generally large and so, performing the desired experiments within the short time offered by parabolic flights, is very challenging. Thus in zero gravity time period of 15 − 20s in the parabolic flights gives only an estimated range for the threshold. It may be noted that an important challenge that will arise in zero-gravity conditions corresponds to the de-mixing of the liquids. In the absence of the gravity, there is no natural motive force that causes the liquids to separate. In this regard, some other means of separation have to be tested and implemented. Hence, various preparatory steps have to be carried out in the parabolic flights before performing the full scale experiments in the ISS. Correspondingly, different aspects of Faraday instability are aimed to be addressed in the present parabolic campaign. Microgravity experiments also confirmed the existence of a crossover frequency (f*), on either side of which gravity plays opposing roles (See Fig. 4.2(c)). Crossover frequency is the frequency below which the system was found to be destabilized in the absence of gravity. For immiscible experiments effects of temperature are studied using the binary liquids system described in Chapter 3, for temperatures T = 38 ^{0}C, 40 ^{0}C and T = 41.5 ^{0}C. Variation of temperature was set only before 5

and 8 minutes break between two series of parabola, such that enough time is available for setting initial condition to make liquids in equilibrium before start of each series of temperature. Figure 4.2 presents the threshold curves for the three above-mentioned temperatures in the immiscible regime in ground-based and parabolic flight environments.

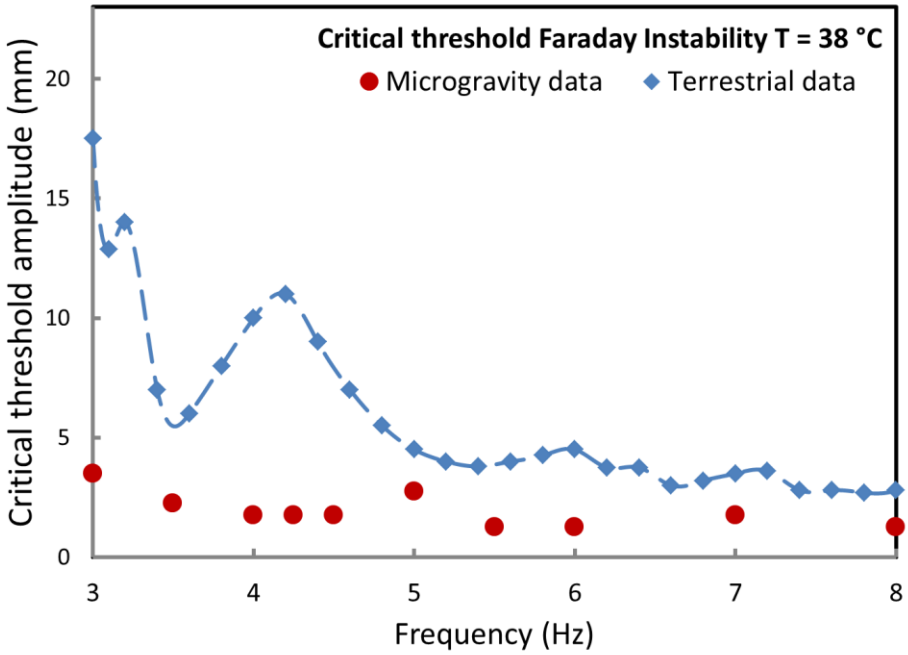

(a)

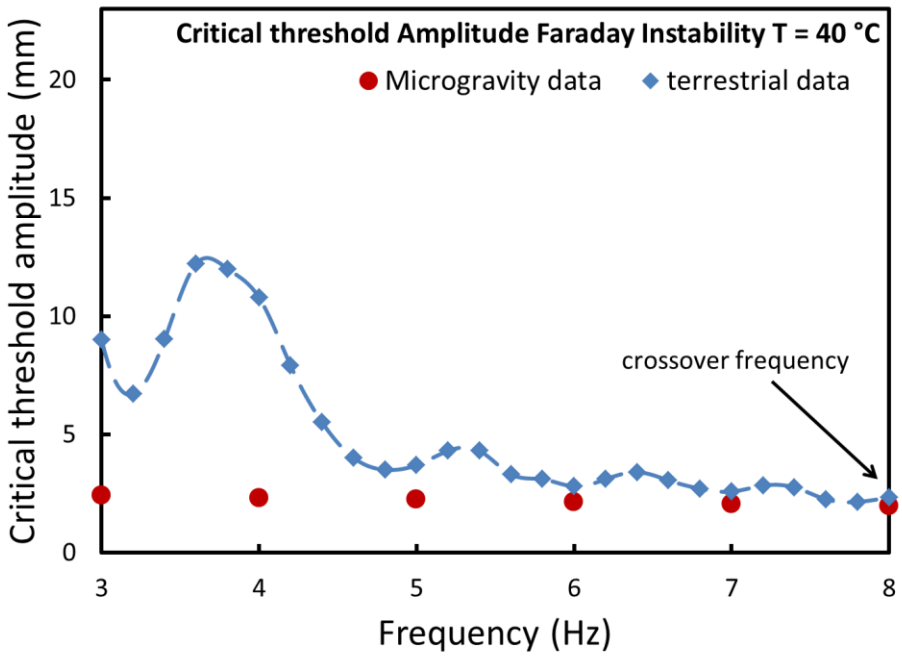

(b)

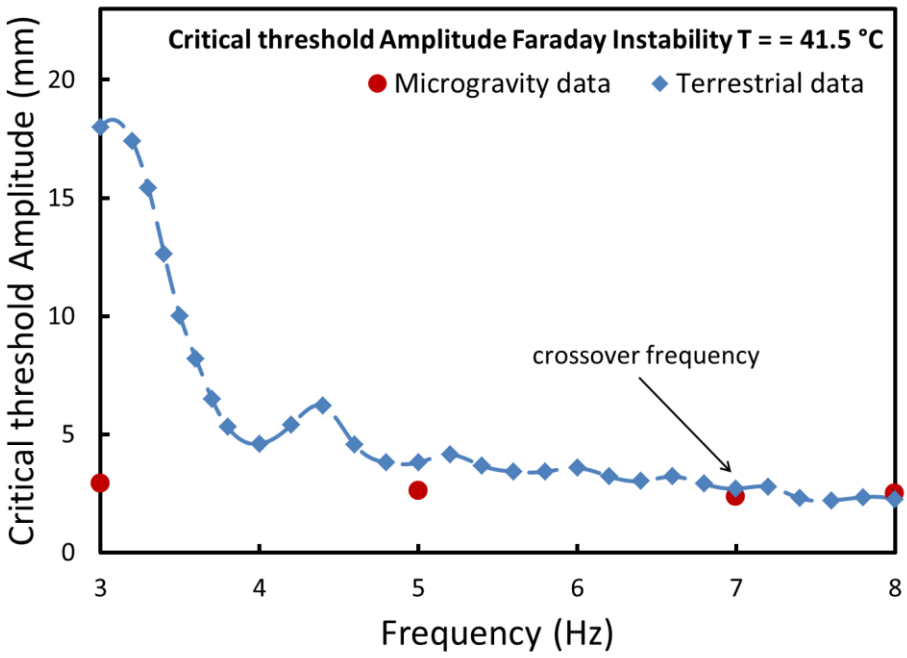

(c)

Figure 4.2: Critical threshold amplitude measured in micro gravity conditions in comparison with terrestrial experiments at temperature for (a) T = 38 ^{o}C, (b) T = 40 ^{o}C and (c) T = 41.5 ^{o}C.

One of the most important observations is the loss of clear discretization of the instability under microgravity conditions as has been observed in the terrestrial experiments. It results now into a continuum mode system. These aspects of the experiments indicate that in microgravity environment even smaller size cell can behave as an infinite boundary system. There is a crossover frequency below which the system was found to be destabilized in the absence of gravity. The existence of crossover frequency is the result of the presence of higher wave number selection in a microgravity system than earth based experiments. The microgravity experiments therefore experiences much higher viscous effects at large frequencies, resulting in higher threshold amplitudes for instability. The present experiments clearly depict the existence of this crossover frequency and its drift to lower frequencies as the coefficient of interfacial tension is decreased.

4.3 g-jitter in Parabolic Flight

This section focusses on understanding the influence of g-jitter on the evolution of Faraday instability in micro gravity environment. The realization of zero gravity conditions is made possible by virtue of the aircraft's parabolic path wherein the outward centrifugal force exactly balances the gravitational pull on the aircraft and its occupants. Diwakar *et al.* (*Private communication*) have correspondingly shown that for low frequency excitation, the removal of gravity destabilizes the fluid layers quickly though the response waves have a lower wavelength that should have led to viscous stabilization. Incidentally, a deeper characterization of the instability behaviour in parabolic flights is complicated by these two important factors.

The first issue concerns the short zero-g time window available with the parabolic flights (around 20s). Correspondingly, a precise prediction of the onset threshold of Faraday instability is not possible. As the time required to observe a tangible interfacial wave increases drastically when the threshold is approached, only a tentative range for the threshold can be estimated within the time of approximately 20s provided by the parabolic flights. The second and more severe issue concerns the ever-present errors in flight dynamics whose influence on the Faraday waves form the primary focus of this work.

Ideally, the parabolic flights are meant to emulate a perfect zero-gravity condition even within the earth atmosphere. However, various factors such as atmospheric turbulence, mechanical vibrations caused by engines etc., make it challenging to create an ideal zero gravity environment. As a result, the microgravity level attained in a parabolic flight deviates of the order of +/-0.05g due to g-jitters. Though such deviations are barely detected by the human vestibular system, their influence on physical experiments like Faraday instability is not negligible. As the natural frequencies of the fluids are constrained by the imposed frequency during resonance, any perturbation in the gravity levels is immediately reflected in the wavelength of the Faraday waves. In the present work, the influence of these g-jitters has been analysed for different imposed frequencies and fluid temperatures. Correspondingly, one such scenario is illustrated in Figure 4.3. In Fig. 4.3 (a), the acceleration levels are shown in x, y and z directions for one parabola with the parameter excitation of frequency 5 Hz and amplitude of

2.25mm. The z-component of the acceleration is the highest. The errors are within 2%, 1.5% and 1% in Z, X, and Y directions, respectively. Figure 4.3 (b) shows the z-component of the gravity together with the wavelength of the Faraday wave measured at different time instants within the timeframe of this single parabola.

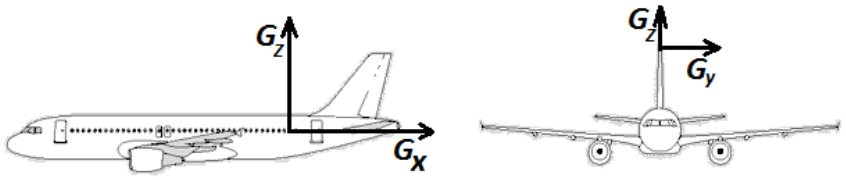

(a)

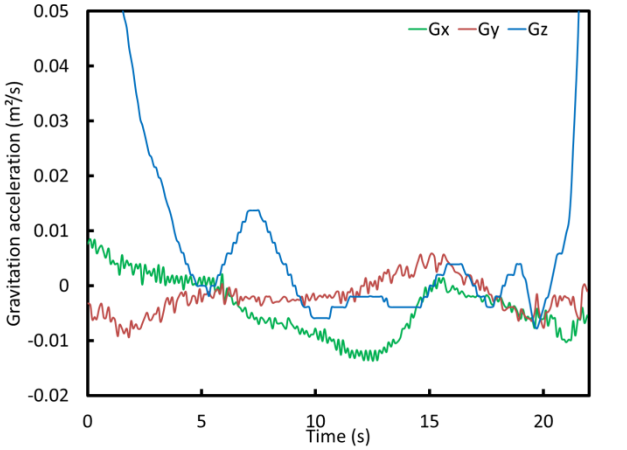

(b)

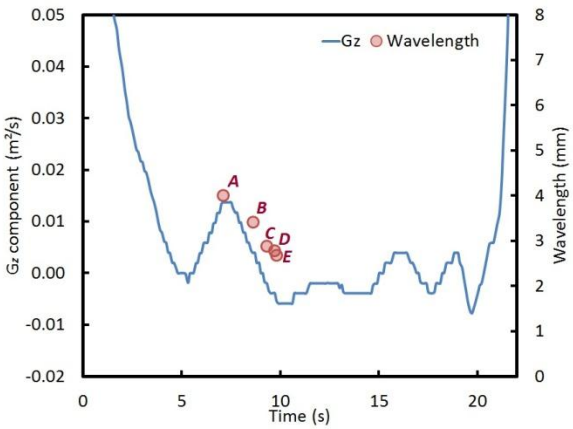

(c)

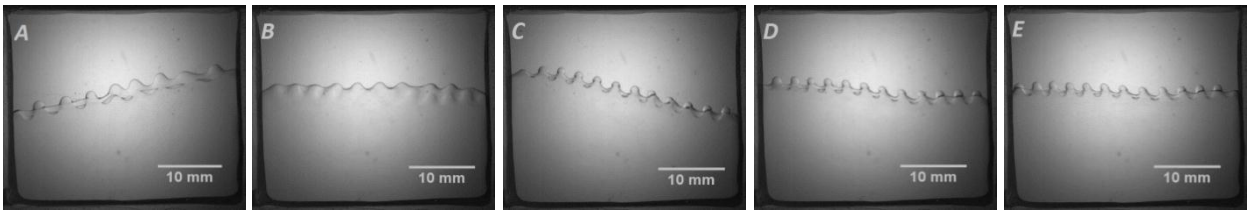

(d)

Figure 4.3: (a) The different axes of the airplane represented by normal, longitudinal and lateral in Z, X and Y directions respectively (b) Acceleration data in a real-time parabola where G_z, G_x and G_y are the acceleration perpendicular to base plane, in direction from tail to front of aircraft, and in the direction from left wing to right wing when looking into cockpit direction,

respectively (c) gravity level at the z-direction and wavelength at selected time instants (d) Faraday instability showing varying wavelength within one parabola. Frequency f = 5 Hz and amplitude A = 2.25 mm.

Several images obtained during this parabola are shown in Fig. 4.3 (d) and are analysed for determining the wavelength, oscillation period etc. Interestingly, contrary to a constant wavelength behaviour observed for earth based experiments, parabolic flight experiments have varying wavelengths ranging from 2.67 mm to 4.00 mm with an error of 0.05 mm. The difference is quite large (over 30% change).

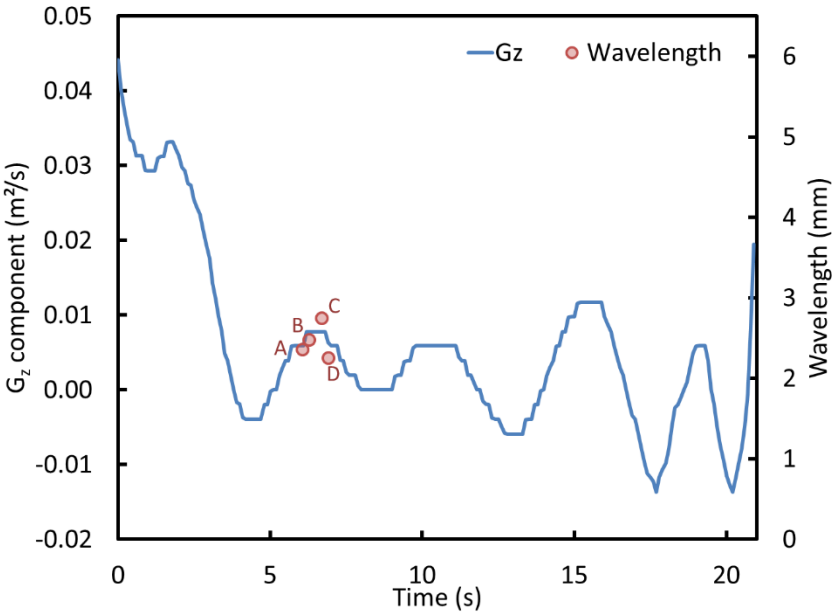

(a)

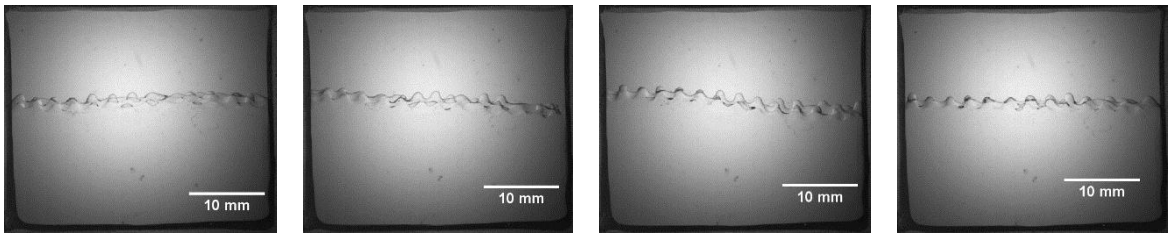

(b)

Figure 4.4: (a) gravity level and wavelength at selected time instants (b) Faraday instability showing variation wavelength within one parabola. Frequency = 7 Hz and amplitude = 2.25mm.

Out of many observed cases another one is also presented in Figure 4.4 where the wavelength is varied from 2.25 mm to 2.75 mm (18% difference). In microgravity condition, the determination of the exact wavelength and the mode thus becomes a tedious task due to small disturbances (g-jitters) present in the aircraft and corresponding variation in wavelength. The forced acceleration in *y* direction is less than 1% of gravitation acceleration, which is generally considered to be an ideal condition. But, even this slight disturbance forces the interface to slant and provide varying boundary length. These results indicate a great shift of experimental results in parabolic flight and provide requirements for corrections in order to reach truthful results.

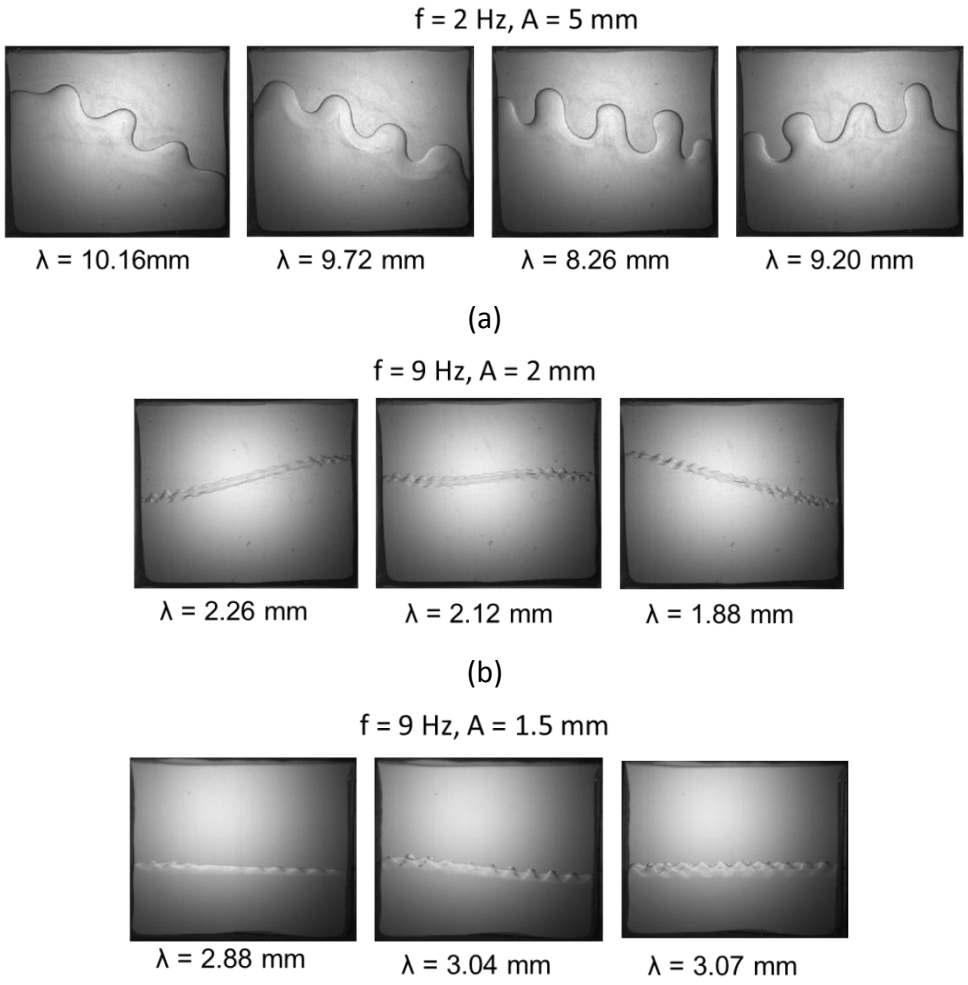

Figure 4.5: Examples of variation of wavelength for (a) f = 2Hz; A, 5mm (b) f = 9Hz; A, 2mm (c) f = 2Hz; A, 1.5mm

It is important to note that g-jitter experiments cannot be planned and observation of such experimental data is dependent of large data collection. As well as in certain parabolas, the g-jitter completely destroys the interface thus not allowing any probability of recording such observation. Following are few example in Fig. 4.5 observed in the parabolic flight campaign showcasing the variation in wavelength.

Chapter 5

Conclusion and Perspectives

In the present thesis the Faraday instability generated as a result of parametric excitation has been experimented and validated with analytical work. An intriguing experimental analysis has thus been performed to characterize Faraday waves in such regimes. The reduction in capillarity was achieved through thermal control of a novel binary liquid system, whereas the vanishing gravity force condition was realized in a parabolic flight environment. The critical external acceleration required for the onset of instability has been generally observed to decrease in these conditions, although the corresponding critical wavelength reduces drastically so as to make the resulting viscous dissipation compensate for the loss of stability arising from the reduced capillarity and gravity forces.

The current study specially aimed to show the role of wall proximity and damping caused by frictional forces and sidewall stress for the small forcing frequency. A linear stability analysis based on Fourier-Floquet method was performed in order to get an understanding of the instability and how different parameters affected the threshold of the instability. In experimental observations, it has been validated that the assumption of stress-free sidewalls was not completely true and produced variation from theory specifically in small cell sizes. The reason came from the fact that the two liquids contacting the solid sidewalls inevitably produced a static meniscus, which emitted waves during vibration, and violated the assumptions of a flat interface and the simple viscous friction of the fluids on the wall are responsible for the discrepancy between our experimental results and existing stability analyses. The experimental data produced a precise intensity of these two effects, but they do not allow to discriminate between each component in the global discrepancy. We successfully measured the cumulative effect of both these effects (capillary waves from the meniscus and viscous friction at the walls) for the correction of the analytical model. This correction in the theoretical calculations with the viscous damping rate helped in achieving a better understanding for the prediction of the experimental critical amplitude for sub-harmonic and harmonic modes. This observation showed that the majority of the viscous damping was the result of boundary layer effects instead of internal damping for the first primary modes. For higher modes, the wall effects diminished but the bulk damping became dominant because of the increased choppiness of the waves. Viscous damping from top and bottom walls affected

sub-harmonic or super-harmonic waves much higher in comparison to harmonic waves. For higher modes theoretical and experimental damping rates provided much better match thus reducing the need of viscous damping correction. From the analysis and results above one could state that the container size needs to be at least five times to the wavelength produced in the system in order to remove viscous damping effects such that the system could act as an infinite size system. A damping coefficient derived from linear theory for unbounded containers with specific wave numbers could be used to describe any discrepancies between a linear model in bounded containers and experiment. For a confined rectangular geometry, damping correction provided a way to predict the corrected threshold with theoretical calculations based on linear stability analysis.

For miscible experiments the choice of binary fluids permitted to study different cases of miscible fluid instability without filling again the cell which is impossible in the short time parabolic flight as well as it allowed to return to exact similar charge conditions before starting of each experiment. It provided some new understanding of the physics of the capillary-gravity wave phenomenon. The value of surface tension coefficient reduced in the immiscible regime and approached to zero in a miscible system as the temperature of the fluids system was gradually increased to the consolute temperature. The system, thus uniquely provided the opportunity for understanding the sole influence of surface tension coefficient on Faraday instability at the cost of very marginal change in the viscosity values.

The zero- gravity experiments unveiled the dual role of gravity and interfacial tension on the evolution of Faraday instability. Comparison of terrestrial experiment with parabolic flight experiments has shown the existence of a crossover frequency, below and above which gravity plays opposing roles. Increasing the temperature in parabolic flight environment resulted in lowering this cross-over frequency. Under microgravity condition the energy required for the appearance of instability drastically reduced and the discretization of modes disappeared even in Hele-Shaw cell for a fluid pair with low interfacial tension. However in the experimental sets, the reduction of interfacial tension with temperature increase played a counter intuitive role of making the system more stable at high frequencies due to the choppiness of waves. The

explanation for this could be the secondary effect of change in the critical wavelength, which caused an increase in viscous damping, overwhelming the primary effect of change in interfacial tension.

The reduction in interfacial tension was obtained by changing the temperature of the binary fluids pair which also altered the density difference between the fluid layers. Under terrestrial conditions, the neutral curves representing the variation of critical amplitude with frequency shifted leftwards and it was difficult to associate this behaviour solely to the variation in density.

Further this work can be progressed with numerical analysis, for which phase field modelling can be an excellent choice. The phase field approach delivers a continuum thermo dynamical model able to treat multi-phase problems. An auxiliary variable - the phase field - is added to the usual set of state variables in order to provide an explicit indication of the dynamic of the phase. This parameter may take different values for different phases and undergoes a rapid but smooth variation in the interface region. In mono-component systems the density ρ (scaled by the liquid density) is the natural order parameter: $\rho=1$ designates the liquid region of the system and $\rho\approx0$ the gaseous phase.

In the phase field model the interface is introduced by gradients of the phase field. The formalism is based on a free energy, giving complete setup as a single homogeneous phase. For a system in equilibrium and without interfacial mass exchange the free energy density has the form of a symmetric double-well potential with two minima corresponding to the two alternative phases. The advantage of the proposed method is that we do not need any interfacial condition (continuity of stress, kinematic condition…) in order to model the interface of the two fluids.

Bibliography

Amiroudine, S., Zoueshtiagh, F., & Narayanan, R. (2012). Mixing generated by Faraday instability between miscible liquids, Physical review E 85, 016326

Batson, W., Zoueshtiagh, F., & Narayanan, R. (2013). The Faraday threshold in small cylinders and the sidewall non-ideality J. Fluid Mech., vol. 729, pp. 496-523

Batson, W., Zoueshtiagh, F., & Narayanan, R. (2013). The Dual Role of Gravity on the Faraday Threshold for Immiscible Viscous Layers, Phys. Rev. E., 88; p. 063002

Batson, W., (2013). Faraday waves in small cylinders and the sidewall non-ideality. Ph.D. thesis, University of Florida.

Bechhoefer, J., Ego, V., Manneville, S., & Johnson, B. (1995). An experimental study of the onset of parametrically pumped surface waves in viscous fluids. J. Fluid Mech., 288, 325–350.

Benjamin, T. B., & Scott, J. C. (1979). Gravity-capillary waves with edge constraints. J. Fluid Mech, 92(2), 241–267.

Benjamin, T. B., & Ursell, F. (1954). The stability of a plane free surface of a liquid in vertical periodic motion. Proc. R. Soc. Lond. A, 225, 505–515.

Chandrasekhar, S. (1981). Hydrodynamic and hydromagnetic stability. Dover publications. ISBN-10: 048664071X, Mineola, New York, United States

Das, S. P., & Hopfinger, E. J. (2008). Parametrically forced gravity waves in a circular cylinder and finite-time singularity. J. Fluid Mech., 599, 205–228.

Diwakar, S. V., Zoueshtiagh, F., Amiroudine, S., & Narayanan, R. (2015). The Faraday instability in miscible fluid systems, Physics of Fluids 27, 084111.

Douady, S. (1990). Experimental study of the Faraday instability. J. Fluid Mech., 221, 383–409.

Douady, S., & Fauve, S. (1988). Pattern selection in Faraday instability. Europhysics letters, 6(3), 221–226.

Edwards, W. S., & Fauve, S. (1994). Patterns and quasi-patterns in the Faraday experiment. J. Fluid Mech., 278, 123–148.

Faraday, M. (1831). On the forms and states of fluids on vibrating elastic surfaces. Phil. Trans. R. Soc. Lond., 52, 319–340.

Fauve, S., Kumar, K., Laroche, C., Beysens, D., & Garrabos, Y. (1992). Parametric instability of a liquid-vapor interface close to the critical point. Phys. Rev. Lett., 68(21), 3160–3163.

Feng, J., Jacobi, I., & Stone, H. (2016). Experimental investigation of the Faraday instability on a patterned surface. Exp. Fluids 57, 86.

Gallaire, F., Brun, P., (2017) Fluid dynamic instabilities: theory and application to pattern forming in complex media. Philos Trans A Math Phys Eng Sci. May 13;375(2093)

Henderson, D., & Miles, J. (1990). Single-mode Faraday waves in small cylinders. J. Fluid Mech., 213, 95–109.

Henderson, D. M., & Miles, J. W. (1989). Faraday waves in 2:1 internal resonance. J. Fluid Mech., 222, 449–470.

Hill, D. F. (2002). The Faraday resonance of interfacial waves in weakly viscous fluids. Physics of Fluids, 14, 158.

Hill, G. W. (1886). On the part of the motion of the lunar perigee which is a function of the mean motions of the sun and moon. Acta Mathematica, 8(1), 1–36.

Hocking, L. M. (1987). The damping of capillary-gravity waves at a rigid boundary. J. Fluid Mech, 179, 253–266.

Ito, T., & Kukita, Y. (2008). Interface behaviour between two fluids vertically oscillated in a circular cylinder under nonlinear contact line condition. J. Fluid Sci. Tech., 3, 690–711.

Ito, T., Tsuji, Y., & Kukita, Y. (1999). Interface waves excited by vertical vibration of stratified fluids in a circular cylinder. J. Nuc. Sci. and Tech, 36, 508–521.

Johns, L., & Narayanan, R. (2002). Interfacial Instability. Springer.

Kumar, K. (1996). Linear theory of Faraday instability in viscous fluids. Proc. R. Soc. Lond. A, 452, 1113–1126.

Kumar, K., & Tuckerman, L. (1994). Parametric instability of the interface between two fluids. J. Fluid Mech., 279, 49–67.

Landau, L., & Levich, B. (1942). Dragging of a liquid by a moving plate. Acta Physicochim. URSS, 17(42).

Landau, L. D. (1987). Fluid Mechanics: Volume 6 (Course Of Theoretical Physics) Author: LD Landau, EM Lifshitz, Publisher: Bu. Butterworth-Heinemann, United Kingdom.

Ernst Florens Friedrich Chladni, (1787), Entdeckungen über die Theorie des Klanges, Leipzig

Lighthill, J., (1978) Waves in Fluids. Cambridge-London-New York-Melbourne, Cambridge University Press. XV, 504 S.

Melde, F. (1860). Ueber die Erregung stehender Wellen eines fadenfOrmigen Korpers . Ann. Phys. Chern. Ser. 2 109: 193-215

Miles, J. W. (1967). Surface-wave damping in closed basins. Proc. R. Soc. Lond. A, 297, 459–475.

Miles, J. W. (1984). Nonlinear Faraday resonance. J. Fluid Mech., 146, 285–302.

Milner, S. T. (1991). Square patterns and secondary instabilities in driven capillary waves. J. Fluid Mech., 225, 81–100.

Muller, H. W. (1993). Periodic triangular patterns in the faraday experiment. Physical Review Letters, 71(20), 3287–3290.

Muller, H. W., Wittmer, H., Wagner, C., Albers, J., & Knorr, K. (1997). Analytic stability theory for Faraday waves and the observation of the harmonic surface response. Phys. Rev. Lett., 78(12), 2357–2360.

Oersted (1813) (referenced in Wheatstone), Wheatstone (1823), and Weber (1825) as predecessors in producing and describing crispations

Raman, C. V. (1912). Experimental investigations on the maintenance of vibrations. Bulletin of the Indian Association for the Cultivation of Science, 6, 1–40.

Rayleigh, J. W. S. (1883), on the crispation of fluid resting upon a vibrating support, Philosophical Magazine 15: 229-235

Rayleigh, J. W. S. (1887), On the maintenance of vibration by forces of double frequency and on the propagation of waves through a medium endowed with a periodic structure, Philosophical Magazine 23: 145-159

Rayleigh, J. W. S. (1945). The theory of sound, vols. 1 and 2.

Tipton, C. (2003). Interfacial Faraday Waves in a Small Cylindrical Cell. Ph.D. thesis, University of Manchester.

Tipton, C. R., & Mullin, T. (2004). An experimental study of Faraday waves formed on the interface between two immiscible liquids. Phys. Fluids, 16, 2336–2341.

Wagner, C., Muller, H.-W., & Knorr, K. (2003). Pattern formation at the bicritical point of the Faraday instability. Phys. Rev. E, 68, 066204.

Wernet A., Wagner C., Papathanassiou D., Muller H., and K. Knorr, (2001), ‘‘Amplitude measurements of Faraday waves,’’ Phys. Rev. E 63, 036305.

Weber, Ernst H. and Wilhelm Weber. (1825). Wellenlehre auf Experimente gegründer. Leipzig: Gerhard Fleischer.

Wheatstone, Charles. (1823). “New Experiments on Sound.” Annals of Philosophy, N.S.6: 81–90.

Zoueshtiagh, F., Amiroudine, S., & Narayanan, R. (2009). Experimental and numerical study of miscible Faraday instability. J. Fluid Mech., 628, 43–55.

Appendix A: Detailed Experimental setup

A transparent *experimental cell* containing the test fluids was mounted on an oscillating platform. The temperature of the fluids inside the cell was controlled by a coolant medium (water) flowing over the cell which was circulated using a small pump. The actual control of the temperature of water entering the cell enclosure was carried out by a PID (proportional integral derivative) controlled immersion heater. The controller received temperature feedback from a probe suitably located in the circuit (Check data circuit A.6). Besides this heating, the water in the circuit was also cooled at the liquid-to-air heat exchanger run by a Peltier element.

A.1 Experimental Cell

Current cell used a rectangular design having internal dimensions 35mm in length, 29.3mm in height and 5 mm depth and had been chosen carefully to get discrete system (see section 2.2.4) with low frequency. The outer dimensions of the cell were 55 mm in length, 55 mm in height and 7 mm in depth. The cell consisted of a polycarbonate frame which was packed in the middle of two 55mm x 55mm x 1mm sapphire glasses at the front and the back enabling faster transfer of heat between the circulating fluid and the fluids inside the cell.

The cell was pre-sealed before experiment using a threaded screw wrapped with Poly tetra fluoroethylene (PTFE). The cell also included a special provision chamber made out of sealed hollow copper rectangular capsule for volume compensation which might be required to accommodate the thermal expansion of the liquids (See Figure A.1). Owing to the boiling point of FC-72 being 56 ^{o}C, the maximum temperature that was aimed to be realized for the fluids was fixed at 50 ^{o}C. The cell was enclosed in a small chamber where coolant water was circulated to maintain the desired temperature in the liquids. During the parabolic flight this whole assembly was in-turn placed inside a secondary confinement. This acted as a safety reservoir for the liquids in case of any leakage. In order to adjust with the scenario of Cabin de-pressurization during parabolic flight experiments, a protective vents screw was installed on the outer containment to compensate for the pressure change.

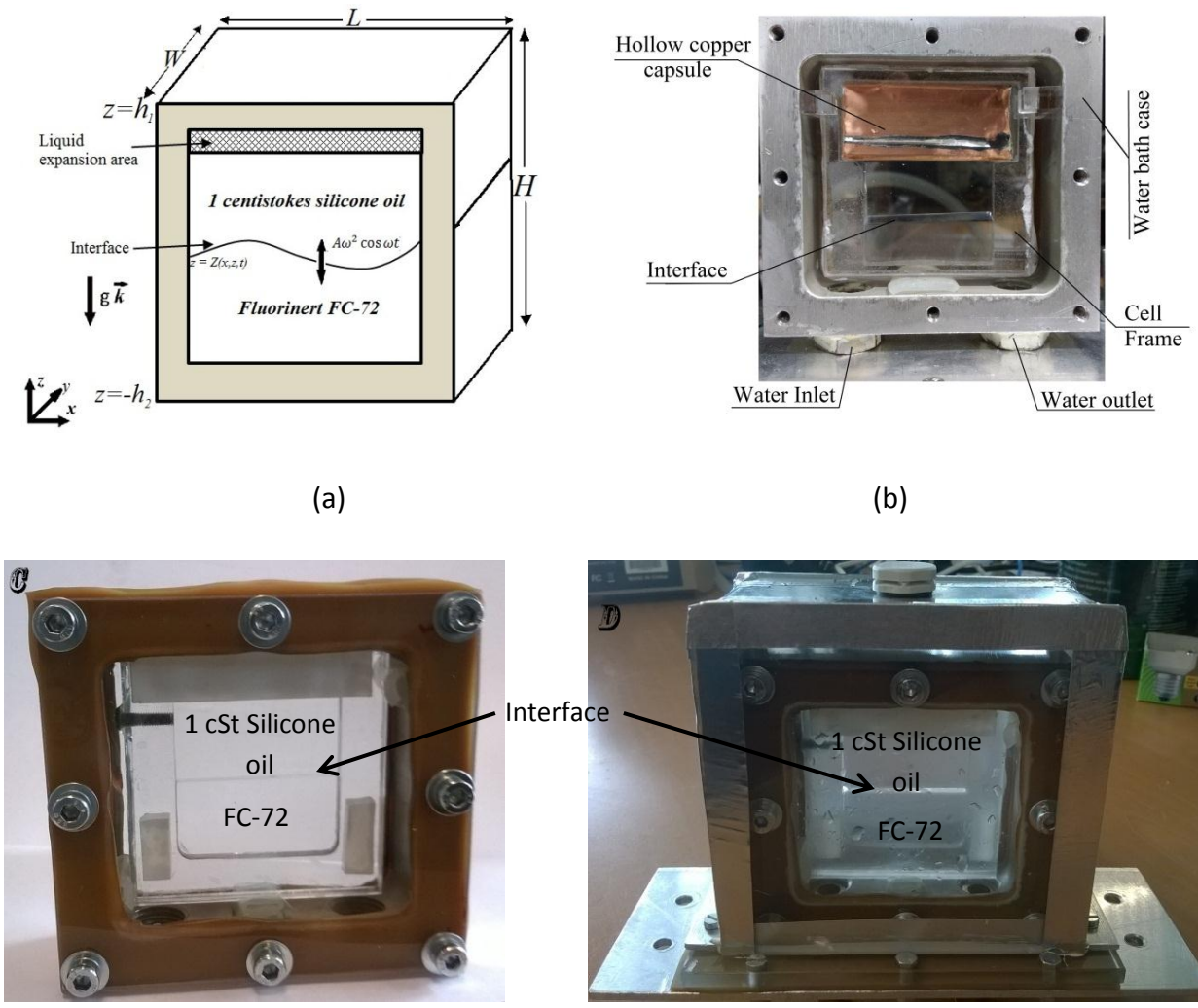

Figure A.1: Experimental Cell (a) Schematic diagram (b) Test cell with liquids (c) Inside confinement for flow of coolant water (d) Double confinement for parabolic flight

A.2 Electromechanical shaker

The cell along with its coolant enclosure was mounted on a vertically oscillating platform which was actuated by a linear drive with servo control of speed (Yaskawa SGMPH Sigma II 04AAA41D). The shaker was vertically mounted with eight fastening points to the experimental frame. The motion of the drive was computer controlled and allowed a maximum acceleration

of 3g with frequencies up to 15 Hz. The amplitudes and frequencies were observed to be within 1% and 0.1% of their respective set values. The oscillating platform was actuated by a linear drive with servo control of speed. The linear drive unit also included a complementary platform which helped in balancing the dynamic load on the rack. The oscillating platform was aided by a position switch which helped in fixing the base point of oscillations. Also to safe guard against the position overshoot/undershoot, two limits switches were provided next to the linear drive.

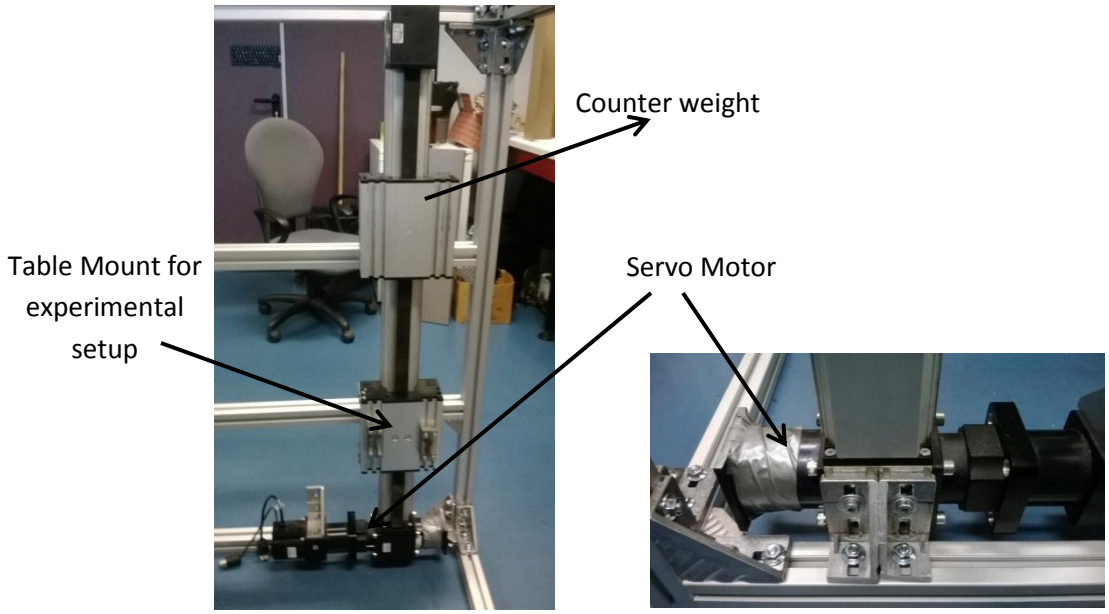

Figure A.2: (a) Pictures of shaker configuration and its fixation in the rack. (b) Servo motor

A.3 Water Bath circuit

The circulating water was actuated by a micro pump with maximum flow rate of 2800ml/min with a high circulation in order to provide real time temperature change in the cell. The desired temperature in the circuit (with a stability of ± 0.01 ^{0}C) was achieved using a PID controlled immersion heater. The heater controller received temperature feedback from a Pt-100 probe suitably located in the circuit (see data circuit A.6). Besides heating, the water circuit was also equipped with a feedback controlled Peltier element for cooling the liquids when required. The

role of the Peltier element was to provide necessary cooling of water in the circuit. The thermoelectric module (TEM) had a maximum power rating of 153W (V_{max} = *29.8 V;* I_{max} = *8.5 A*). The temperature of the water flowing out of the water-block was measured using a NTC (negative temperature coefficient) Thermistor. The temperature feedback thus obtained from the Thermistor was utilized to control the voltage applied to the TEM by a PR-59 (Proportional Controllers-59) controller.

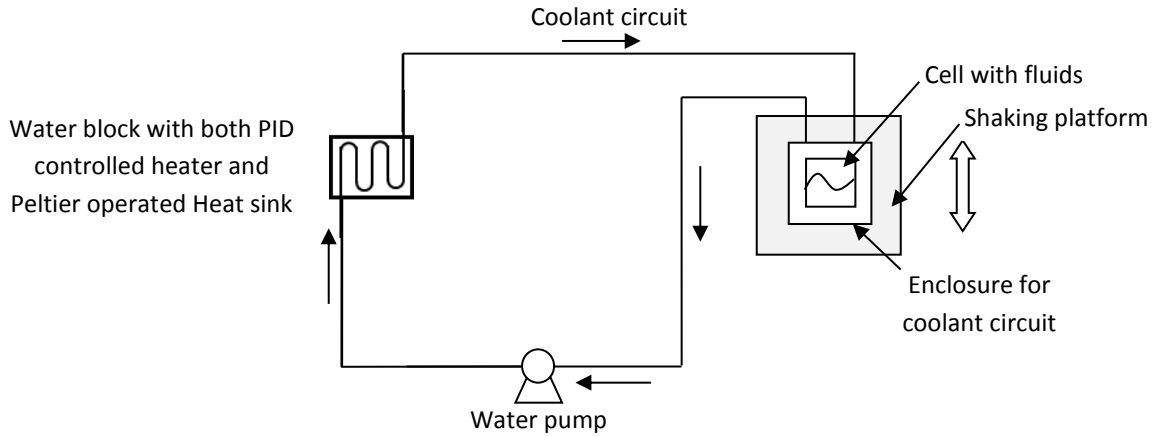

Figure A.3: Schematic diagram of water bath circuit

The PR-59 controller was linked to the computer using a RS-232 (standard for serial communication transmission of data) interface for remote control of the temperature. Along with the control of current to the Peltier module, the PR-59 also controlled the speed of the fan utilized for cooling the heat sink. The power to the controller was provided by a switching power supply of 156 W (24 VDC and maximum current 6.5 A). In addition to the control provided by PR-59, the setup also involved three other mechanisms to safeguard against any overheating. The first one involved the NC thermal switch which was placed on the side of the water block, so that the current to the TEM module would be cut-off if the local temperature on the block surface goes beyond 50 ^{o}C. Secondly, a thermocouple (J type) was placed on the heat sink to additionally measure its temperature. Using the temperature measured from this probe, the current to Peltier module was either switched ON or OFF by a secondary digital temperature controller. Thirdly, a current fuse (8A maximum) was utilized to limit the current to the TEM. In principle, the above cooling circuit was provided as an auxiliary mechanism to

compensate for the extra heat that might have been gained by the flowing water from lighting systems etc.

The actual control of the circulating liquid's temperature was achieved through a small immersion heater (diameter 6.5 mm, length 40 mm, Voltage 230 V and power 50 W) that was inserted inside the water-block. The water from the exit of this block was directly fed into the cell chamber where the desired temperature of the liquid had to be maintained. The temperatures at the inlet and the exit of the cell chamber were measured using PT-100 (Platinum Resistance) resistance thermometers. Using the measured outlet temperature of the water-block, the current supplied to the heater was controlled by an i-Series 1/16 DIN PID temperature controller.

The DC pulse feedback generated by the controller (based on the water temperature) was utilized to actuate a Solid State Relay (SSR) which regulates power to the heater. As a safety precaution, the current to the heater was routed via a fast fuse of rating 1 Amps. In addition to the safety provided by the temperature controller for over-heating, two reversible thermal switches placed on the top and the sides of the water-block were utilized to restrict its surface temperature below 50 ^{o}C.

In order to understand the thermal transience of the liquids enclosed within the cell, the outlet temperature at the chamber exit was also measured by another i-Series 1/16 DIN PID temperature monitor. The temperature values measured by both the controller and the monitor were logged on to a computer via RS-232 link for both storage and remote control purposes. It may be noted that the overall coolant circuit was realized using double silicone flexible tubes. The maximum volume of water that was used in the circuit was 200 ml and the maximum temperature that was attained by the water was less than 50 ^{o}C.

In order to safeguard from overheating, two thermal switches with a cut-off temperature of 50 ^{o}C were positioned on the water block surface close to the heater. The protection for the Peltier assembly was derived from the thermal switch positioned on the side of the water block. In addition, a J-type thermocouple was positioned on the heat sink which controlled the current to the Peltier element through an ON-OFF controller.

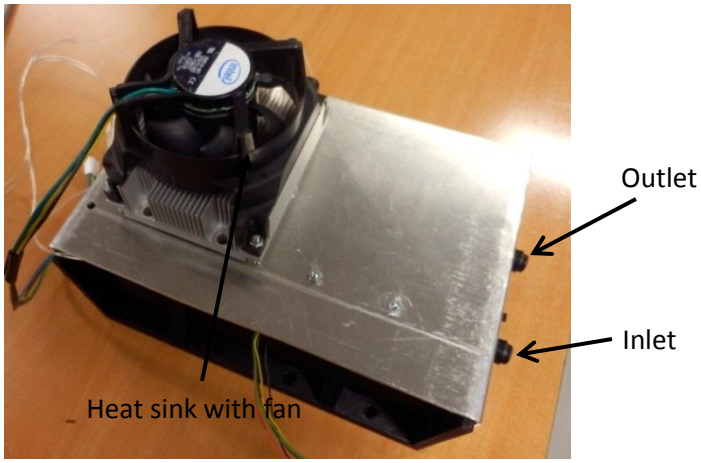

(a)

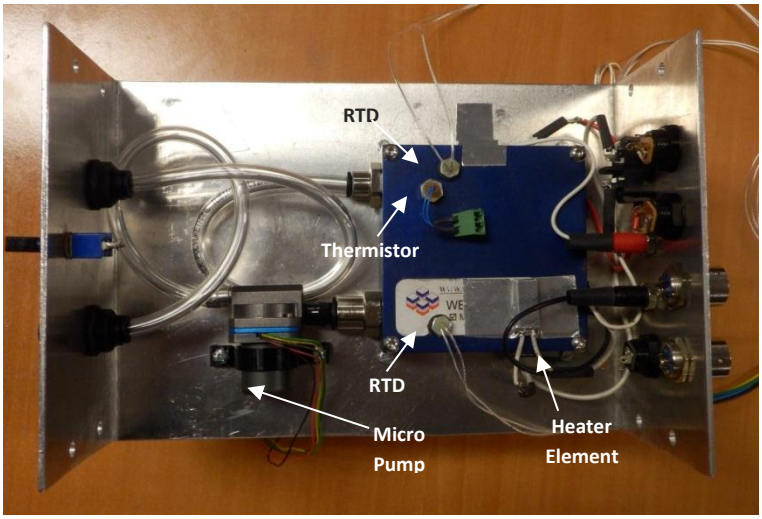

(b)

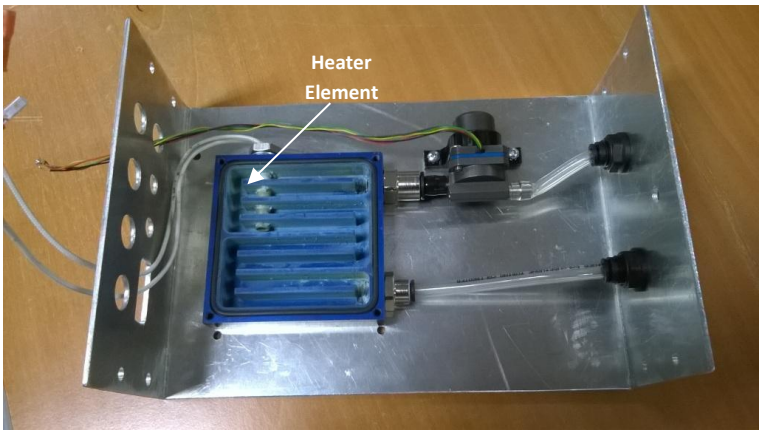

(c)

Figure A.3: Assembly for the control of circulating water temperature (a) Heat sink assembly (b) Inside view water temperature controller (c) Heating element

A membrane-based degasify system was utilized on a by-pass loop for the initial degassing of the water so that the instability phenomenon inside the cell was not shrouded by the bubbles formed out of dissolved gases. Using the above mechanisms, the temperature of the fluids inside the cell was accurately modified above and below the consolute temperature. Before each miscible oscillatory experiment, the fluid temperature was set below the consolute temperature to obtain a perfect separation of phases between the fluids. Once perfectly separated, the temperature was once again increased to lead the fluids into the miscible state.

A.4 Data recording Equipment

The phenomenon was recorded by a high speed camera (Photron SA3 60K M2) which was connected to a computer with a Gigabit Ethernet port (see section A.6). All motion of cell and interface phenomenon were examined using time-space data of the images, obtained from high speed digital imaging with frame rates of up to 2000 fps. The illuminations for the imaging process were obtained through a 30 W LED light placed behind the cell, on the moving platform. The power for this LED was supplied by a LED driver of capacity 50 W. In order to prevent over-heating of the LED lights, they were mounted on two cooling aggregates which were ventilated by small 12V DC fans. The motion of interface in the following presented data was captured at 500 images per second with an exposure time of 5µs. The recorded images were digitized and calibrated into length scales from which the size of the instability (wavelengths) has been measured.

A.5 Electrical circuit

A schematic of electrical circuit of the experimental setup has been shown in figure below. The yellow line in the circuit shows power connection and green light shows data connection between components.

Servo motor which takes maximum current of 2.6 ampere was connected by a single wire with 3G1.5mm^2 (15 amp capacity) wire. Another connection went for temperature control unit

explained above. A connection is for LED lights were located behind the experimental set-up to illuminate the cell. This cell motion and wave motion was captured by a high speed camera connected with system. An extra heater with TEM controller was also present in the system (explained in section A.3) for fast heating of experimental fluids.

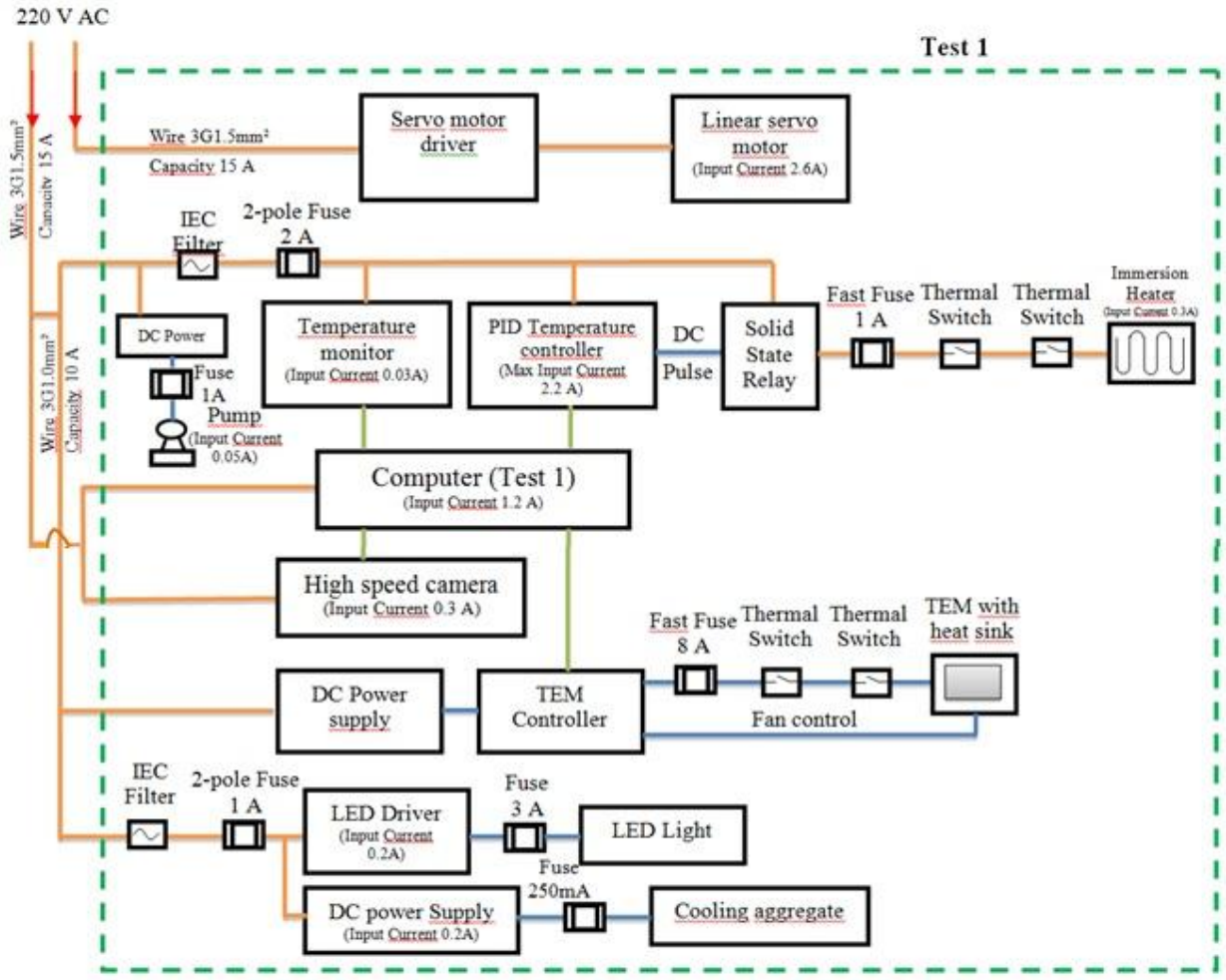

A.6 Data circuit

A schematic of data circuit of the experimental setup is shown in the figure below. Data links in the experiment were present to communicate the information to motor unit, temperature control and data recording equipment. Applied amplitude and frequency were communicated to linear drive unit with the help of a computer while monitoring the fluid temperature. The wave patterns were recorded by a high speed camera.

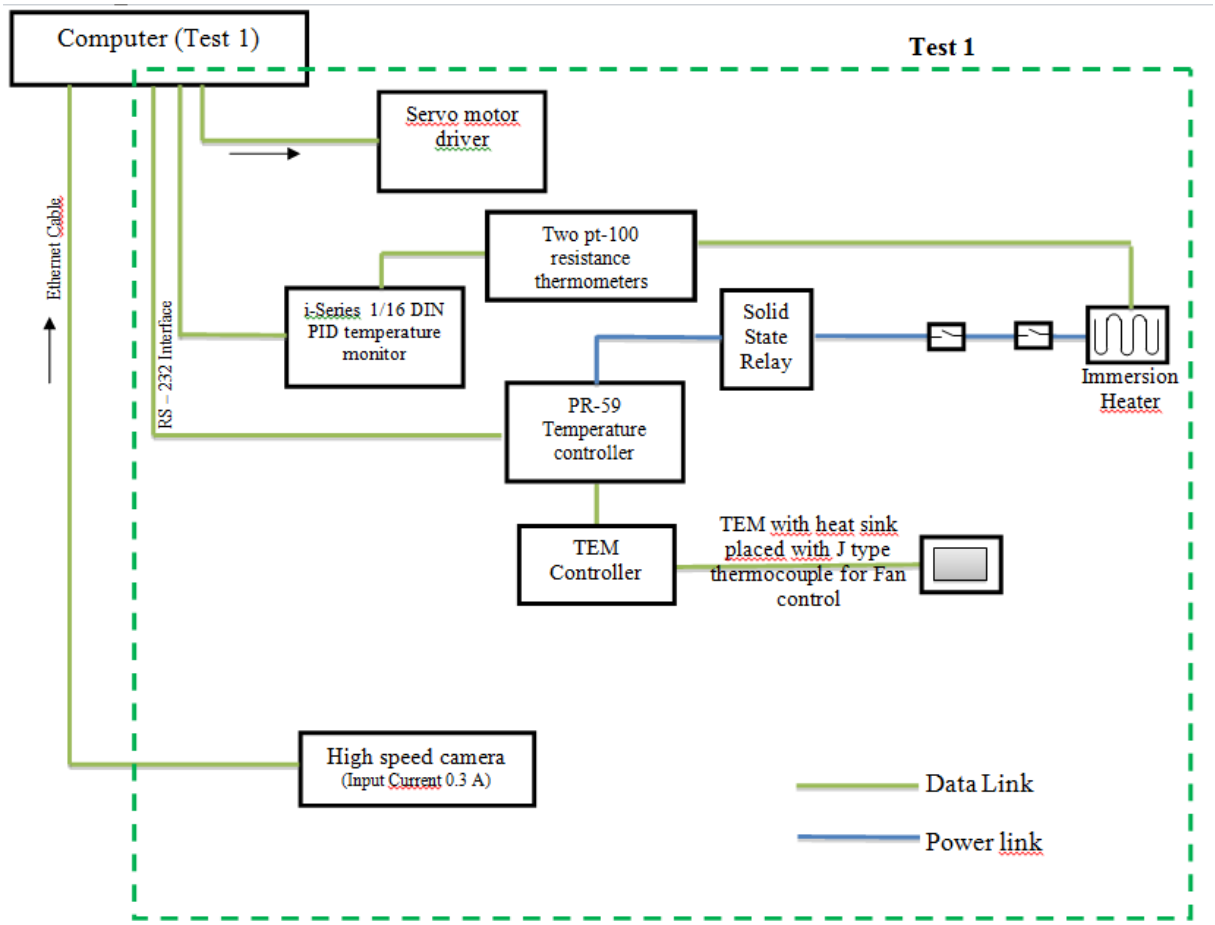
Computer (Test 1)
Test 1
Servo motor driver
Ethernet Cable
RS – 232 Interface
Two pt-100 resistance thermometers
i-Series 1/16 DIN PID temperature monitor
Solid State Relay
Immersion Heater
PR-59 Temperature controller
TEM Controller
TEM with heat sink placed with J type thermocouple for Fan control
High speed camera
(Input Current 0.3 A)
Data Link
Power link

Appendix B: MATLAB Code for inviscid fluids

```
% To plot the Response and Phase plane for the Mathieu's Equation
%~~~~~~~~~~~~~~~~~~~~~~~~~~~~~~~~~~~~~~~~~~~~~~~~~~~~~~~~~~~~~~~~~~~~~~~~~~~~
%|||||||||||||||||||||||||||||||||||||||||||||||||||||||||||||||||||||||||||||
%-------------------------------------------------------------------------
% Mathieu Equation is z''(t)+eta.z'(t)+(a-qsin(omega*t))*(z) = 0
clc ; clear all ; close all;
% Characteristic Exponents of the Mathieu Equation
result(1:10) = 0;
for gg = 1:1:10;
omega = 2*pi*1;
rowp1 = 999.97;
rowp2 = 956.10;
h1    = 0.02;
h2    = 0.02;
k     = 8;
EARTH_GRAVITY = 9.8;
gravity = gg/10*EARTH_GRAVITY;
gamma = 1;
amplitude = 8;
% q = ((rowp1 - rowp2)*omega*omega*amplitude)/(rowp1*coth(k*h1)+
rowp2*coth(k*h2));
% a = ((rowp1 - rowp2)*gravity*k - gamma*k*k*k)/((rowp1*coth(k*h1)+
rowp2*coth(k*h2)));
q = 2;
a = gg;
fprintf('     g = %d   q = %d    a = %d \n',gravity,q,a)
eta = 0.00 ;                  % Damping in the system
time = 0:0.01:80;           % Time span
theta0 = [0 0.25] ;          % Initial values
ivp = [theta0 q a eta omega] ;
% Time History Analysis using ODE45
sol = ode45(@MathieuEquation,time,ivp);
y = deval(sol,time);
theta = y(1,:)' ;
Dtheta = y(2,:)' ;
% Time History plot
figure ;
plot(time,theta) ;
xlabel('time','FontSize', 26) ;
ylabel('Amplitude','FontSize', 26);
set(gca,'linewidth',3)
set(gca,'fontsize',22)
set(gca, 'Ticklength', [0.01 0.01])
grid off
 % Phase plane plot
% figure ;
% plot(theta,Dtheta,'b') ;
% hold on ;
% plot(theta0(1),theta0(2),'or') ;
% xlabel('Z') ;
% ylabel('SECOND SOLUTION') ;
% axis equal ;
% hold off ;
[pks,locs] = findpeaks(theta);
```

```
frequency = diff(locs);
modifiedfrequency = frequency(find(frequency < 100));
modifiedfrequency = mean(modifiedfrequency);
result(round(gg)) = 100/modifiedfrequency;
filename = sprintf('range8%d',gg*10);
print(filename,'-djpeg','-r500')
end


function xdot = MathieuEquation(t,x)
% Mathieu Equation is y''(z)+eta.y'(z)+(a-qsin(omega*t))(y) = 0
% Written into two first order differential equations
% y'(z) = x
% x'(z) = -eta.y'(z)-(a-qsin(2z))(y)
%
n = length(x) ;
xdot=zeros(n,1);
theta = x(1) ;
Dtheta = x(2) ;
q = x(3) ;
a = x(4) ;
eta = x(5) ;
omega = x(6);
xdot(1) = Dtheta;
xdot(2) = -eta*Dtheta-(a-q*sin(omega*t))*theta;
```

Appendix C: MATLAB Code for viscous fluids

```
% To plot the threshold vibrational amplitude with frequency
%~~~~~~~~~~~~~~~~~~~~~~~~~~~~~~~~~~~~~~~~~~~~~~~~~~~~~~~~~~~~~~~~~~~~~~~~~~~~~~~
%|||||||||||||||||||||||||||||||||||||||||||||||||||||||||||||||||||||||||||||||
%-------------------------------------------------------------------------------
clear all
clc
format long

%%%%%%%%%%%% Required Parameter INPUT %%%%%%%%%%
rhoset=[1622,885              %1
1609.564815,890.9178378       %2
1597.648148,895.4912432       %3
1593.166667,910.1007135       %4
1492.12963,930.0972973        %5
1472.8,978.5                  %6
1325.0544,975                 %7
1280.7024,985                 %8
1228.7024,997                 %9
1393,1055];                   %10 %densities 1 (bottom) and 2 (top), kg/(m^3)
nu1set=[0.42,0.95             %1
18.993,22.587                 %2
17.118,20.462                 %3
15.243,18.337                 %4
13.368,16.212                 %5
18.493,19.087                 %6
10.618,11.962                 %7
8.6805,10.8995                %8
7.8,9.8                       %9
5.7,7.8];                     %10 %kinematic viscosities 1 and 2, centistokes
gammaset=[2.133 1.5375  1.2993  1.0611  0.8229  0.5847  0.3117  0.2276
0.1856  0.1083]/1000;%interfacial tension , kg /(s^2)
Temperatureset = [25,30,32,34,36,38,40,41,41.5,42];
hset = [0.01281,0.01719
0.01304,0.01696
0.01308,0.01692
0.01301,0.01699
0.01284,0.01716
0.01251,0.01749
0.01182,0.01818
0.01129,0.01871
0.01099,0.01901
0.01067,0.01933]; %layer heights 1 and 2, meters
g_set = [9.81 0.00001];
wavenumber_set = [87.18 87 87 87 87 87 87 86.43 86 86];
gi = 0;
range = 1;
for range = 1; %gravitational acceleration , m/(s^2)
g = g_set(1);
frange = [];
gi = gi+1;
rho = rhoset(range,:);
gamma = gammaset(range);
nu1 = nu1set(range,:);
```

```
h = hset(range,:);
wavenumber = wavenumber_set(range)/1;
fi=0;
theoriticalwork (1:20) = 0;
theoriticalwork1 (1:20) = 0;
f = 3.00;
fstep = 0.01;
while f<=3.6
fstep = fstep + 0.01;
if fstep >= 0.025
fstep = 0.025;
end
f = f+fstep; %imposed frequency , Hz
fi=fi+1;
%k=800; %wavenumber , m^-1
sigma=0; %mode growth rate , s^-1, zero for neutral stability
N=12; %Fourier series cutoff

%%%%%%%% Calculation proceeds from HERE %%%%%%%%%
    thresholds=zeros(46,2) ; %calculation output variable, and contains the
harmonic and subharmonic neutral stability amplitudes
    thresholds2=zeros(46,2);
    thresholds3=zeros(46,2);
    thresholds4=zeros(46,2);
    nu=nu1/1e6 ; %kinemat viscosity conversion , cSt to m^ 2 / s
    mu=rho.*nu; %dynamic viscosity calculation, kg/m*s
    omega=2*pi*f ; %frequency conversion , Hz to radians/s
    Index=0;
for alpha=[0, 1/2*omega]
    count=1;
    Index=Index+1;
    numodenu = 0;
    for k = wavenumber:wavenumber:wavenumber*12;
        numodenu = numodenu+1;
        if numodenu == 1
            nu = [0.64 1]*51.32/(1e6);
        elseif numodenu == 2
            nu = [0.64 1]*16.24/(1e6);
        elseif numodenu == 3
            nu = [0.64 1]*9.06/(1e6);
        elseif numodenu == 4
            nu = [0.64 1]*6.90/(1e6);
        elseif numodenu == 5.51 && alpha ~= 0
            nu = [0.64 1]*2.79/(1e6);
        elseif numodenu == 12.58 && alpha == 0
            nu = [0.64 1]*2.79/(1e6);
        elseif numodenu == 6
            nu = [0.64 1]*5.51/(1e6);
        elseif numodenu > 6
            nu = [0.64 1]*5.51/(1e6);
        end
        mu=rho.*nu;
           INDEX1=0;
            INDEX1=INDEX1+1;
                D=zeros(2*(N+1)) ; %eigenvalue problem D?matrix initialize
                for n=0:N; %loop to calculate the D-matrix coefficients for
each Forier mode n
```

```
                    fexp =(sigma+1i*(alpha+n*omega)) ; %Fourier Floquet
exponent
                    q1=sqrt(k^2+1/nu(1)*fexp) ; %characteristic solution
exponent1
                    q2=sqrt(k^2+1/nu(2)*fexp) ; %characteristic solution
exponent2
                    b=zeros(8,1); %initialization of inhomogeneity in
boundary condition system of equations
                    b(8)=fexp; %insertion of Floquet exponent arising from
kinematic condition
        %Here the matrix defined by the system of equations arising from the
boundary conditions  is constructed . The characteristic velocity solutions
include z?exp(k?z) and z?exp(?kz)instead of exp(q1?z) and exp(q2?z) when
q1=q2=0 and the coefficients for these solutions are calculated first.
                    if fexp==0
                        fhs =[exp(-k*h(1)), exp(k*h(1)), h(1)*exp(-k*h(1)),
h(1)*exp(k*h(1)) , 0, 0, 0, 0; %no flow condition , bottom sur face
                              0, 0, 0, 0, exp(k*h(2)), exp(-k*h(2)),
h(2)*exp(k*h(2)),h(2)*exp(-k*h(2)) ; %no flow ,top surface
                              k*exp(-k*h(1)), -k*exp(k*h(1)), h(1)*k*exp(-
k*h(1))+exp(-k*h(1)),-h(1)*k*exp(k*h(1))+exp(k*h(1)), 0, 0, 0, 0; %no slip
condition , bottom surface
                              0, 0, 0, 0, k*exp(k*h(2)), -k*exp(-k*h(2)),
h(2)*k*exp(k*h(2))+exp(k*h(2)), -h(2)*k*exp(-k*h(2))+exp(-k*h(2)) ; %no slip,
top surface
                              -1, -1, -1, -1, 1, 1, 1, 1,; %continuity of
velocity at the interface
                              -k, k, -1, -1, k, -k, 1, 1; %continuity of
velocity zderivative at the interface
                              -mu(1)*2*k^2 ,-mu(1)*2*k^2, -mu(1)*(k^2+2*k), -
mu(1)*(k^2-2*k), mu(2)*2*k^2, mu(2)*2*k^2, mu(2)*(k^2+2*k), mu(2)*(k^2-2*k) ;
% continuity of tangential stresses at the interface
                              1, 1, 1, 1, 0, 0, 0, 0] ; %kinematic condition.
equally can be written as 0 , 0 , 0 , 0 ,1 , 1 , 1 ,1]
                        coeff=fhs\b ; %calculation of the velocity profile
coefficients
                        dz1=coeff(1)*k-coeff(2)*k+coeff(3)-coeff(4);
%evaluation of first z?derivative of the lower layer velocity profile at z=0
                        dzzz1=coeff(1)*k^3-
coeff(2)*k^3+coeff(3)*3*k^2+coeff(4)*3*k^2; %third z?derivative of the lower
layer
                        dz2=coeff(5)*k-coeff(6)*k+coeff(7)-coeff(8); %first
z?derivative of the upper layer
                        dzzz2=coeff(5)*k^3-
coeff(6)*k^3+coeff(7)*3*k^2+coeff(8)*3*k^2; %third z?derivative of the upper
layer
                        Dn=(rho(2)*fexp+3*mu(2)*k^2)*dz2-mu(2)*dzzz2-
((rho(1)*fexp+3*mu(1)*k^2)*dz1-mu(1)*dzzz1)+((rho(2)-rho(1))*g-
gamma*k^2)*k^2; %evaluation of the D?matrix coefficients for each Fourier
mode n
                    else %calculation for when q1=q2 are not zero . Same
format as above .
                        fhs=[exp(-k*h(1)), exp(k*h(1)), exp(-q1*h(1)),
exp(q1*h(1)), 0, 0, 0, 0;
                              0, 0, 0, 0, exp(k*h(2)), exp(-k*h(2)),
exp(q2*h(2)), exp(-q2*h(2));
```

```
                            k*exp(-k*h(1)), -k*exp(k*h(1)), q1*exp(-q1*h(1)),
-q1*exp(q1*h(1)), 0, 0, 0, 0;
                            0, 0, 0, 0, k*exp(k*h(2)), -k*exp(-k*h(2)),
q2*exp(q2*h(2)), -q2*exp(-q2*h(2));
                            -1, -1, -1, -1, 1, 1, 1, 1,;
                            k, -k, q1, -q1, -k, k, -q2, q2;
                            mu(1)*2*k^2, mu(1)*2*k^2, mu(1)*(k^2+q1^2),
mu(1)*(k^2+q1^2), -mu(2)*2*k^2, -mu(2)*2*k^2, -mu(2)*(k^2+q2^2), -
mu(2)*(k^2+q2^2);
                            1, 1, 1, 1, 0, 0, 0, 0];
                        coeff=fhs\b;
                        dz1=coeff(1)*k-coeff(2)*k+coeff(3)*q1-coeff(4)*q1;
                        dzzz1=coeff(1)*k^3-coeff(2)*k^3+coeff(3)*q1^3-
coeff(4)*q1^3 ;
                        dz2=coeff(5)*k-coeff(6)*k+coeff(7)*q2-coeff(8)*q2;
                        dzzz2=coeff(5)*k^3-coeff(6)*k^3+coeff(7)*q2^3-
coeff(8)*q2^3 ;
                        Dn=(rho(2)*fexp+3*mu(2)*k^2)*dz2-mu(2)*dzzz2-
((rho(1)*fexp+3*mu(1)*k^2)*dz1-mu(1)*dzzz1)+((rho(2)-rho(1))*g-
gamma*k^2)*k^2;
                    end
                    D(2*n+1, 2*n+1)=real(Dn); %placement of the real and
imaginary components Dn in the Dmatrix
                    D(2*n+1, 2*n+2)=-imag(Dn);
                    D(2*n+2, 2*n+1)=imag(Dn);
                    D(2*n+2, 2*n+2)=real(Dn);
                end
                B=zeros(2*(N+1)) ; %construction of the B matrix
                if alpha==0; %harmonic
                    B(1,3)=2;
                    B(3:2*(N+1) ,1:2*N)=eye(2*N);
                    for i =1:2*(N-1)
                        B(2+i,4+i)=1;
                    end
                else %subharmonic
                    B(1,1) =1;
                    B(2,2) =-1;
                    B(3:2*(N+1),1:2*N)=eye(2*N);
                    for i =1:2*N
                        B(i,2+i)=1;
                    end
                end

                [eigenvecs,eigenvals]=eig(D,1/2*(rho(2)-rho(1))*k^2*B);
%solution of the eigenvalue problem
                eigenvals=diag(eigenvals);
                %stop
                index1=0; %routine used to sort through the obtained
eigenvalues
                for index2=1:length(eigenvals) %
                    if isnan (eigenvals(index2)) %NaN eigenvalues ignored
                    elseif isinf(eigenvals(index2)) %infinite eigenvalues
ignored
                    elseif abs(imag(eigenvals(index2)))>1e-6 %super tiny
eigenvalues ignored
                    elseif eigenvals(index2)<0 %negative eigenvalues ignored
                    else
```

```
                        index1=index1+1; %index set for positive eigenvalues
                        evals(index1)=eigenvals(index2); %eigenvalue stored
in evals vector
                        if abs(imag(evals(index1)))<1e-6 %disposal of super
tiny complex parts
                            evals(index1)=real(evals(index1));
                        end
                    end
                end
                evals=sort(evals); %sorting of the obtained eigenvalues
                evals2=100/omega^2*evals; %conversion from acceleration
Aomega^2 to amplitude A, centimeters
                thresholds(count,Index)=evals2(1,1); %output variable
                sizeevl = size(evals2);
                if sizeevl>1
                thresholds2(count,Index)=evals2(1,2);
                else
                thresholds2(count,Index) = 99999999;
                end
                if sizeevl>2
                thresholds3(count,Index)=evals2(1,3);
                else
                thresholds3(count,Index) = 99999999;
                end
                if sizeevl>3
                thresholds4(count,Index)=evals2(1,4);
                else
                thresholds4(count,Index) = 99999999;
                end
                wavelengths(count,Index)=k;
                count=count+1;
    end
    nu = [0.64 1]/1e6;
    mu = rho.*nu;
end
% % %
plot(wavelengths(:,1),thresholds(:,1),'r*',wavelengths(:,1),thresholds2(:,1),
'r*',wavelengths(:,1),thresholds3(:,1),'r*',wavelengths(:,1),thresholds4(:,1)
,'r*',
wavelengths(:,2),thresholds(:,2),'g*',wavelengths(:,2),thresholds2(:,2),'g*',
wavelengths(:,2),thresholds3(:,2),'g*',wavelengths(:,2),thresholds4(:,2),'g*'
)
%
plot(wavelengths(:,1),thresholds(:,1)*10,'b.',wavelengths(:,1),thresholds2(:,
1)*10,'b.',wavelengths(:,1),thresholds3(:,1)*10,'b.',wavelengths(:,1),thresho
lds4(:,1)*10,'b.',
wavelengths(:,2),thresholds(:,2)*10,'b.',wavelengths(:,2),thresholds2(:,2)*10
,'b.',wavelengths(:,2),thresholds3(:,2)*10,'b.',wavelengths(:,2),thresholds4(
:,2)*10,'b.');
% axis([0,550,0,50])
lim (1:12) = 0;
stepmatnumber = wavenumber/wavenumber;
for crit  = 1:12
matcrit = [thresholds(crit*stepmatnumber,1) thresholds2(crit*stepmatnumber,1)
thresholds3(crit*stepmatnumber,1) thresholds4(crit*stepmatnumber,1)
thresholds(crit*stepmatnumber,2) thresholds2(crit*stepmatnumber,2)
thresholds3(crit*stepmatnumber,2) thresholds4(crit*stepmatnumber,2)];
```

```
    lim(crit) = min(matcrit)*10;
end
% xlabel('wavenumber k (m^{-1})')
% ylabel('Vibrational Amplitude A (mm)')
% tiltlevary = sprintf('Faraday Instability Critical Amplitudes @ frequency =
%d', f);
% title(tiltlevary)
% hold on
stepmat = wavenumber/1;
% plot([100 100]*stepmat,[0 lim(1)],'r--',[200 200]*stepmat,[0 lim(2)],'r--
',[300 300]*stepmat,[0 lim(3)],'r--',[400 400]*stepmat,[0 lim(4)],'r--',[500
500]*stepmat,[0 lim(5)],'r--',[600 600]*stepmat,[0 lim(6)],'r--');
indexmin = find(lim == min(lim));
xmin = stepmat*indexmin*100;
ymin = lim(indexmin);
% strmin = ['Critical Threshold = ',num2str(ymin) 'mm' char(10) 'Critical
Mode = ' num2str(indexmin)];
% text(xmin,ymin,strmin,'HorizontalAlignment','left');
% filename = sprintf('frequency%d',(f*100 + 1));
% print(filename,'-djpeg')
% hold off
theoriticalwork(fi) = ymin(1);
theoriticalwork1(fi) = indexmin(1);
frange = [frange f];
end
% % ampg(gi) = ymin;
% % wavenug (gi) = indexmin;
% % f = 0.1:0.1:10;
markerlist='vop>*h<.xs^dvop>*h<.xs^dvop>*h<.xs^dvop>*h<.xs^dvop>*h<.xs^dvo';
colorlist='mcrgbkmcrgbwkmcrgbkmcrgbkmcrgbkmcrgbwkmcrgbkmcrgbwkmcrgbk';
experimental=[19    15.9    13.5    11.4    9.5 7.8 6.3 5.1 4.1 3.7 3.6 4
4.5 5.2 5.8 6.5 7.1 7.2 7.2 7   6.7 6.3 6   5.5 5   4   3.3 2.7 2.2 2   1.9 2
2.2 2.4 2.4 2.7 2.8 2.8 2.5 2.1 1.8 1.6 1.6 1.9 2   2   1.7 1.5 1.4];
experimentalred=[3.4    3.5 3.6 3.7 3.8 3.9 4   4.1 4.2 4.3 4.4 4.5 4.6 4.7
4.8 4.9 5   5.1 5.2 5.3 5.4 5.5 5.6 5.7 5.8 6   6.2 6.4 6.6 6.7 6.8 6.9 7
7.1 7.2 7.3 7.4 7.6 7.8 8   8.2 8.4 8.6 8.8 9   9.25    9.5 9.75    10];
experimentalmode = [1   1   1   1   1   1   1   1   1   1   1   1   1   1   1
1   1   5   5   5   5   5   2   2   2   2   2   2   2   2   2   2   2   2   2
2   2   3   3   3   3   3   3   3   3   4   4   4   4];
for ncolor1=1:max(experimentalmode)
p1 = plot(experimentalred(experimentalmode==ncolor1),
experimental(experimentalmode==ncolor1), markerlist(ncolor1),'MarkerSize',12,
'MarkerEdgeColor', 'k', 'MarkerFaceColor',colorlist(ncolor1));
hold on
end
% % if interfacialevelrange == 2.45
% % flevelrange = frange;
% % theoriticalwork1g = theoriticalwork1;
% % theoriticalworkg = theoriticalwork;
% % end
% % if interfacialevelrange ~= 2.45
% % thresholdplot = plot(flevelrange, theoriticalworkg,'b--
','MarkerSize',5);thresholdplot.Color(4)=0.3;
% % end
hold on
Linestyle = ['- '; '--'; ': '; '-.';'- '; '--'; ': '; '-.';'- '; '--'; ': ';
'-.';'- '; '--'; ': '; '-.'];
```

```
for ncolor=1:max(theoriticalwork1)
p2 = plot(frange(theoriticalwork1==ncolor),
theoriticalwork(theoriticalwork1==ncolor),Linestyle(ncolor,:),'LineWidth',nco
lor);
set(p2,'color',colorlist(ncolor))
set(gca,'linewidth',3)
set(gca,'fontsize',22)
set(gca, 'Ticklength', [0.01 0.01])
grid off
hold on
end
hold off
% graph=plot(f,theoriticalwork,'b.');
axis([3,10,0,23])
xlabel('Applied frequency (Hz)','FontSize', 26)
ylabel('Vibrational Amplitude A (mm)','FontSize', 28)
% title('Gravitational acceleration  =')
% set(get(gca,'title'),'Position',[4.3 18.6 1.00011],'FontSize', 28)
% strmin = sprintf('g = %1.2f m^2/s',g);
strmin = sprintf('1000mm, 35 mm, 30 mm (L*W*H)');
text(2,40,strmin,'HorizontalAlignment','left','VerticalAlignment','top','Font
Size', 16, 'Color','black');
tiltlevary = sprintf('Temperature = %1.1f (^0C)',Temperatureset(range));
title(tiltlevary)
% ['\Delta\rho ='], [sprintf('%1.0f kg/m^{3}'rho(1) - rho(2)])
hold on
% legend([p1,p2],'Experimental','Theoretical')
% pbaspect([2.8 1 1])
filename = sprintf('range%d',range);
print(filename,'-djpeg','-r500')
% plot(f,theoriticalwork1*4,'r-.');
hold off
close all
end
% g = 0.01:0.01:9.81;
% graph=plot(g,ampg,'b.');
% hold on
% % plot(f,theoriticalwork1*4,'r-.');
% hold off
```